Title
High-Throughput Plasmonic Nanolithography

Author
Pan, Liang

Publication Date
2010

Peer reviewed|Thesis/dissertation

High-Throughput Plasmonic Nanolithography

by

Liang Pan

A dissertation submitted in partial satisfaction of the

requirements for the degree of

Doctor of Philosophy

in

Engineering-Mechanical Engineering

in the

Graduate Division

of the

University of California, Berkeley

Committee in charge:

Professor David B. Bogy, Co-Chair

Professor Xiang Zhang, Co-Chair

Professor Roberto Horowitz

Professor Ming Wu

Fall 2010

High-Throughput Plasmonic Nanolithography

by

Liang Pan

Abstract

High-Throughput Plasmonic Nanolithography

by

Liang Pan

Doctor of Philosophy in Engineering-Mechanical Engineering

University of California, Berkeley

Professor David B. Bogy, Co-Chair

Professor Xiang Zhang, Co-Chair

The conventional projection-type photolithography approach to nanoscale manufacturing is facing possibly insurmountable challenges, especially to invent novel technical solutions that remain economical for the next generation of semi-conductor integrated circuits. Although extreme ultra violet (EUV) lithography with the next generation photo-masks and 193-nm immersion lithography with double patterning are expected to deliver 22 nm and smaller nodes, it still cannot effectively address the reliability and cost issues required for mass production. Maskless nanolithography is a potentially agile and cost effective approach, but most of the current solutions have throughputs that are too low for manufacturing purposes.

This dissertation reports a new low-cost high-throughput approach to maskless nanolithography that uses an array of plasmonic lenses (PL) that "fly" above the rotating surface to be patterned, concentrating short wavelength surface plasmons into sub-100 nm spots. However, these nanoscale spots are only formed in the near field (within a few nanometers of the surface), which makes it very difficult to scan the array above the surface at high speeds. To overcome this problem a self-spacing air-bearing surface was designed and fabricated that can fly the array just nanometers above a disk that is spinning at speeds on the order of 10 meter/second, and patterning with feature sizes far smaller than the far-field diffraction limit have been experimentally demonstrated . Using this plasmonic nanolithography (PNL) approach, a 22-nm half-pitch direct pattern writing was successfully demonstrated using ultra-fast laser assisted nanoscale heat management and advanced PL designs.

This nano-fabrication scheme has the potential of a few orders of magnitude higher throughput than current maskless techniques, and it opens the way for a new cost effective approach towards the next generation lithography for nano-manufacturing.

To My Family

Acknowledgement

I would like to express my deepest gratitude to my research advisors, Professor David B. Bogy and Professor Xiang Zhang, for their guidance and encouragements through my doctoral study. I would sincerely thank my former Xlab manager, Professor Cheng Sun (Northwestern University), who has been very important in shaping my research path and for helping me in the past five years.

I would also like to thank all my former and current teammates, Werayut Srituravanich, Yongshik (Peter) Park, Yi Xiong, Erick Ulin-Avila, Yuan Wang and Li (Leo) Zeng for all the valuable discussions, collaboration and helps. It has been my great pleasure to work together with them.

I want to extend my thanks to my former and current colleagues both in CML and Xlab, Du Chen, Nan Liu, Guy Bartal, Zhaowei Liu, Dongmin Wu, David Pile, Rupert Oulton, Jia-Yang Juang, Rohit Ambekar, Shuang Zhang, Xiaobo Yin, Nicholas (Xuanlai) Fang, Yongmin Liu, Sheng Wang, Ming Liu, Sean Moseley, Puneet Bhargava, Sujit Kirpekar, Sripathi Canchi, Ning Li, Thomas Zentgraf, Lee Fok, Hyeun-Seok Choi, Branden Cox, Christian Spencer, Jessica Little, Nga Thien Bui, and all the other colleagues for their advice, support, and friendship.

I also want to thank Professor C. Singh Bhatia (National University of Singapore), Professor Robert Hocken (UNC Charlotte), and Professor Tsu-Chin Tsao (UCLA) for all the valuable suggestions, collaboration and helps.

Finally, I am deeply indebted to my families for their love and support. Any of my successes is impossible without their great love and encouragement.

Contents

List of Figures

List of Tables

Chapter 1 Introduction

1.1 Introduction to Current Nanolithography

1.1.1 History and Status of Photolithography

Nanolithography is a process of patterning at the nanoscale, typically from 100 nm down to the molecular and atomic levels, and it has been used extensively during the past decade. There are many approaches to creating nanoscale patterns using either top-down or bottom-up schemes. Top-down schemes seek to create and assemble nanoscale patterns using larger devices, while bottom-up schemes seek to assemble smaller entities into larger and more complex ones. Currently, the top-down scheme is still dominant over the bottom-up scheme in both manufacturing and research, but there is a possibility that the bottom-up scheme may take over as the primary nanolithography approach because of the ever-increasing complexity and cost of the top-down scheme.

The semiconductor industry provides the primary demand for economical high-throughput nanolithography approaches and effectively drives the development of nanolithography to keep their trends of growth. As described by the famous Moore's law, the number of transistors that can be placed inexpensively on an integrated circuit doubles approximately every two years in a long-term development trend of computing hardware.

Figure 1.1 shows this trend taking CPU as an example.

Photolithography [1, 2] as an important branch of the nanolithography, is exclusively employed in current semiconductor manufacturing. In order to keep the aforementioned growth trends of Moore's law, photolithography needs to maintain a similar trend of feature size reduction at about 0.7X every two years. Current advanced photolithography tools use an optical system to project a pattern on a photosensitive resist. The smallest achievable feature is primarily determined by the resolution of the optical system as shown in following equation, where W_{min} is the minimum feature size or critical dimension (CD), λ is the wavelength and NA is the optical numerical aperture of the illumination and k_1 is a process-related coefficient (commonly called the k_1 factor) used in place of the constant 0.61 in the Rayleigh resolution formula.

Rayleigh resolution: $R = \frac{0.61\lambda}{NA}$ and photolithography resolution: $W_{\min} = k_1 \frac{\lambda}{NA}$

The photolithography industry has been very successful in improving pattern density in the past by continuously introducing shorter wavelength (from i-line 365 nm, to KrF 248 nm, and then ArF 193nm), with higher NA together with many other engineering improvements. A few years ago, there were much work on achieving 157 nm using an F_2 light source but it didn't succeed due

to complexity, high cost and lack of future potential. Current state-of-the-art photolithography tools use an ArF light source at 193 nm vacuum wavelength with water immersion in order to further reduce the effective wavelength. The NA of optics is reaching 0.93 and the k_1 factor is reaching 0.25 by using photoresist engineering, phase shift masks, off-axis illumination (OAI), optical proximity correction (OPC) and many other techniques to produce a minimum feature size of 32 nm in mass production. It is widely believed that 32 nm will be the smallest feature size the current photolithography approach alone can produce economically. For further improvements, some non-optical methods will be needed to get even finer patterns.

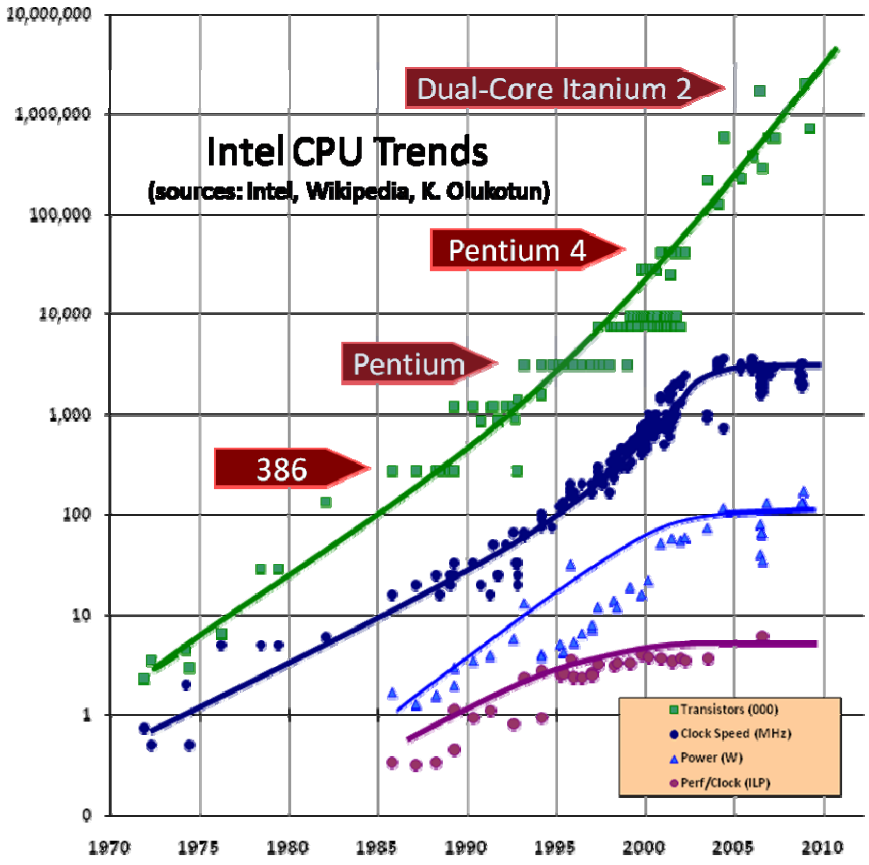

Figure 1.1: Growth trend of transistor counts in Intel CPU Introductions. The transistor count roughly doubled every two years in the past two decades. (Source: Intel)

According to the International Technology Roadmap for Semiconductors (ITRS) the lithography roadmap (shown in Figure 1.2), another technique called double patterning will likely be employed in a few years to further increase the pattern density. Although the double patterning approach as shown in Figure 1.3 can provide a short term extension of conventional photolithography, this ever-improving trend of photolithography will inevitably stop due to the

fundamental limit of far-field optical diffraction and the infamous problem of ultra-short wavelength light absorption. The issue that the current photolithography approach is facing is the increasing process complexity and its extremely high cost. For example, a state-of-the-art tool costs more than 65 million dollars each, and each set of photomasks also costs a few million dollars. Lithography cost has become the major cost for chip fabrication. Currently, there is an urgent call for an exotic technology to deliver an affordable patterning solution in the near future.

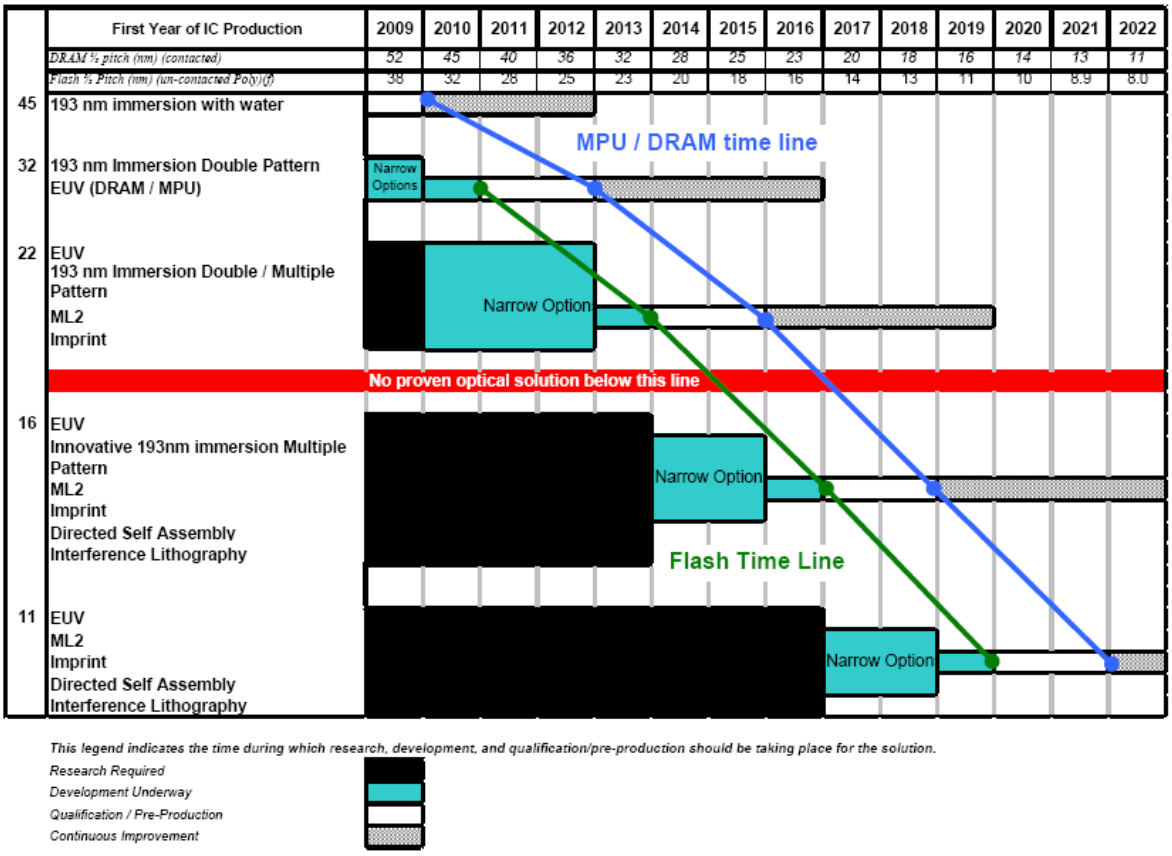

Figure 1.2: ITRS lithography roadmaps updated at year 2009.

1.1.2 Alternative Approaches

The semiconductor industry is looking for some alternative solutions for 22 nm half-pitch and below. Many approaches have been proposed and intensively studied for mass production purposes. And among them, EUV, nanoimprint and maskless from top-down schemes are identified as potential solutions. Although there are no fundamental limits that prevent these approaches reaching the desired resolution, whether any technology will eventually succeed is mainly determined by its economical feasibility. Even if one approach is currently identified as a

potential solution, it doesn't necessarily mean that it will indeed be capable of meeting the requirements for 16 nm half-pitch and below. At the current stage, some particular applications are focusing on bottom up approaches, such as copolymer self-assembly.

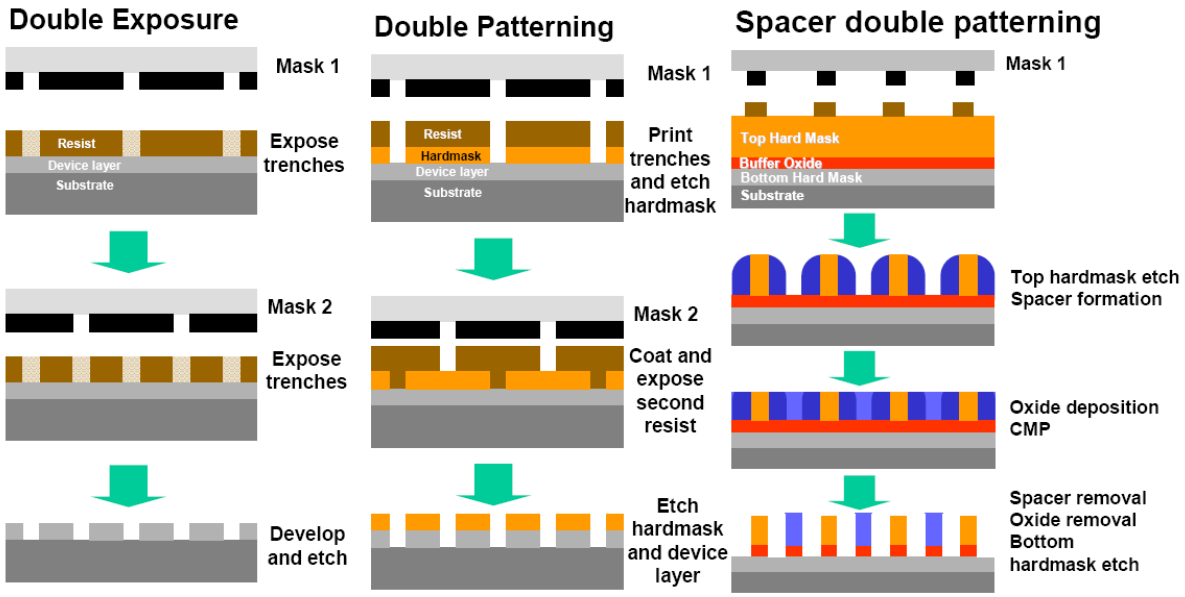

Figure 1.3: Process flows for pitch splitting and spacer patterning. (Source: 2009 ITRS lithography white papers)

1.1.2.1 Extreme Ultra-Violet lithography (EUVL)

Currently, EUVL [3-9] ranks as the most likely candidate for 22 nm and 16 nm half-pitch patterning in the ITRS lithography roadmap. It is preferred because of its similarity to photolithography and its noncontact feature. Many techniques that have been learned along the path of photolithography are applicable to EUVL as well, such as photoresist engineering, phase shift masks, off-axis illumination (OAI) and optical proximity correction (OPC). EUV represents the vacuum wavelength range of 10~120 nm. This wavelength range is distinguished from the others because of its infamous nature of suffering from absorption. Everything including air has strong absorption in this wavelength range. This leads to many issues and thus makes EUVL very expensive in practice [10, 11]. It requires all vacuum operations which will limit the overall throughput. And both the optics and masks need to be reflective rather than transmissive, which limits the feasible maximum NA (<0.5) of the EUVL system as shown in Figure 1.4.

Due to the lack of high NA EUV optics, a much shorter wavelength of 13.4 nm is required in practice to deliver the desired resolution. Although EUVL has been developed for years, many obstacles still exist including the availability of the EUV source, debris, blank and mask, resists, and more. More critically, current data on EUV mask development show positioning of about 25X to 100X off from the target and there is still no mask inspection tool available. Despite the fact that

current EUVL is expected to require extremely high tool and process cost, which makes it poor economically, it is still likely to be employed if it has enough throughput and reliability to manifest itself as profitable for the semiconductor industry. In fact, 193 nm wavelength projection photolithography, the only one yet available but very expensive, are actually working in high volume manufacturing.

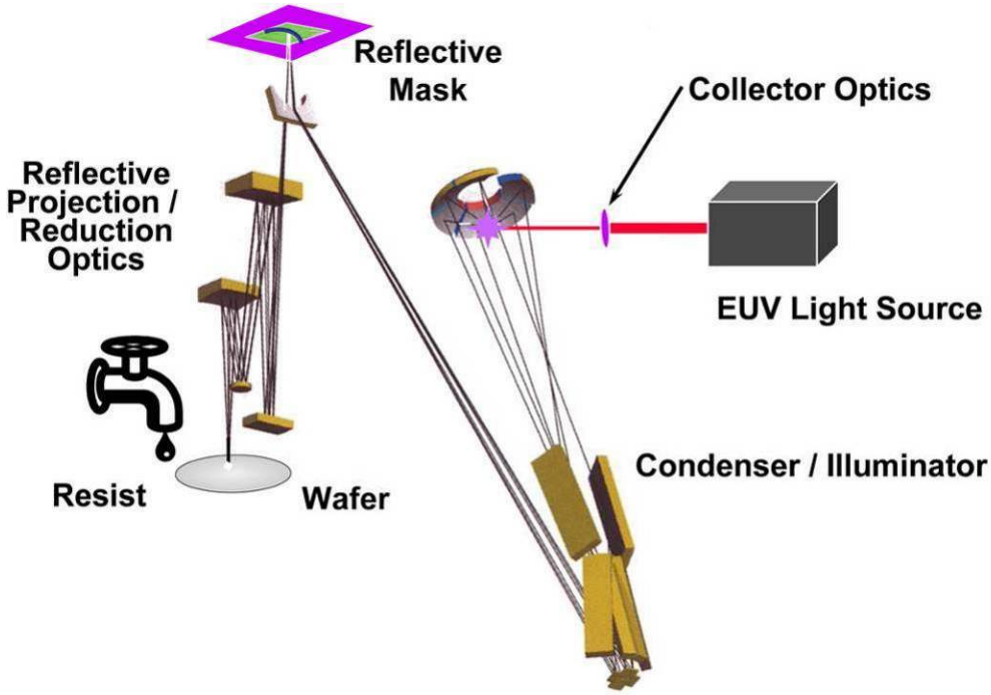

Figure 1.4: Illustration of EUV lithography system

1.1.2.2 X-ray Lithography

X-ray corresponds to photons at wavelength of 0.01~0.1nm (soft X-ray) and 0.1~10nm (hard X-ray). Having ultra-short wavelengths, X-rays overcome the diffraction limits of optical lithography, and allow replication of smaller feature sizes. X-ray lithography was initially proposed as a candidate for next-generation lithography [12]. Because of X-ray's penetrating nature, collimating mirrors or diffractive lenses are used in place of the optical refractive lenses to collimate the X-ray beam. X-ray lithography uses the shadow printing method where an X-ray mask is placed in proximity of a wafer. The X-ray mask consists of an X-ray absorber (made of heavy elements such as Au) on an X-ray transparent membrane (such as SiC and Si_3N_4). Several prints at about 20 nm have been published [13]. Although it utilizes ultra-short wavelength photons, due to the finite size of the X-ray source and the finite mask-to-wafer gap, a shadow effect degrades the resolution at the edge of the feature. Because of its limitation of resolution and high

cost, X-ray lithography appears to have been abandoned for next generation lithography. Yet deep X-ray lithography (DXRL), which uses the wavelengths on the order of 0.1 nm to replicate patterns, is important for particular applications such as LIGA (a German acronym for Lithographie, Galvanoformung, Abformung, i.e., Lithography, Electroplating, and Molding), where the goal is to fabricate deep and even three-dimensional structures.

1.1.2.3 Electron-Beam Projection Lithography (EPL)

Efforts have been made to access shorter wavelengths by using particles such as electrons, ions or neutral atoms. Among them, the electron beam is more often studied since it is considered to be a cleaner beam source without causing ion contaminations/doping to the substrate being patterned. Typically, for electrons with energy level of 10-50 keV, the wavelength is less than 1 Å.

The scattering with the regular limitation for projection electron lithography (SCALPEL) [14-18] is one of the major EPL efforts initiated in Bell Labs, as shown in Figure 1.5. SCALPEL uses an ebeam mask which consists of a low atomic number element membrane covered with a patterned layer of a high atomic number material. The membrane scatters electrons weakly and to small angles, while the patterned high atomic number element layer scatters them strongly and to high angles. This allows the formation of a directional ebeam pattern which can be projected onto a wafer surface with much reduced feature sizes. An aperture is used at the back-focal plane to filter out the strongly scattered electrons to form a high contrast ebeam image at the wafer surface. The SCALPEL mask is much simpler and cheaper than an EUV mask.

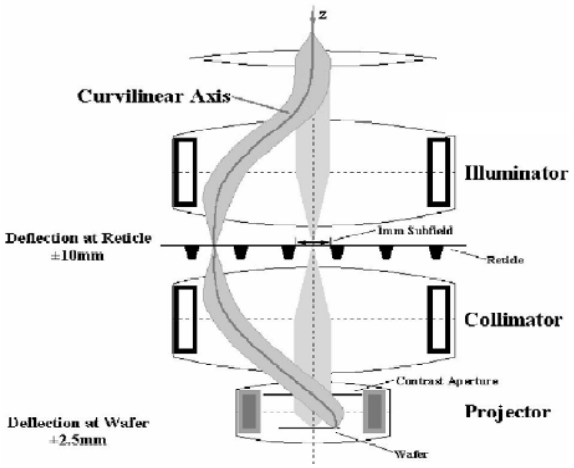

Figure 1.5: Illustration of Nikon's EPL system (2003)

Although shorter wavelengths are accessible with electrons, their Coulomb interaction greatly impairs the EPL throughput, known as the Boersch effect and Loeffler effect. As the electron beam current increases, the beam aberration also increases, which limits the achievable pattern resolution. The SCALPEL approach has been abandoned by major lithography tool vendors for

next generation lithography but it is still pursued by some research groups.

There are still some ongoing efforts to project election beams for lithography purposes. Recently, KLA Tencor proposed a different scheme of reflective EBL (REBL) [19-21]as shown in Figure 1.6. It replaced the SCALPEL mask with a programmable electron beam reflector array. This new approach claims to solve some issues of SCALPEL and could become a potential successor of SCALPEL.

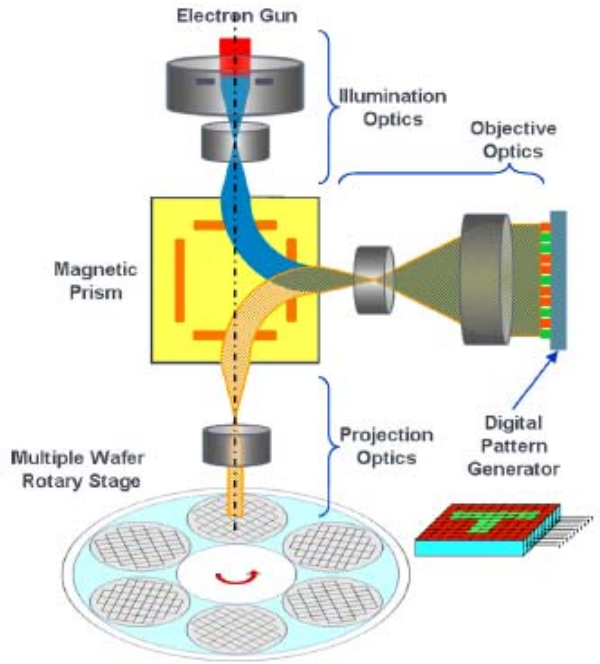

Figure 1.6: Illustration of REBL system by KLA Tencor (2009)

Other researchers have proposed Ion-beam lithography (IBL) [22, 23], which uses heavier ions (such as Ga) to achieve less beam aberration, high resolution and throughput, but this technique is not yet as mature as EPL. It also has the issue of unwanted ion doping. Improvements are required for better ion beam source and masks.

1.1.2.4 Nano-Imprint Lithography (NIL)

NIL is a method of fabricating nanometer scale patterns by mechanical deformation of imprint resist [24-30] and subsequent processes as shown in Figure 1.7. It is a simple and low-cost nanolithography process with high throughput and high resolution. It usually uses heat or UV light during the imprinting to cure the imprint resist.

Many efforts have been made to improve NIL resolution, throughput, uniformity and reliability. Commercial NIL tools are available both for research and mass production purposes. Compared with photolithography, EUVL and many other approaches, NIL can achieve high resolution and throughput at low cost which makes it very attractive for data storage applications

such as flash memory and magnetic bit-patterned media recording.

The major limitations for NIL are the imprint mold manufacturing, mold durability, pattern overlay and defects. Especially, making a large-size high-resolution imprint mold using currently available maskless pattern writers are unrealistic due to their low throughput at high resolution.

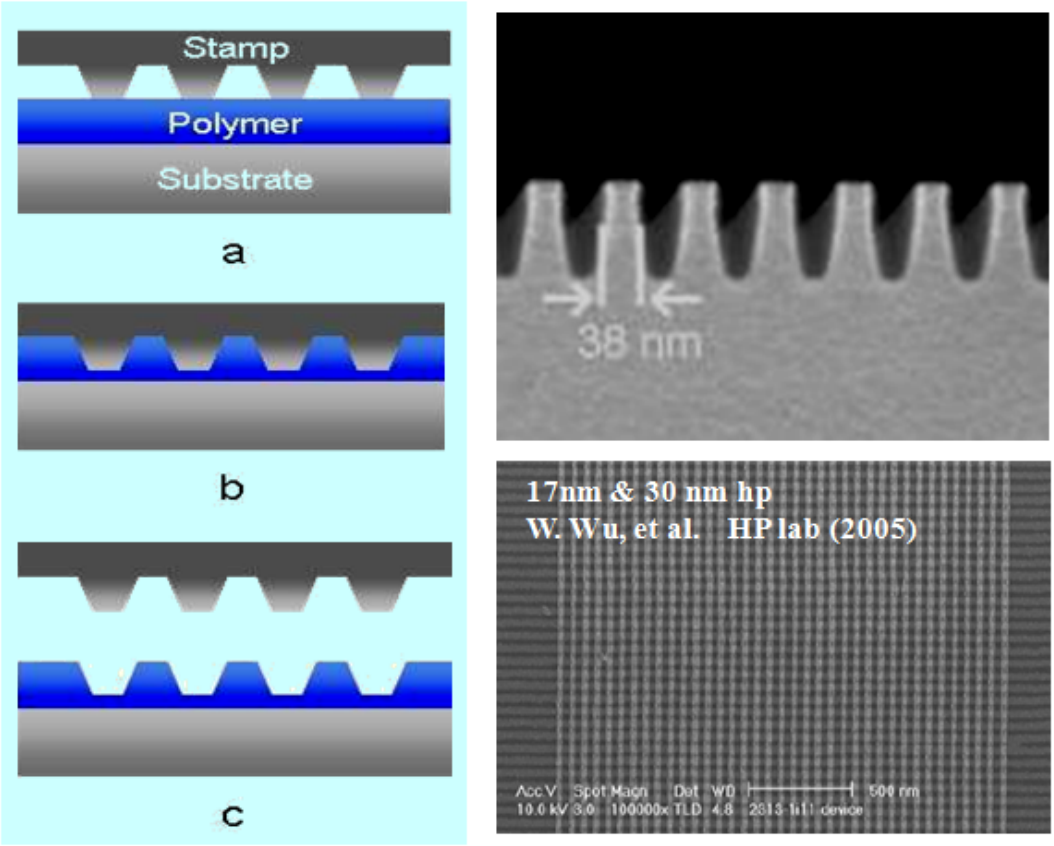

Figure 1.7: Example of high resolution nanoimprint lithography

1.1.2.5 Maskless Approaches

Approaches such as EUVL and NIL, use a mask or mold to perform a pattern transfer. This pattern replication approach greatly enhances the throughput of the nanolithography process but also causes many issues due to its gradual feature size reduction, such as the extremely high cost of reticules and increasing the production cycle time. Currently, the mask/mold production accounts for the major process costs which is considered as the technical bottleneck for both EUVL and NIL towards applications.

Many efforts have been made to develop maskless approaches [31] for high volume chip fabrication, such as electron beam direct writing lithography (EBDW) [32], focused ion beam lithography (FIBL) [33], scanning probe lithography (SPL) [34-37] and zone-plates-array

lithography (ZPAL). Usually, maskless lithography (ML2) refers to maskless approaches with significantly higher throughput than EBDW and can meet the requirements for high volume manufacturing.

1.1.2.6 Electron Beam Direct Writing (EBDW)

As shown in Figure 1.8, EBDW uses magnetic lenses to focus a shutter controlled single electron beam to do direct writing [32]. A beam size of a few nanometers is achievable by carefully designing the beam current and magnetic lenses. EBDW has been widely used for device prototyping, photo mask writing and some special fabrication. The conventional EBDW tool uses a single beam for writing with either vector scan or raster scan. One of the advantages of EBDW is its capability of working with numerous resist materials. Although EBDW has very good flexibility, it suffers from its extremely low patterning throughput due to its serial scanning requirement.

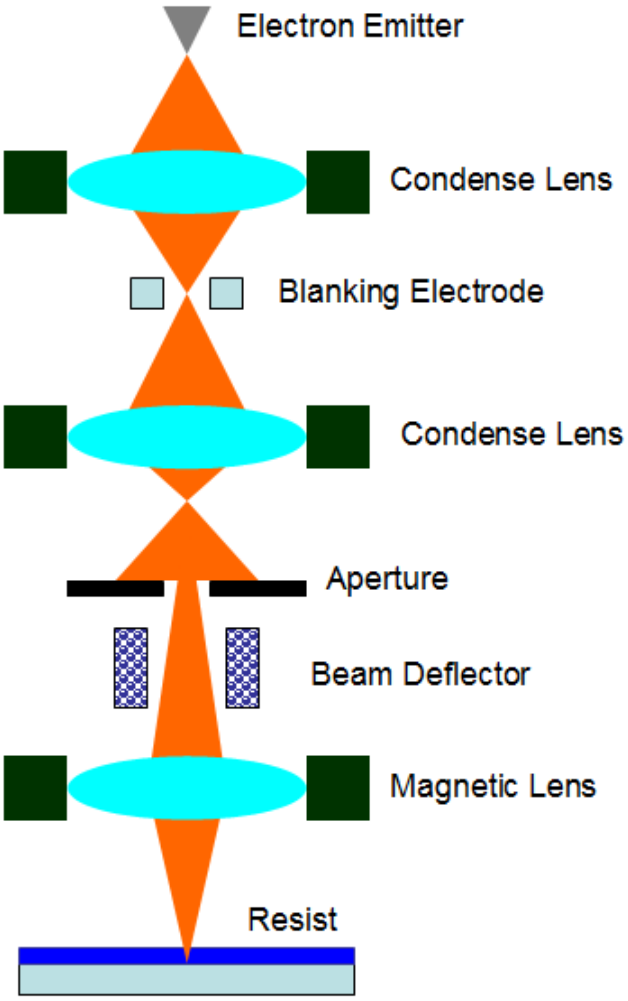

Figure 1.8: Illustration of direct electron beam writer

1.1.2.7 Parallel Electron Beam Lithography

Many maskless lithography systems are being developed based on the use of multiple electron beams in a parallel scanning arrangement [38, 39] or shaped electron beams [40] to enhance their throughputs. The parallel scanning of the beams can greatly improve the lithography throughput. For example, the maskless tool developed at MAPPER lithography [41] uses up to 10,000 parallel electron beams (http://www.mapperlithography.com/) to write simultaneously (shown in Figure 1.9). MAPPER and other similar tools have managed to greatly improve the performance of maskless lithography and reduce lithography costs.

However, the crosstalk between one electron beam and its neighboring beams can disturb one another because of the Coulomb repulsion similar to that in EPL approach. And it limits the spacing and current of the beams. Currently, the direct parallel e-beam writers still cannot meet the throughput requirement for mass production.

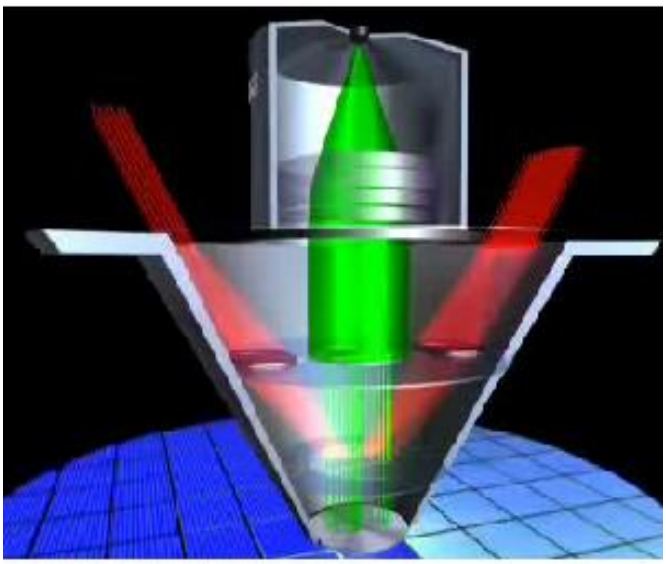

Figure 1.9: illustration of MAPPER system (2009)

1.1.2.8 Optical Maskless Lithography

Typical optical maskless approaches use conventional optics or optics arrays driven by an addressable array of light modulating elements to generate the pattern. Usually, micro-mechanical

spatial light modulators (SLMs) are used to produce an image to be projected on the wafer. As an example, zone-plate-array lithography (ZPAL) uses a zone plate array to focus individually modulated light beams onto the substrate [42-48]. A computerized SLM is used in ZPAL to control the light input to each element during scanning. A schematic of ZPAL is shown in Figure 1.10. Although this approach is capable of optically generating arbitrary patterns, the resolution is still diffraction limited. A shorter wavelength is still needed to generate finer feature sizes.

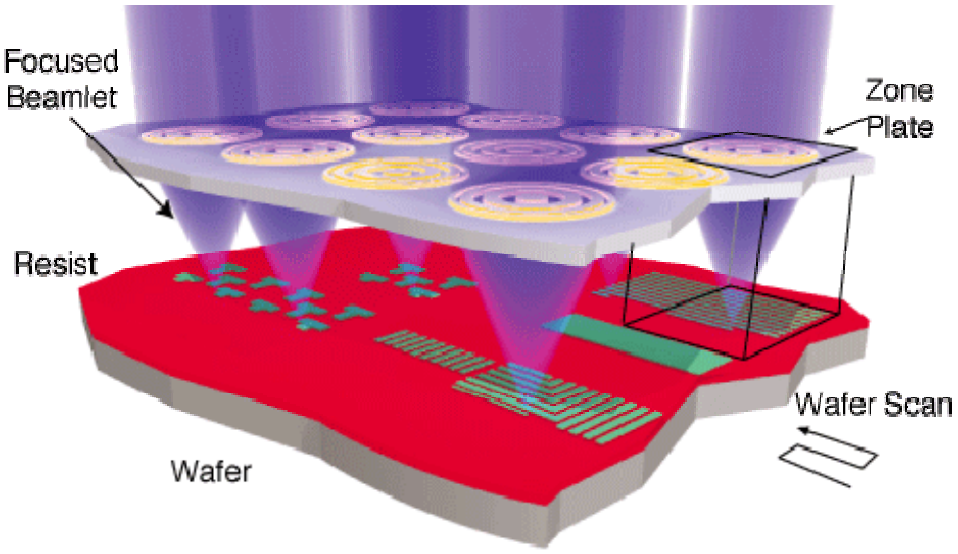

Figure 1.10: illustration of ZPAL system

1.1.2.9 Molecular Self-Assembly Lithography

Although top-down schemes are still currently dominant over bottom-up schemes in both manufacturing and research there is a possibility that bottom-up schemes may take over as the primary nanolithography approach because of the ever-increasing complexity and cost of the top-down schemes. The bottom-up scheme seeks to assemble smaller entities into larger and more complex ones. Currently, molecular level assembly is the major approach including block copolymer self-assembly (PSA), DNA engineering, and shaped molecules (e.g. bis-peptides). Among them, PSA is compatible with thin film technology and is particularly well studied because of its ability to generate nanoscale patterns in a large scale [49-51]. PSA has invoked many interests especially in the data storage related applications such as bit-patterned magnetic storage media or high density flash memories. In theory, PSA is expected to produce structures down to a few nanometers by optimizing the polymer structures and assembly conditions. Experimentally it was also shown that PSA can be guided externally to form more complicated patterns, as shown in Figure 1.11. A dot density reaching 10 Tbit/in2 was recently demonstrated [52].

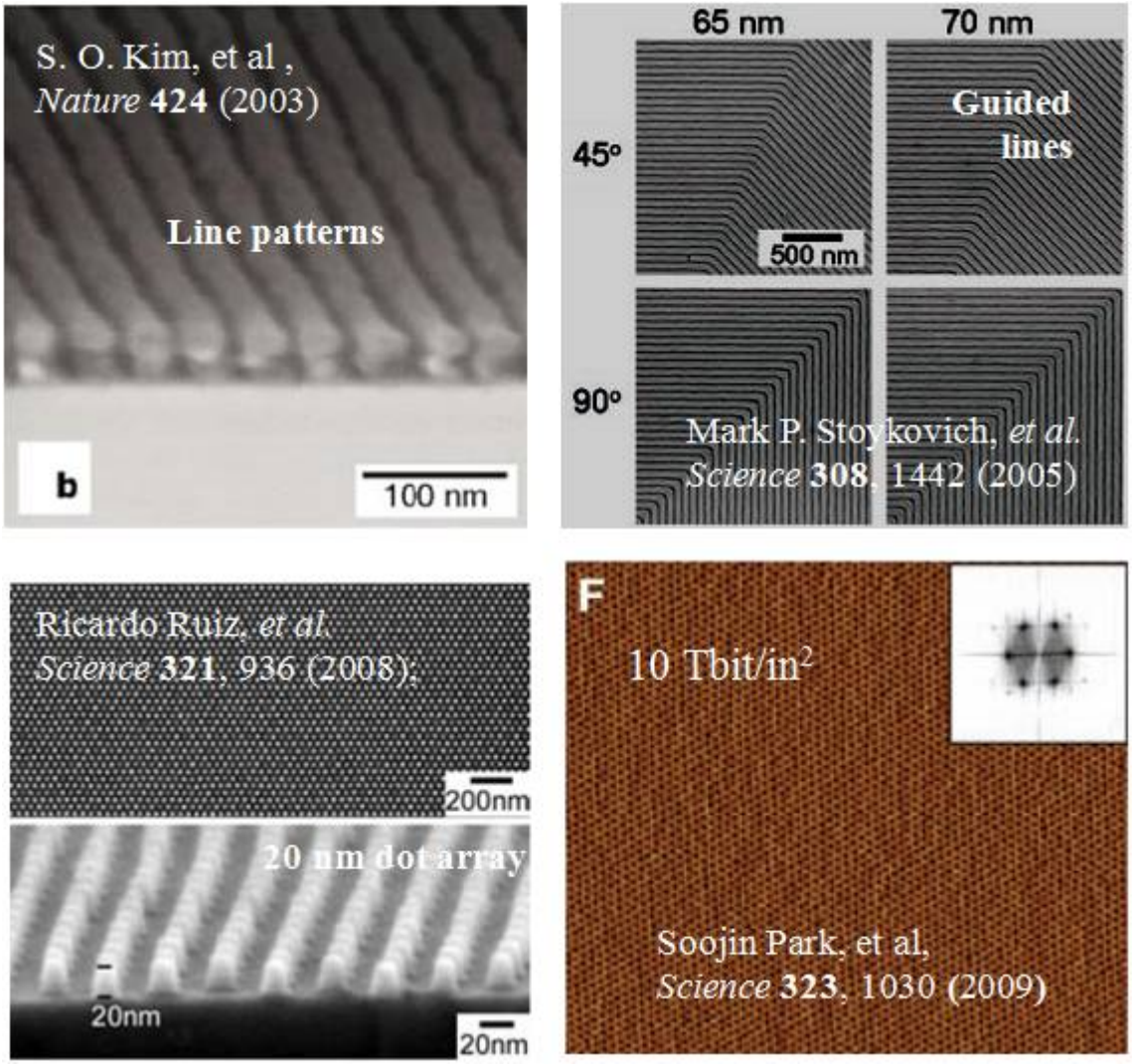

Figure 1.11: illustration of PSA results

1.2 Introduction to Plasmonic Techniques

1.2.1 Introduction to Surface Plasmons

Surface plasmon polaritons (SPPs) are the collective motions of the surface electrons at the interface between a metal and a dielectric [53-55]. Some metals exhibit strong SPPs resonance at optical frequencies. Using proper metal structures and illumination, SPPs can be excited and coupled with an incident optical field through its interaction with the free electrons of the metal as shown in the schematic in Figure 1.12.

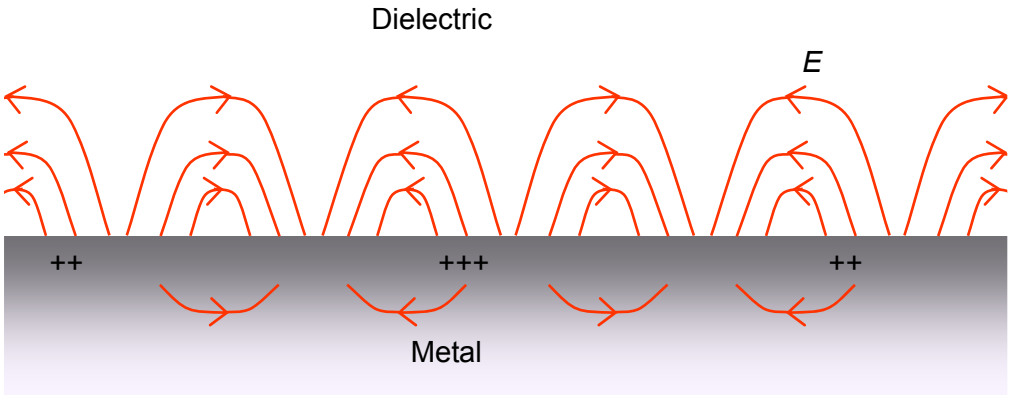

Figure 1.12: Schematic of the charges and the electromagnetic field of SPPs propagating on a surface.

Confinement of the electrons near the interface produces strong enhancement of the electromagnetic near-field in the vicinity of the SPPs. Numerous research fields have been focused on the control and confinement of this strong, localized enhancement, including the fields of surface chemistry, physics, biology and nanoscale engineering [56-59]. The use of SPPs opens up potential applications in nanoscale optical spectroscopy [60], surface-enhanced spectroscopy, surface plasmon resonance sensing [61, 62], and nanolithography[63].

Because of the coupling between the SPPs and the optical field, the optical energy transmission through subwavelength holes can be greatly enhanced [64-68]. As observed in experiments, transmission through subwavelength metallic hole arrays can be orders of magnitude greater than the prediction of zero-order transmission of standard aperture theory [68]. Theory and experimental evidence show that this effect is due to the coupling of incident light with surface plasmons at the interface between the metallic film and the surrounding dielectric media.

The coupling between SPPs and optical fields produces a much smaller SPP wavelength than that of the incident light. The dispersion relation for the SP at an interface between a semi-infinite metal and dielectric materials is expressed as [69]:

$$k_{sp} = \sqrt{\frac{\varepsilon_1 \varepsilon_m}{\varepsilon_1 + \varepsilon_m}} \frac{2\pi}{\lambda_0}$$

where ksp is the SP wave vector, λ0 is the light wavelength in vacuum, ε1 and εm are the permittivities of the dielectric and metal, respectively. A typical SP dispersion curve based on the above equation is illustrated in Figure 1.13.

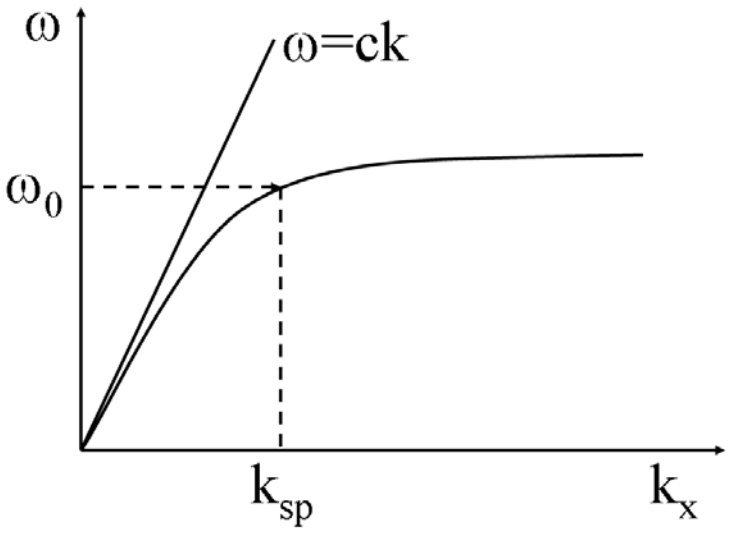

Figure 1.13: A typical dispersion curve for surface plasmons. To excite surface plasmons by an incident light beam at a specific frequency, the momentum mismatch between them has to be compensated.

Because of the momentum mismatch between the SPPs and the excitation light, a compensation coupling mechanism is a necessity to excite the SPPs. The creation of a grating in a metal film is considered as one of the best SPP couplers because it can effectively compensate the momentum mismatch and guide the propagation of SPPs. The dispersive property of SPPs offers access to much shorter wavelengths of surface waves than the excitation light wavelength, and this promises the potential of high-resolution imaging / lithography at a length scale beyond the diffraction limit.

1.2.2 Plasmonic Nearfield Microscopy

Nearfield scanning optical microscopy (NSOM) uses a scanning probe to scan in the nearfield of the sample. This has been applied extensively in the studies of biology, material science, and data storage. Although NSOM is capable of achieving a resolution well beyond the diffraction limit of the light, its applications are somewhat limited by the strong attenuation of the light transmitted through the subwavelength aperture, making it inappropriate for the applications such as high-speed probing and high-throughput nanolithography. Obviously, a subwavelength optical spot size with high light intensity is very helpful for the aforementioned applications.

The application of plasmonic coupling with focusing structures can greatly enhance the transmission through a sub-diffraction-limited spot which enables probing the sample in the nearfield with high resolution and high efficiency [70].

As shown in following Figure 1.14, a set of conical gratings with a subwavelength aperture at the apex of the cone has been fabricated in a thin Al film deposited on a tapered fiber tip. The gratings geometry can excite SPPs and guide the SPPs propagation towards the aperture apex. To obtain the best transmission through the aperture, the geometry of the plasmonic structure is optimized to provide the constructive interference at the center aperture.

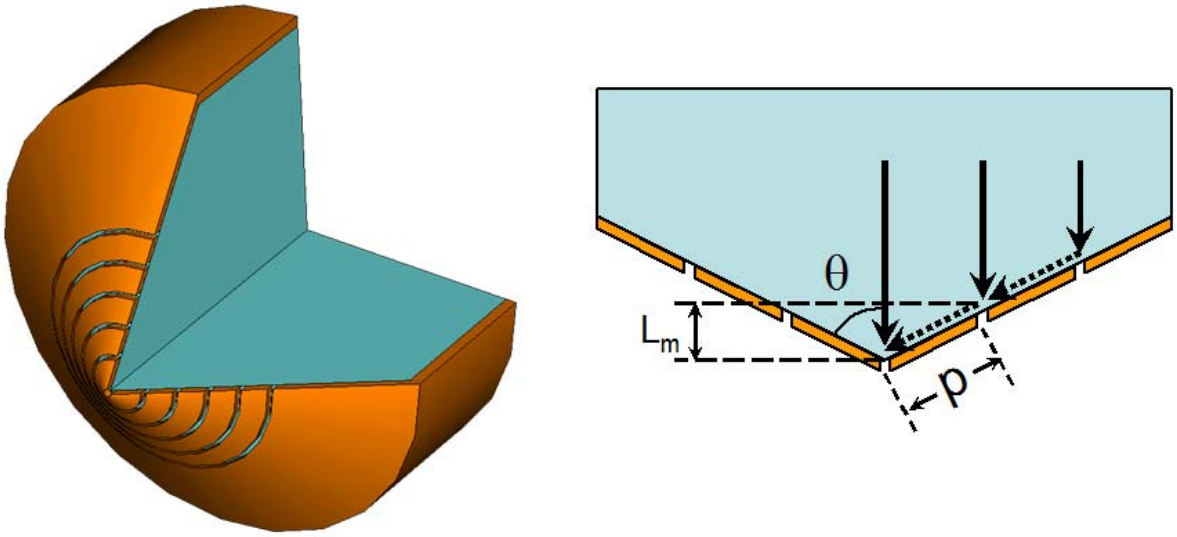

Figure 1.14: (left) Schematic drawing of the conic plasmonic structures. (right) Illustration of interference between the SPPs waves generated by the inner rings and those transmitted SPPs waves from the outer rings. Solid and dashed arrows represent incident light and SPPs respectively.

The following 3-D simulation result (calculated by commercial electromagnetic wave software, CST Microwave Studio) shows the optical field intensity of the plasmonic structures normalized to the intensity without rings (Figure 1.15). The peak enhancement factor of about 36 is observed at 365nm, which is exactly our designed UV wavelength. The cross-sectional view of the intensity profile at the plane near the aperture shows a very good field confinement with a spot size of ~100nm along the x direction and ~85nm in the y direction. This asymmetry produced by the symmetric structure is due to the horizontal polarization of the incident light.

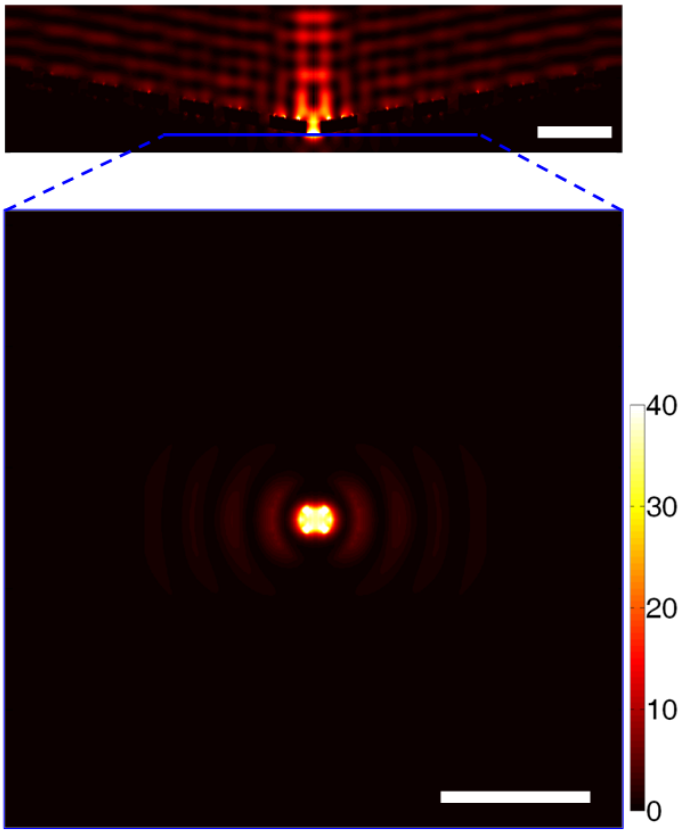

Figure 1.15: Tip side view (top) and cross-sectional view (bottom) of simulated intensity of the nearfield of the plasmonic structures. The scale bars is 500nm.

1.2.3 Plasmonic Nearfield Nanolithography

As shown in Figure 1.16 below, this plasmonic NSOM can also be used in nanolithography applications. During the lithography process, a laser beam at the wavelength of 365nm was coupled into the NSOM plasmonic tip to expose a positive photoresist. A best pattern linewidth of 80 nm was demonstrated. Similar exposure results through the tip without the plasmonic structures were only obtained by using 10 times higher input power.

This NSOM based approach allows us to utilize a light source with longer wavelength to do nanolithography. However, it still cannot overcome the limitation of scanning probe based lithography approaches due to its slow scanning speed. In order to meet the requirement of real world applications, the scanning speed needs to be at least one million times faster.

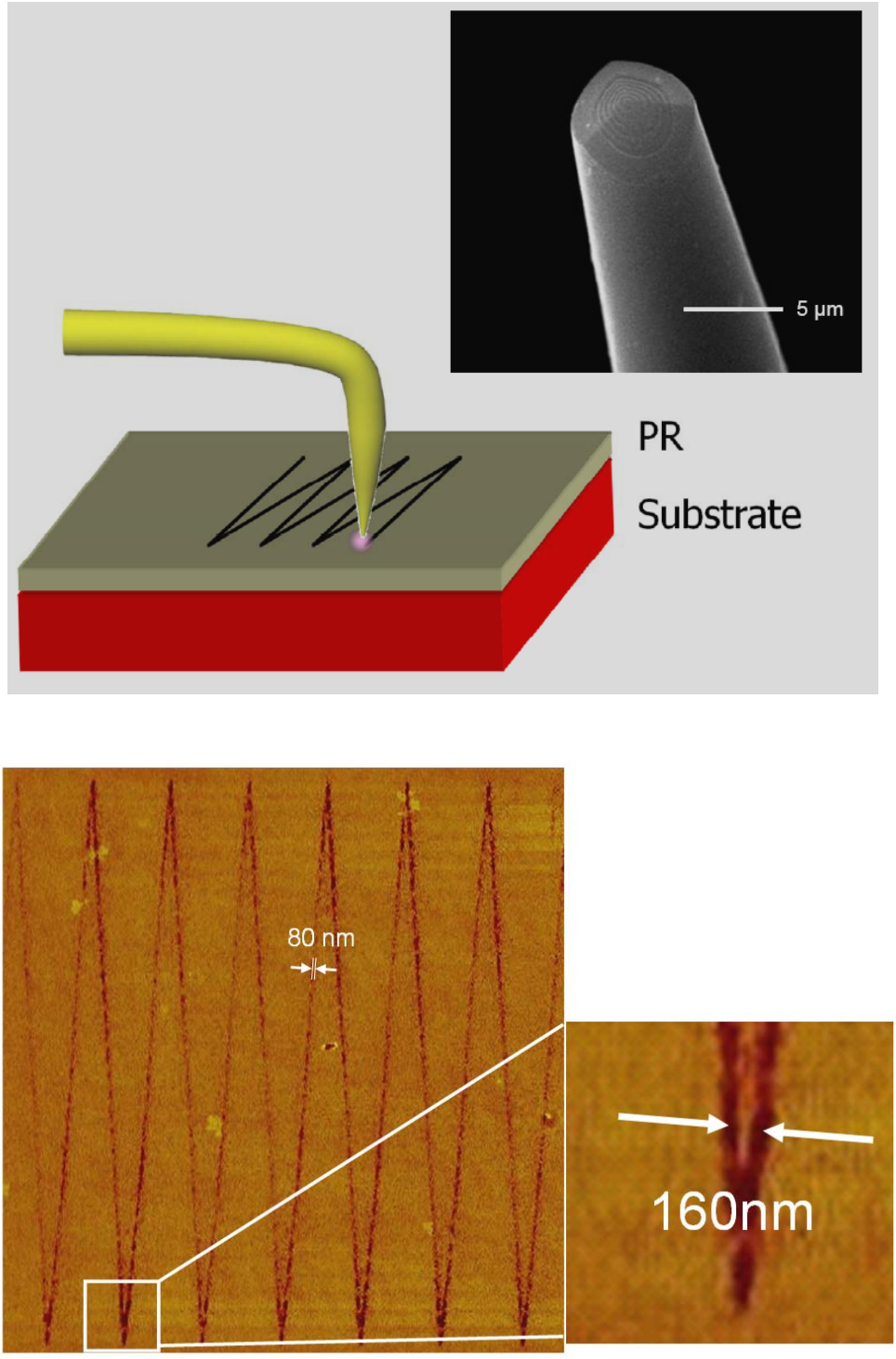

Figure 1.16: (top) NSOM probe consists of nano-structured plasmonic structures being fabricated on the end of an optical fiber. (bottom) AFM image of the photoresist after near-field scanning exposure using the plasmonic structures.

1.3 Introduction to Hard Disk Drive (HDD) Technology

In 1878 Orberlin Smith introduced to the world the idea of magnetically storing the electrical signals produced by the telephone onto a steel wire. More than one hundred and thirty years later, and after transitioning from wires on drums recording analog signals to disks capable of storing digital data, magnetic recording has become the overwhelmingly dominant computer data storage technology. The current device of choice is the hard disk drive (HDD), a non-volatile data storage system, which stores digitally encoded data on a rotating disk coated with magnetic layers. Since the first HDD was introduced in 1957 by IBM, the basic operation principles are almost unchanged. Today's HDD is still the main mass storage device for computers and networks due to its advantages in storage capacity, cost per unit storage amount, data access time and storage reliability. The structure of a HDD is shown in Figure 1.17. Usually the components inside a HDD can be divided into four main sub systems. They are the magnetic read/write heads, magnetic disks and head-disk interface (HDI); a printed circuit board with data detection electronics and write circuit; a mechanical servo and control system, including spindles, actuators, suspensions and control chips; interface to a microprocessor and power supply.

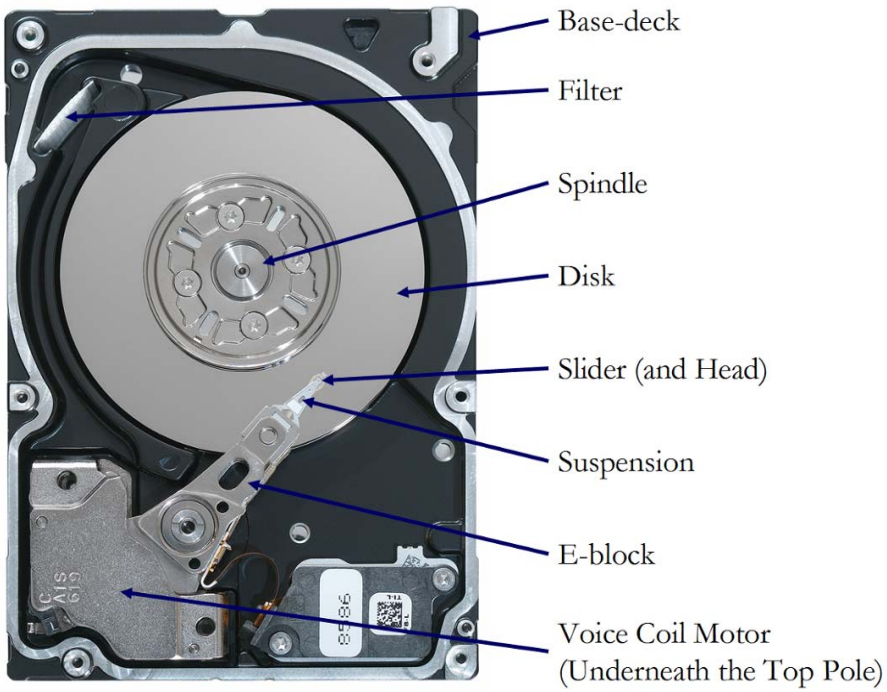

Figure 1.17: Structure of a modern HDD. (Source: Seagate Technologies)

Modern HDDs use read and write transducers positioned by air bearing sliders a few nanometers above a disk (made with a magnetic medium coating the rotation of which produces linear speeds of tens of meters per second) to access the data. Figure 1.18 shows an illustration of the standard perpendicular recording scheme in a HDD where the transducers are located at the

vertical trailing end of the scanning head.

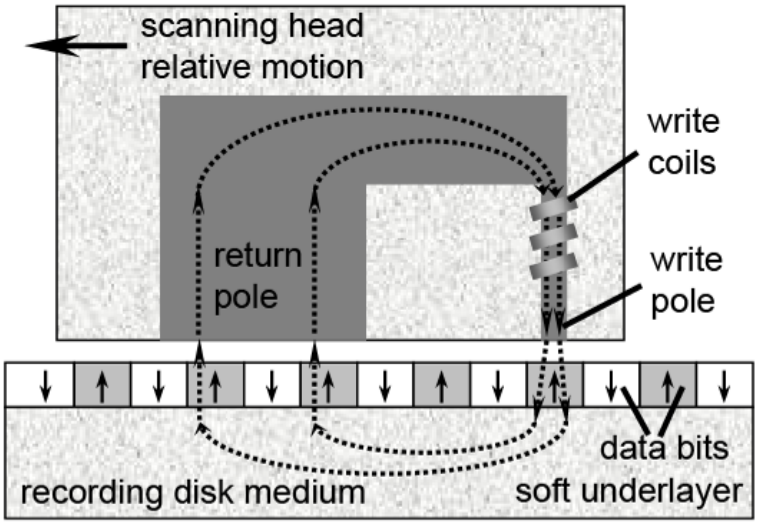

Figure 1.18: Schematic of perpendicular recording HDD systems. In a conventional HDD, a perpendicular recording head is working above a disk medium where the data are stored as vertical magnetized bits. The write transducer, consisting of write coils, a write pole, and a return pole, is located at the vertical trailing end of the scanning head.

As shown in Figure 1.19, the areal recording density (AD) of HDDs has been doubling roughly every two years. Various technology innovations and breakthroughs including thin film head and disk technology, giant magnetoresistance (GMR) heads and the use of perpendicular recording in place of longitudinal recording, have helped to maintain this trend.

The mechanical operation of the head-disk assembly relies on an air bearing film between the slider and the spinning disk for a stable self regulating head media spacing (HMS) as shown in Figure 1.20. The HMS includes the thickness of the protective layers- slider and disk diamond-like-carbon (DLC) overcoats and disk lubricant- and the physical spacing between the read/write transducer and the disk, the so called flying height (FH). Figure 1.21 shows the continuous reduction of FH over the years. A reduced but still stable FH of a slider mainly relies on a delicate design of the slider's patterned surface, called the air bearing surface (ABS), opposite to the disk surface. The relative motion between the slider with a well designed ABS and the disk creates an air pressure field that can stably sustain the slider's FH. The evolution of the slider and ABS is shown in Figure 1.22. As a result of the rapid development of the hard disk drive, the FH has dropped to sub 2 nm in order to achieve higher AD.

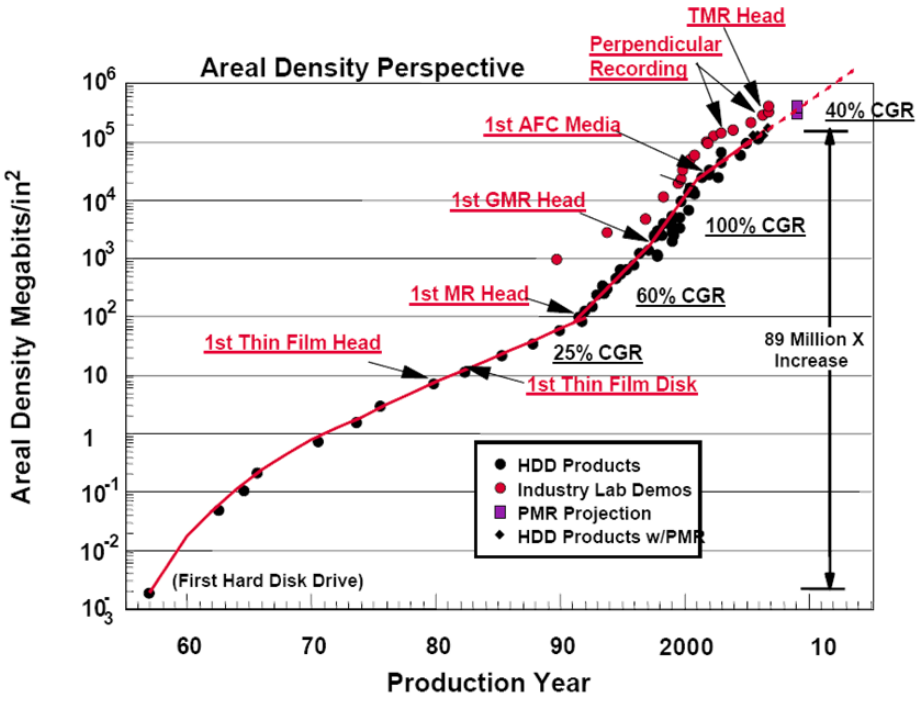

Figure 1.19: Areal density growth trend of HDD. (Source: Ed Grochowski 2007)

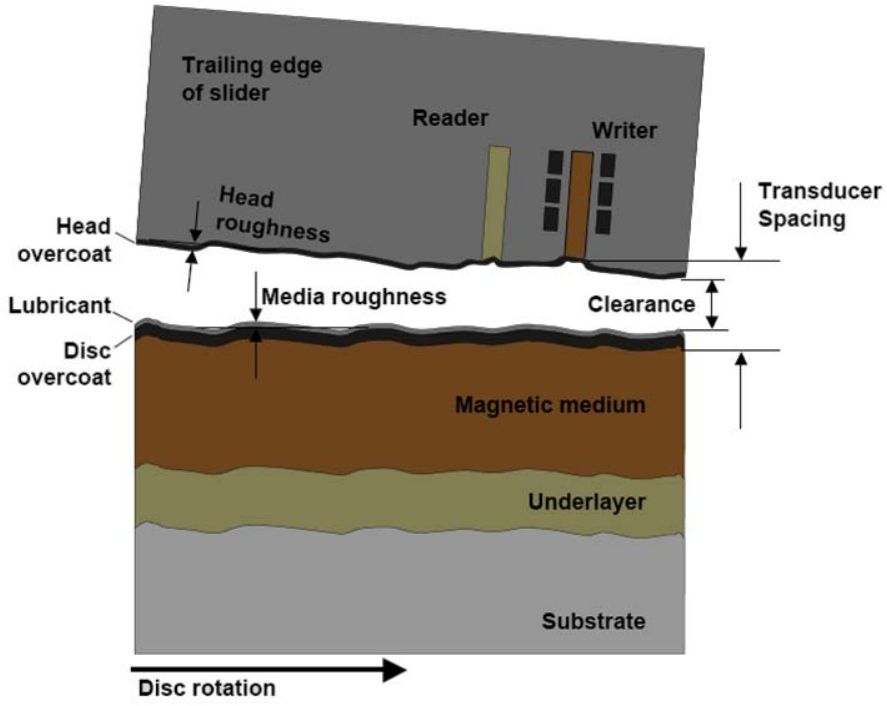

Figure 1.20: Illustration of head-disk interface. (Source: Seagate Technologies)

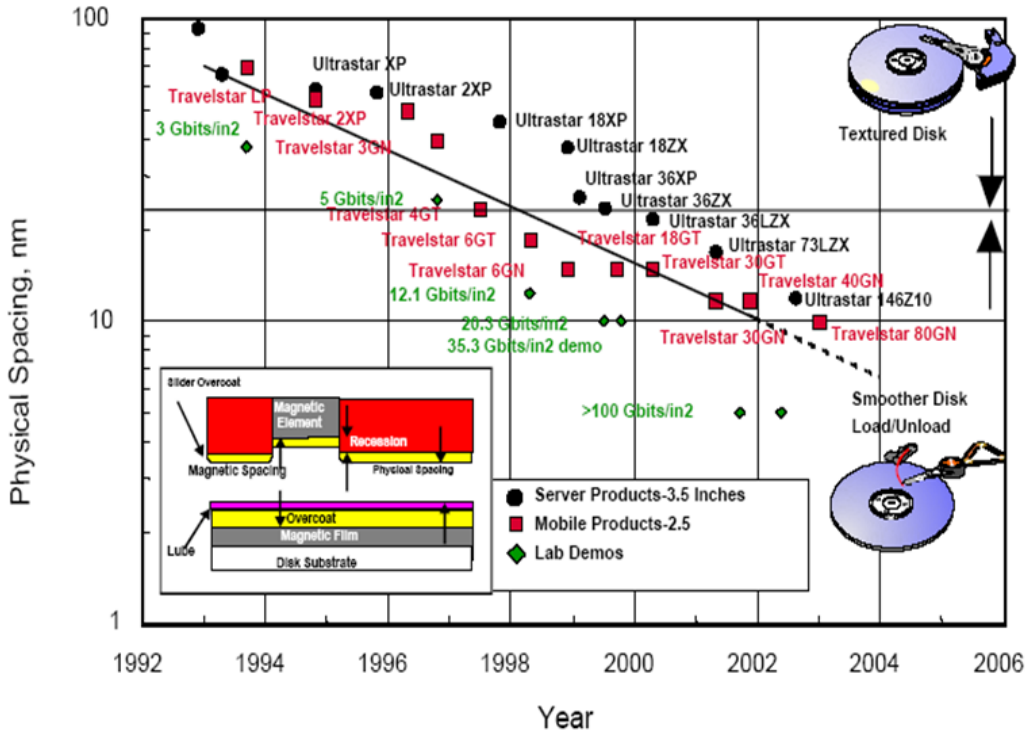

Figure 1.21: trend of reduction of physical spacing in head-disk interface. (Source: Hitachi Global Storage Technologies)

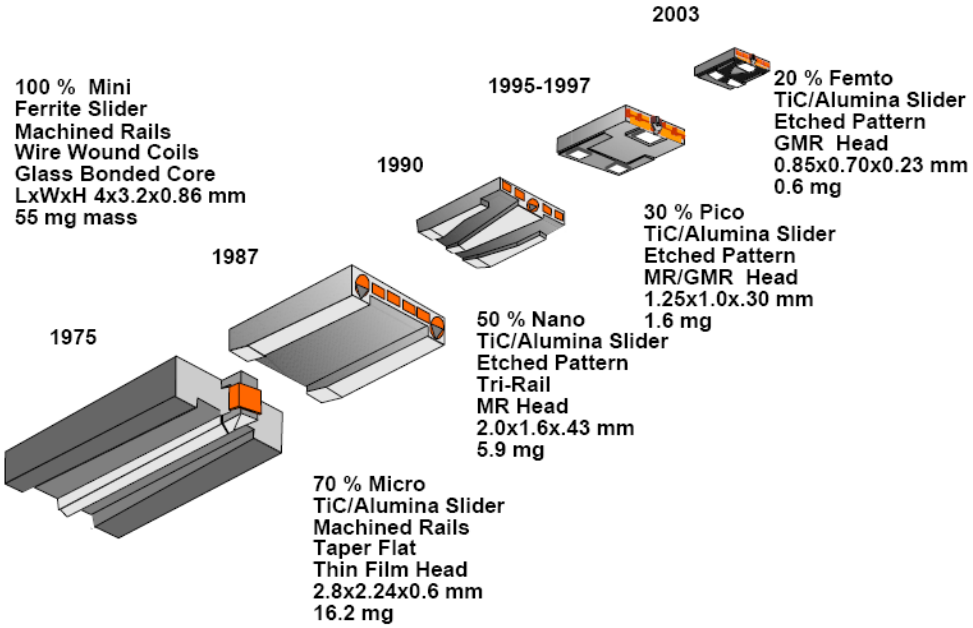

Figure 1.22: Advancement of HDD read/write sliders. (Source: Hitachi Global Storage Technologies)

Today, the recording AD of HDDs based on perpendicular recording technology has exceeded 500 Gb/in^2. However, the recent shift from longitudinal to perpendicular recording is only a short term solution; its ultimate AD is expected to be limited to about 1 Tb/in^2. At this point the AD of conventional magnetic recording will reach the superparamagnetic limit where the ambient thermal energy and neighboring bit polarizations are able to change the direction of the magnetic moment for a single bit. Several solutions have been proposed for further increase in AD but two of the most promising ones are heat assisted magnetic recording (HAMR) [71-73] and the use of bit-patterned media (BPM) [74-78]. Although there are debates about which approach will eventually succeed, it is conjectured that some combination of the two approaches will ultimately enable ADs of 300 Tb/in^2. In the following chapters, we will also discuss the applications of HAMR and BPM.

1.4 Scope and Organization of Thesis

This dissertation focuses on using surface plasmons and advanced airbearing surface techniques to achieve high throughput and high resolution maskless pattern writing.

It is organized into 7 chapters. Besides this first chapter which attempts to provide a brief background of current nanolithography techniques, the fundamentals of surface plasmons and the status of HDD technologies, the other 6 chapters are organized as follows.

Chapter 2 focuses on a variety of novel plasmonic nanostructures, the so called plasmonic lens (PL), which utilize surface plasmons to create high-intensity nanoscale light sources for lithography purposes. Numerical studies are presented to explain their working principles, designs and performances.

Chapter 3 is dedicated to the development of a high speed plasmonic flying head using advanced airbearing surface technology. Designs, simulations, fabrication and testing results are presented.

Chapter 4 is dedicated to the development of resist and media structures including the media tribological design, fabrication, and resist thermal analysis.

Chapter 5 describes the development of the maskless plasmonic lithography system with the integration of the plasmonic flying head with the PLs, novel lithography medium and optical/mechanical/electrical testbed.

Chapter 6 presents the plasmonic nanolithography results and discusses the future directions of the work.

Finally, Chapter 7 summarizes the work presented in this thesis and discusses the potential of plasmonic nanolithography in current and future applications.

Chapter 2 Plasmonic Lens (PL)

2.1 Plasmonic Resonance Structures

The plasmonic nanostructure used in this work serves as a near-field focusing lens which can effectively concentrate optical energy into a nanoscale spot. Focusing light to a highly confined spot has numerous applications in lithography, imaging and data storage. The smaller spot size of the focused light allows the formation of images with higher resolution and enables the writing patterns with higher density. Great efforts have been devoted to achieving smaller light spot sizes. The nearfield scanning optical microscope (NSOM) probe is one common way to obtain a high confined light spot. This NSOM probe can be used to study optical properties as well as to accomplish lithography. However, the transmission through the aperture of the probe is extremely low for subwavelength size apertures. The transmission normalized by the aperture area is proportional to $(d/\lambda)^4$ [79], where d is the diameter of the aperture and λ is the wavelength of illumination light in free space. As an example, the optical power transmission of a NSOM probe with a sub-100 nm opening is typically on the order of 10^{-5} to 10^{-7} [79], resulting in a very low throughput for both imaging and lithography applications. Clearly, a light source with subwavelength size and high intensity will be very useful for many applications including nanolithography, high-density optical and/or magnetic data storage, nanospectroscopy, biosensing, molecular trapping, and so forth.

As discussed in previous chapters, focusing light can also be realized by focusing surface plasmon polaritons (SPPs) by taking advantage of its short wavelength. Because SPPs can be excited by incident light on some metallic interface to propagate with long decay lengths, various structures (in Figure 2.1) have been proposed to focus light to a tiny spot by utilizing SPP [80-84].

One type of plasmonic structure is the SPPs grating which uses a series of gratings to build constructive SPPs interference to concentrate optical energy, such as the bull's eye aperture (in Figure 2.1(e)). The bull's eye aperture is a single nanoscale hole surrounded by circular gratings which can excite and guide the SPPs propagation, thus it can dramatically enhance the evanescent field transmitted through the sub-wavelength hole [85, 86].This system was also demonstrated in a recording experiment by Betzig et al. [87, 88]. They used an optical fiber tapered to a 100 nm tip and coated with an aluminum film to deliver light to a recording medium in the presence of an external magnetic field.

The second type of plasmonic structure is the SPPs resonant aperture. Most of the common SPPs resonant apertures are essentially ridge apertures initially proposed for microwave frequency applications and later shown to also operate at near infrared and visible wavelengths [89-92]. As shown in Figure 2.1(a)~(d), many designs have been studied including C-shaped, H-shaped, I-shaped and bowtie apertures. Although the aperture shapes are quite different, they share the

same working principal. The long dimension of the rectangular aperture part is on the order of a wavelength to allow light that is polarized perpendicular to this dimension to propagate through the aperture. The ridge in the center of the aperture concentrates the electric field intensity by both the lightning rod effect and a localized SPP resonance. Similarly, other types of SPP apertures have been proposed such as the triangle aperture, modified C-shaped and the L-shaped apertures [93]. These SPP ridge apertures usually have strong wavelength dependency.

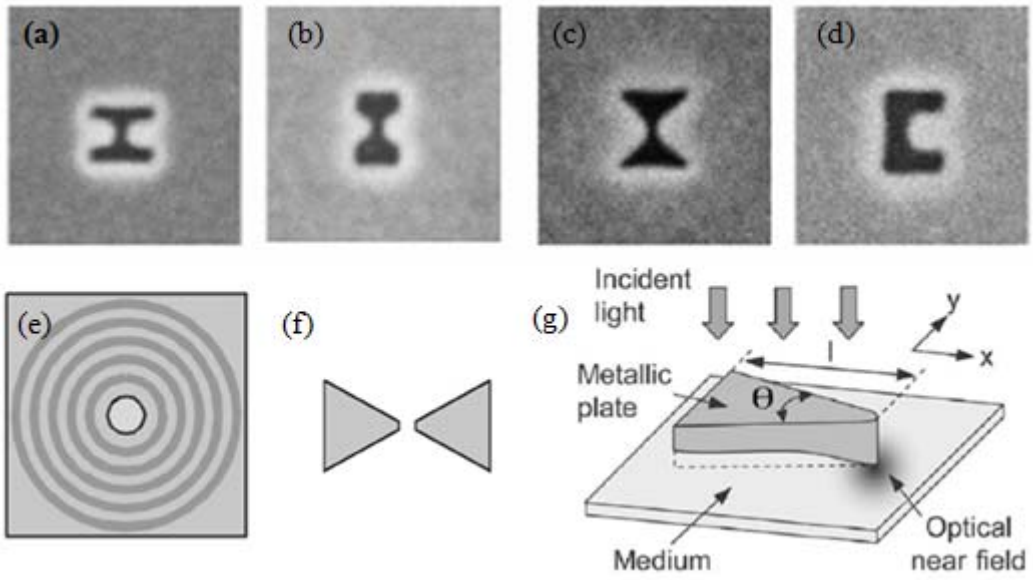

Figure 2.1: Examples of plasmonic resonance structure in literatures.

Similar to the ridge apertures, some SPP nano-antennas are also proposed to focus light in the nearfield. Among them, bowtie antennas as shown in Figure 2.1(f) are most widely studied. The antenna can couple the incident light with the electric field polarized along the long axis of the antenna. And the antenna tips also concentrate the electric field intensity by both the lightning pole effect and a localized SPP resonance working the same as the ridge apertures. By tuning the SP resonant frequency together with the dimensions of the antenna, it is possible to concentrate the surface charges at the points of the tips in order to generate large field intensities. The beaked triangle plate [94, 95] is a modified version of the SPP antenna (in Figure 2.1(g)), serving as one-half of a bowtie antenna. It has the tip of the triangle extending towards the metallic medium to ensure that the optical energy is locally concentrated in the medium. The mirror charges inside the metallic medium greatly enhance the SPP's coupling.

The plasmonic lens (PL) [96], as an extension of these structures, is a nano-scale aperture or antenna surrounded by a circular coupling grating on a metal film. The circular coupling grating excites the surface plasmon modes on the metal surface. The energy of the surface plasmon waves propagates along the direction normal to the slit of the gratings. As a result, the surface plasmon waves are focused at the center of the circular grating where the nanoscale aperture is located. The

focused surface plasmon waves enhance the energy transmission through the aperture. The transmission through the aperture is a subdiffraction-limited spot in its near field, which can be used as a virtual probe for optical maskless high-speed lithography with high resolution.

2.2 PL Performance Characterization

Because the new plasmonic nanolithography system uses a nearfield PL and ultrafast picosecond-pulsed laser to write on thermal type inorganic resists, the conventional parameters used to evaluate diffractive focusing lenses are no longer precise and effective. For this reason, we propose some new parameters to evaluate the lithographic performance of PL, and also discuss requirements for PL in high speed nanolithography in terms of the proposed parameters, including focus spot size, optical confinement, field enhancement, transmission efficiency, image contrast and lens working depth.

The focus spot size of a PL (D_L) is a function of the working distance, and it is evaluated by the full-width-half-maximum (FWHM) of the optical field at the working plane ($I_{(x, y)}$).

$$D_L = FWHM\ of\ I_{(x,y)}$$

D_L is one of the key parameters that determines the patterning feature size. For a linear resist, the exposure feature size is very close to D_L in terms of FWHM, but the writing feature could be quite different for resists with nonlinear responses, such as its finite exposure threshold, pattern shrinking and physical/chemical diffusion.

Another parameter, the optical confinement factor (Γ_L), could be more helpful for determining exposure threshold of a nonlinear resist. Γ_L is defined as the distance of the steepest optical field gradient (d_L) normalized by the spot size.

$$\Gamma_L = \frac{d_L}{D_L}$$

Γ_L is a nondimensional number which is important in characterizing the nonlinear response of the resists. For a nonlinear resist with an appropriate choice of exposure threshold, the feature with the best defined edges aligns with the position of the steepest field gradient. A smaller Γ_L helps generate smaller feature sizes with a better pattern edge definition.

The light enhancement factor (E_L) in this work is defined as the ratio between the peak light intensity (I_M) at the working plane and that of the incident light (I_0).

$$E_L = \frac{I_M}{I_0}$$

By comparing this number with that of a pinhole of the same size as the focus spot, we can intuitively determine how much the transmitted field is enhanced by the PL.

It is worth noting that E_L alone is insufficient to describe the lithographic performance of a PL, because a higher field enhancement doesn't necessarily mean a better PL efficiency for the same focus spot size. In practice, an important parameter in lithographic applications is the amount of

optical power obtainable from the focus spot.

The transmission efficiency (η_L) is the percentage of optical power that can be utilized to generate patterns. Ideally, the transmission efficiency (η_L) should be defined as the percentage of total incident optical power (P_{total}) absorbed by the resist layer within the area illuminated by the lens focus spot. But in practice, we use a nominal number:

$$\eta_L = \frac{P_L}{P_{total}} \times 100\%,$$

which is the ratio between the optical power within the focus spot at the working plane (P_L) and the overall incident power onto the PL, because the transmission efficiency can be greatly affected by the absorptivity and coupling properties of the resist layer.

The depth of focus (*DOF*) is defined as the range of working distance corresponding to ±10% change of the patterning feature size (*W*).

$$\text{DOF} = \text{ range for } \pm 10\% \text{ change of W}$$

DOF is one key parameter to ensure the patterning uniformity because of the evanescent decaying nature of surface waves. Usually during high speed scanning the working distance varies over a short range mainly caused by the substrate roughness and flatness, fabrication errors and some error dynamics in the high speed scanning process. A good PL design should be able to tolerate some of gap variations in practice.

2.3 Example Proposed PL Designs

2.3.1 Modified Bull's Eye

The previously discussed bull's eye structure has stimulated extensive interest in SPPs in the scientific community [85, 86]. However, its application is limited by the tradeoff between the greater transmission and the finer spot size. Here, we introduce a modified structure to overcome the limitations of the previous designs. We replace the partially through circular grooves with through ones. This scheme achieves better light confinement and higher energy transmission. The field penetration depth is also improved for applications of near-field nanolithography. Although this modification sacrifices the contrast performance of the focus spot by allowing light to be transmitted through the slits, this can be tolerated by using nonlinear resists with a higher exposure threshold.

The proposed structure is shown in the inset of Figure 2.2(a) where the light intensity profile along the dashed line is plotted. This numerical simulation to obtain this profile was performed using the commercial FDTD software (CST Microwave Studio) under a linearly polarized plane wave illumination. The polarization direction is along the y axis as shown in Figure 2.2(a). Under plane wave illumination the SPPs are excited at both sides of the lens and propagate towards the center [57, 97]. By tuning the period of the rings, the SPPs excited by multiple rings can form constructive interference. Also the thickness of the metal film is carefully chosen in order to

generate constructive interference between the top and bottom light spot. The focused SPPs launched through the center hole help generate a stronger field profile and improve the field depth. The simulated PL consists of a nano-aperture surrounded by 15 through rings on an aluminum film. The hole diameter, ring periodicity, ring width and aluminum layer thickness are 100nm, 250nm, 50nm and 80nm, respectively. Figure 2.2(c) and (d) show the maximum enhancement of about ~100 at the resonant wavelength of ~365 nm. And the intensity profile as a function of the off-plane distance is plotted in Figure 2.2(b). As shown, the FWHM of the obtained spot is about 80 nm near the lens surface, and it becomes larger as the distance increases. Figure 2.3 shows an SEM picture of fabricated modified bull's eye PL.

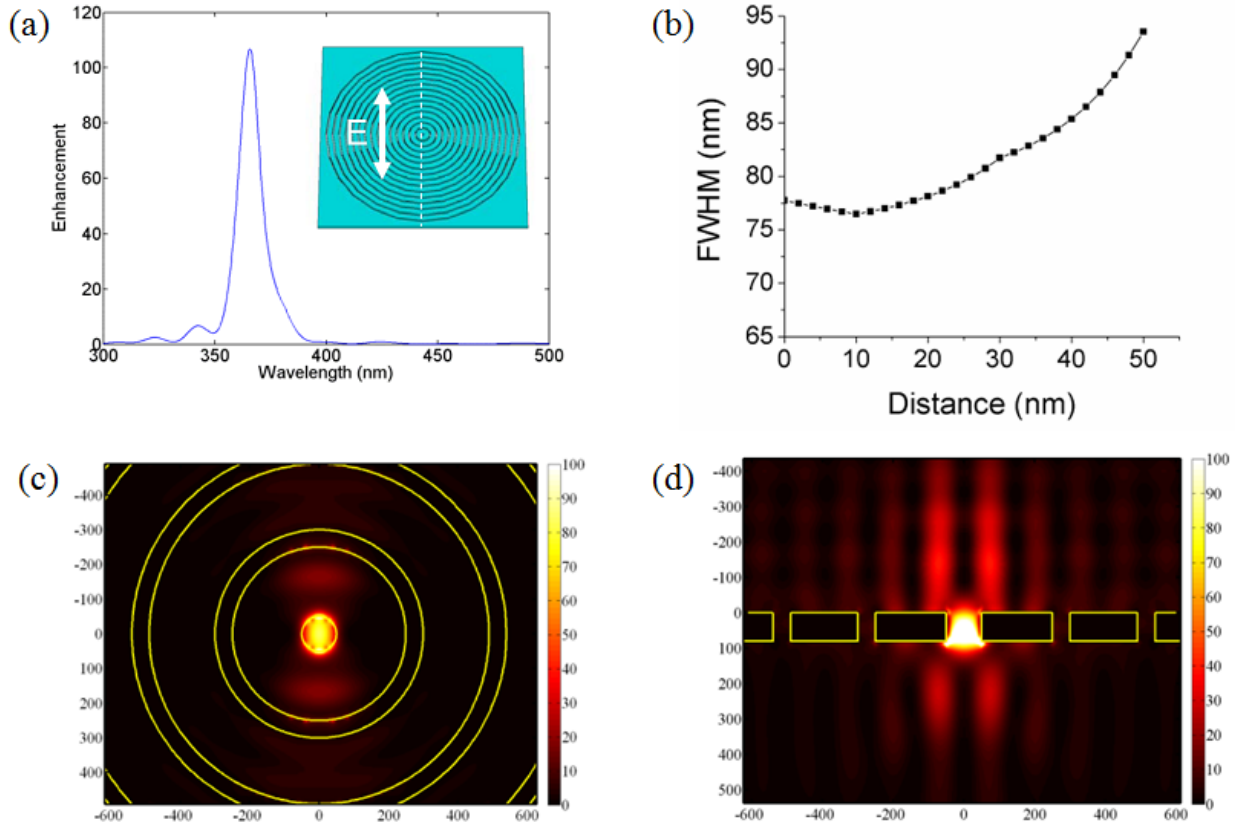

Figure 2.2: Numerical studies of the modified Bull's eye PL. (a) The light intensity profile along the dashed line shown in the inset. (b) The intensity profile plotted as a function of off-plane distance. (c) and (d) top and cross-section view of field profile showing the maximum enhancement about ~100 at the resonant wavelength of ~365 nm.

As discussed earlier, the lens transmission has a strong wavelength dependency and the modified bull's eye design relies on long distance propagating SPPs to concentrate the optical energy at the center hole. Therefore, this design occupies a relatively large area and also limits the choice of metals. At the optical range only a few metals can support long distance propagating SPPs with reasonably small decays in the propagation direction, such as aluminum, silver, copper

and gold. Because the poor mechanical properties of these metals can result in reliability issues during high-speed scanning, it is highly desirable to find some other designs which allow use of more durable metals as PL materials such as chromium. But when aluminum is replaced by chromium in modified bull's eye designs, the intensity enhancement is significantly reduced by more than two orders of magnitude. For this modified bull's eye PL, an optimized design would have about a 150 nm spot size with an enhancement factor only about 3.

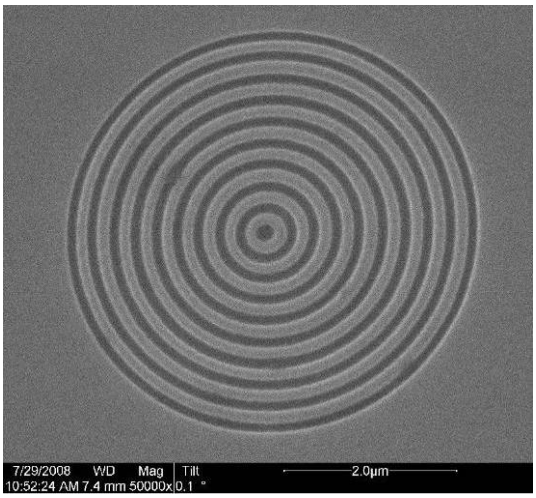

Figure 2.3: An SEM picture of modified Bull's eye design

2.3.2 H-shaped PLs

In the flying-head PL system, the PL is fabricated on a chromium thin film because chromium's exceptional mechanical properties can prevent damage of the PL when it flies with the flying head above the substrate. At the working wavelength of 355 nm, the propagation length of the surface plasmons on Cr surface is several hundred nanometers. To utilize the surface plasmons on a Cr film to enhance the transmission through the aperture, it is reasonable to design the PL with its diameter around 1 μm considering the limited propagation length of the surface plasmons on a Cr surface. Many studies [98-100] have been performed recently to obtain a subdiffraction-limited spot with high transmission through a ridge aperture at optical wavelengths. In order to design a lens using Cr, we replace the circular aperture of the modified bull's eye PL with a ridge aperture to enhance the intensity of the focus spot by the PL. And only a few rings are needed to achieve reasonable performance.

Our typical Cr-based PL has an H-shaped aperture surrounded by two rings as shown in Figure 2.4(a). Figure 2.4(b) shows the E field intensity distribution at a plane 15 nm away from the surface of H-shaped aperture (calculated by commercial electromagnetic wave software, CST Microwave Studio). The central spot is the focus generated by the PL. The incident light intensity is 1 and the peak intensity of the focus spot is about 4.09. The size of the focus spot, which is

defined by the full width of the half maximum (FWHM) intensity, is about 80 nm. The half-circular patterns in the intensity distribution are the direct transmission through the two rings surrounding the H-shaped aperture. The local maximum intensity at those patterns is about 1.58 corresponding to a contrast ratio of 2.6. With the proper choices of nonlinearity of resist and exposure condition, their intensity can be well under the exposure threshold of the resist.

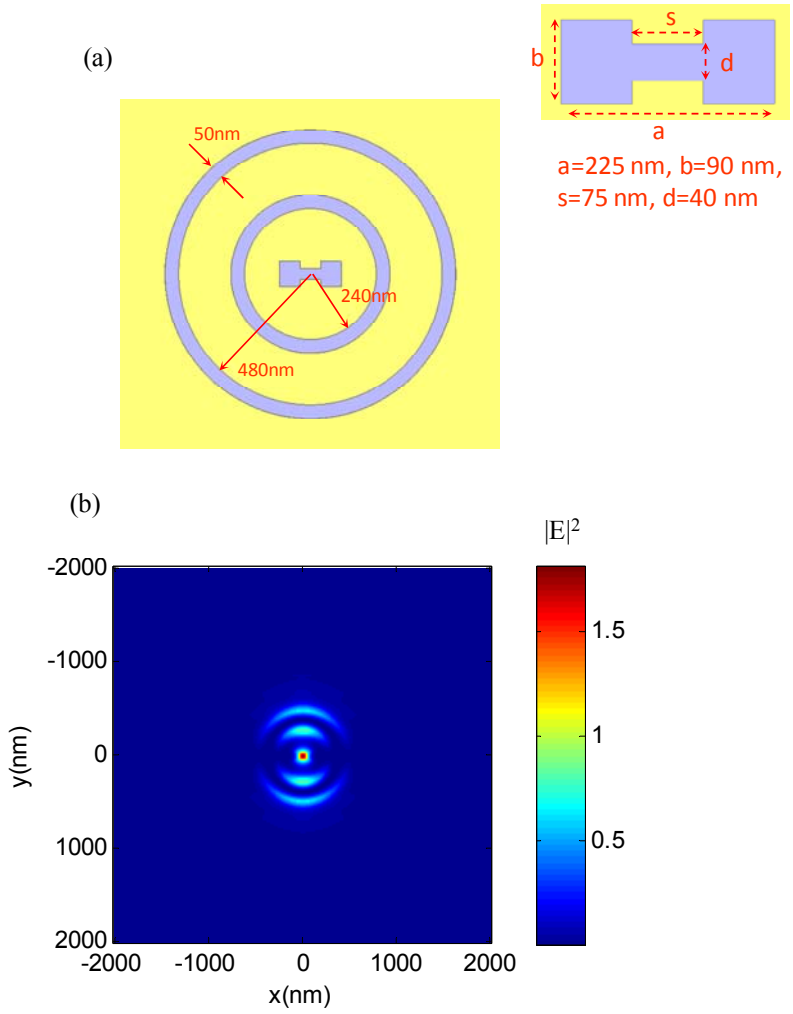

Figure 2.4: Typical H-shaped PLs. (a) The structure of one PL: H-aperture surrounded by two rings. The inset shows the parameters of the H-aperture. (b) *E* field intensity distribution at the plane 25 nm away from the PL.

As shown in Figure 2.5, by replacing the through rings with shallow grooves to reduce the peak intensity of the half-circular patterns to sub 0.1, this contrast ratio can be greatly enhanced to the order of 20 which is good enough for most lithography applications using linear resists.

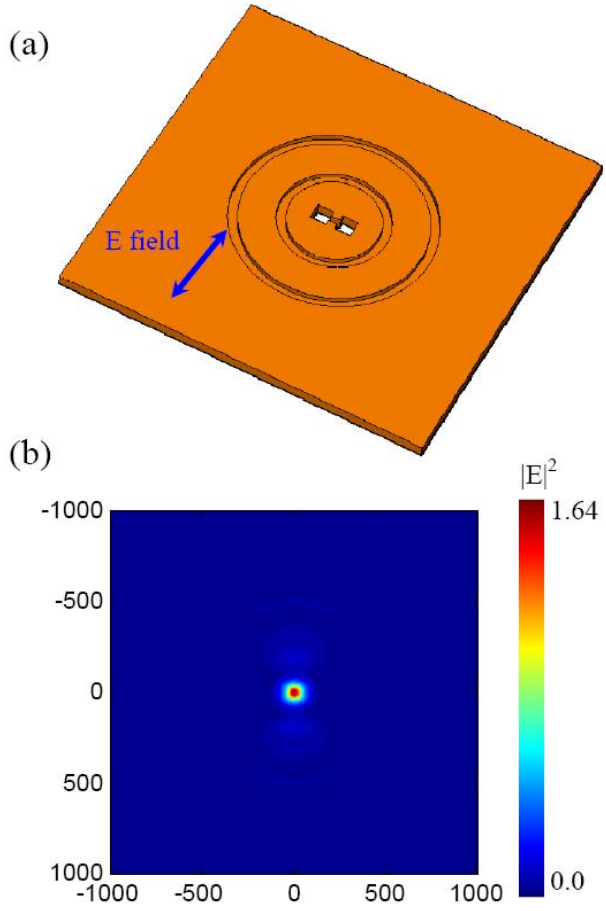

Figure 2.5: (a) An H-shaped aperture surrounded by two rings partially through the Cr slab. (b) E field intensity distribution at the plane 25 nm away from the PL surface.

2.3.3 H-shaped PL with a Ring Reflector

The performance of the PL can be further improved by adding a third ring with a radius of 600 nm (see Figure 2.6). The third ring, placed at a half-period position of the circular grating, acts as a reflector for the outward propagating surface plasmon waves on the Cr film due to destructive interference. Consequently, more light can be concentrated at the focus spot of the PL to generate stronger peak intensity. And the ring reflector also helps to reduce the crosstalk within an array of closely-packed PLs in a parallel patterning process. For better illustration, Figure 2.7 compares the pointing vector fields at the planes 25 nm away from the PL with two rings only and the PL with two rings plus the ring reflector. The insets show the enlarged view of the pointing vector fields at regions immediately outside the outer rings of the two PLs. By comparison, it is clear that less energy propagates outwards and more energy is focused at the center of the PL after adding the ring reflector. Figure 2.8 shows the field intensity distribution at the plane 15 nm away from the

improved PL. The peak intensity of the focus spot is 5.28, which is about 29% more than the peak intensity by the PL without the reflector. Additionally, replacing of Cr with other metals that can better support SPPs, such as Al, can further improve the lens energy efficiency.

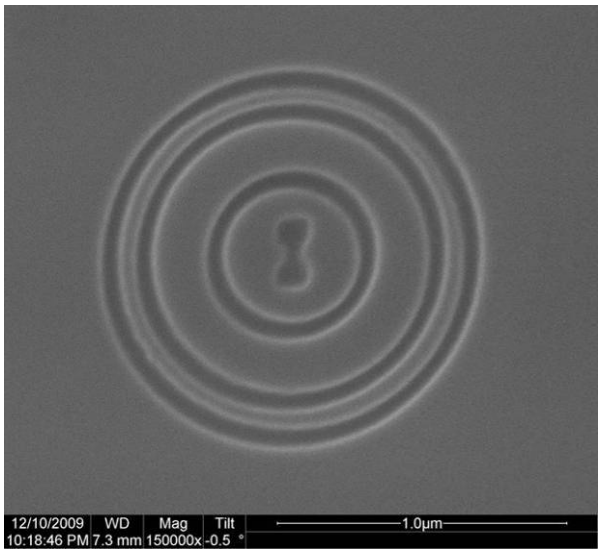

Figure 2.6: SEM pictures of H-shaped PL with a ring reflector.

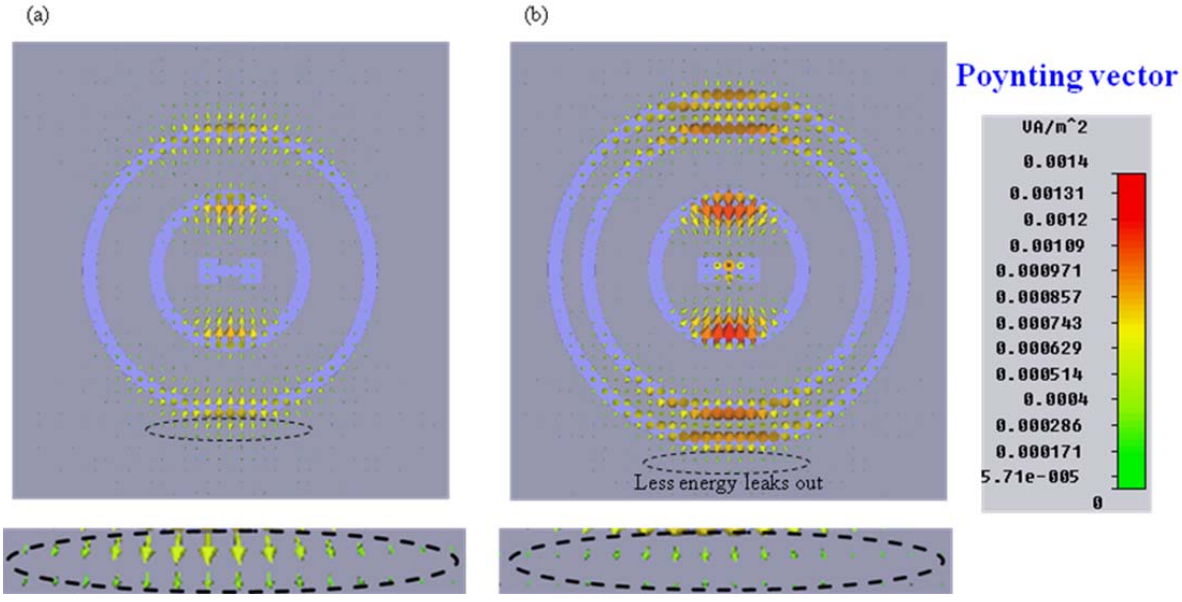

Figure 2.7: Poynting vector fields at the plane 25 nm away from the PLs. (a) The PL with two rings only (b) The PL with two rings and a reflector. The insets are the enlarged views of the pointing vector fields at the regions immediately outside the last ring of the two PLs.

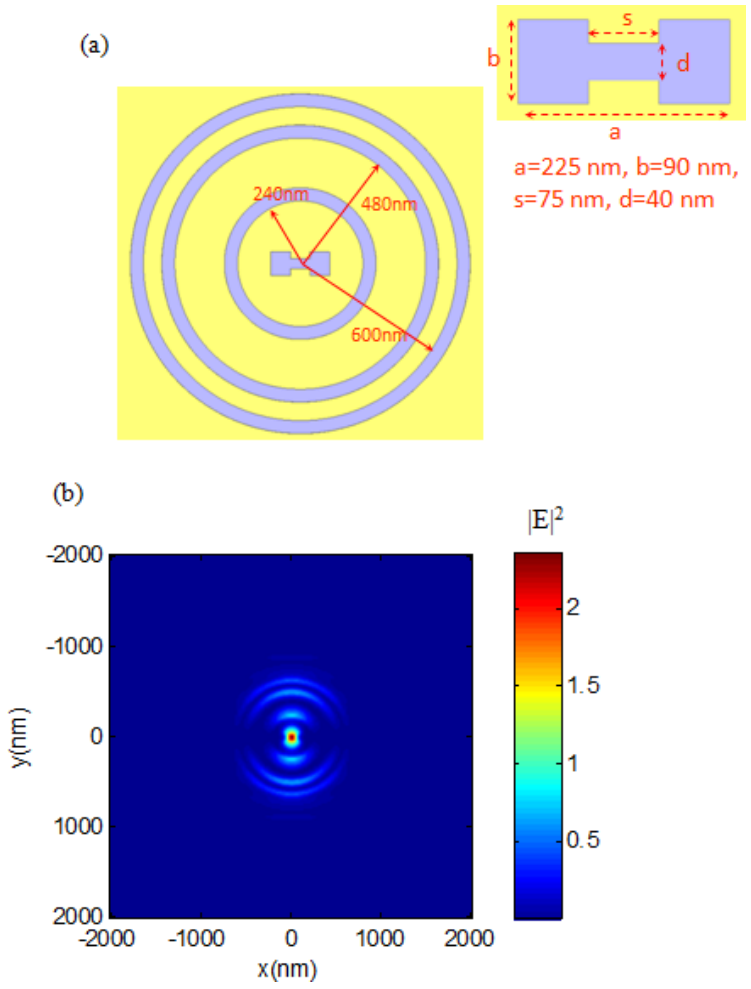

Figure 2.8: An example of H-shaped PL. (a) The structure of an improved PL design: H-aperture surrounded by two rings and a reflector ring. (b) E field intensity distribution at the plane 25 nm away from the PL.

Comparing the lens performance between the H-shaped and the optimized modified bull's eye, at the focus spot size of 75 nm defined by the FWHM intensity, we find that the optical intensity enhancement factor itself is already one order higher for the H-shaped PL. When we also consider the size differences between them (where the H-shaped PL is about 1 μm and the modified bull's eye is about 4 μm in diameter) for the same amount of laser total power input, the transmission efficiency through the H-shaped PL is about a few percent (1~2% at 25 nm away from the lens surface) which is two orders higher than that of the modified bull's eye design.

2.3.4 Recessed H-shaped PL for Direct Line Patterning

For most semiconductor applications, it is more desirable to directly print other shapes such as

narrow and short lines rather than isolated dots. There are many practical advantages for non-pixel based patterning in many applications. Importantly, it can help to improve the line-edge roughness which is critical for the device performance. And it also helps to improve the maskless lithography throughput by patterning a larger area in the same amount of time and power consumption. A single plasmonic lithography head can carry thousands of PLs. A combination of different types of lenses could greatly improve both the patterning quality and throughput.

One simple example is the recessed H-shaped PL which is capable of patterning short lines instead of connected dots. This is achieved by replacing the center H-shaped aperture with modified partially recessed cross elements. The modified H-shaped aperture is shown in Figure 2.9. In this design, the gap between the two ridges is enlarged to 80 nm which causes the original center spot to split into two rectangular short lines aligned to the edges of each ridge. And then one of the lines is attenuated by introducing a 15 nm recess to the associated ridge. As shown in Figure 2.9, a non-symmetric E-field is generated 15 nm away from the PL. And the focus spot size is about 20nm by 60nm with a contrast ratio of 2. Figure 2.10 shows an SEM picture of a fabricated recessed H-shaped PL.

(a)

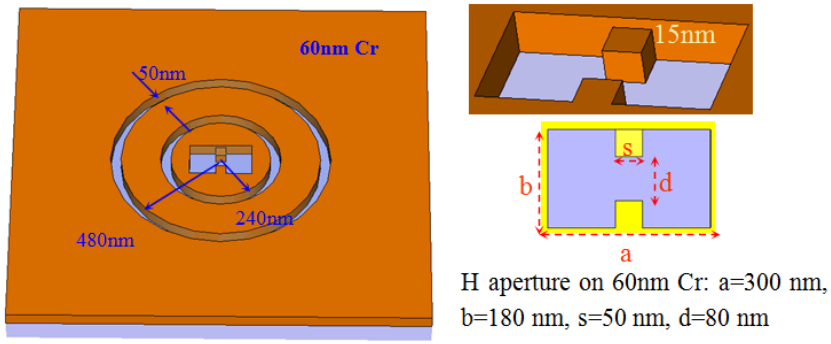

H aperture on 60nm Cr: a=300 nm, b=180 nm, s=50 nm, d=80 nm

(b)

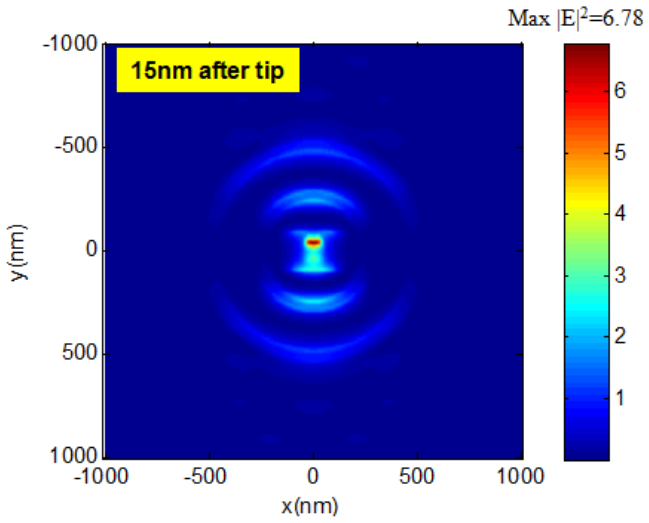

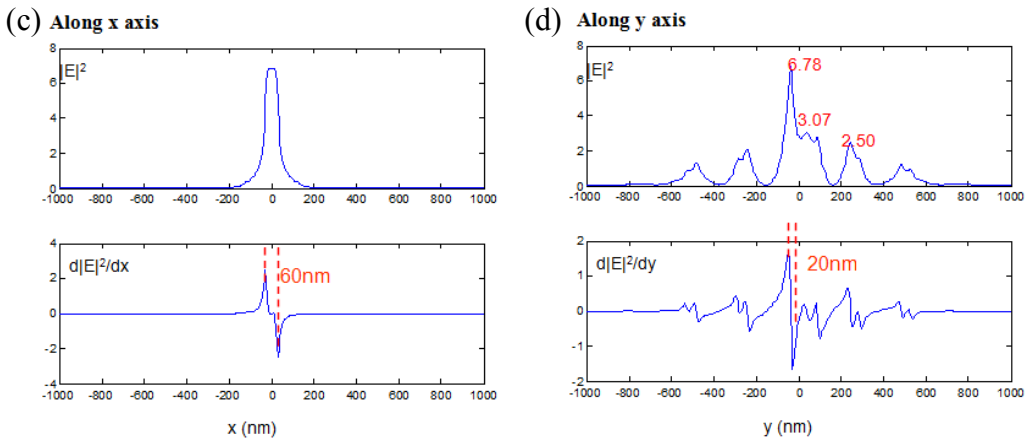

Figure 2.9: Recessed H-shaped PL design and performance. (a) Lens dimensions. (b) Light intensity profile at 15 nm distance from the PL. (c) and (d) Cross-section profiles.

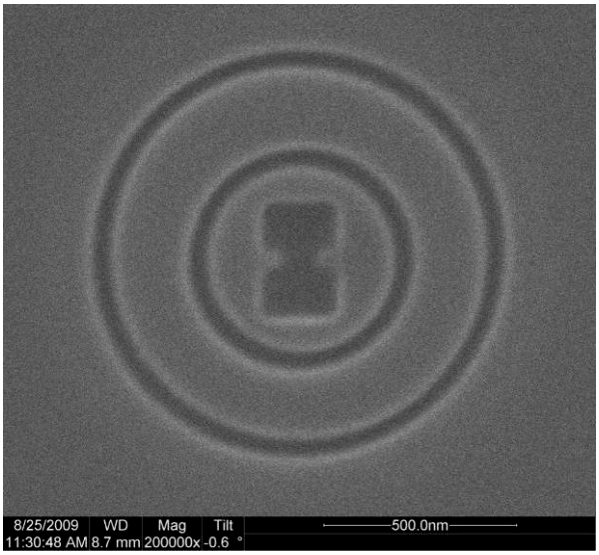

Figure 2.10: SEM picture of recessed H-shaped PL.

Similarly, PLs with more complicated focus spot shapes can be designed by using different aperture shapes and introducing local pattern recesses. This approach provides more freedom to the PNL process.

2.3.5 Push-Pin PL

One of the limitations of both the aperture- and antenna- based PL designs is the trade-off between their resolution and coupling efficiency. For SPP apertures or antennas, the strong SPP

resonance is tightly confined inside their nanoscale gap. And this highly confined subdiffractive field decays exponentially at a distance away from the metal surface. A smaller light spot decays over a shorter distance leading to a lower coupling efficiency. In order to improve both the lens resolution and coupling efficiency, a novel type of PL, called the push-pin design, is proposed to pattern sub 20 nm features. This push-pin design is optimized for the case when a metallic based resist layer is used but it also performs reasonably well for dielectric resist layers.

A push-pin PL has a half antenna pin structure surrounded by a set of SPP grating couplers. The SPP grating couplers are used to collect the SPP's energy towards the center of the structure. And a pin structure is placed at the center of the lens serving as an antenna pole. Figure 2.11 shows two typical designs with different types of grating couplers. The first one uses a spiral shape slit working with circular polarized plane wave. And the second design uses two sets of half rings on both sides of the pin with a plane wave linearly polarized along the symmetry axis of the lens. Because these two designs share the same idea and have similar performances, we will mostly use the second design as an example in the following discussions.

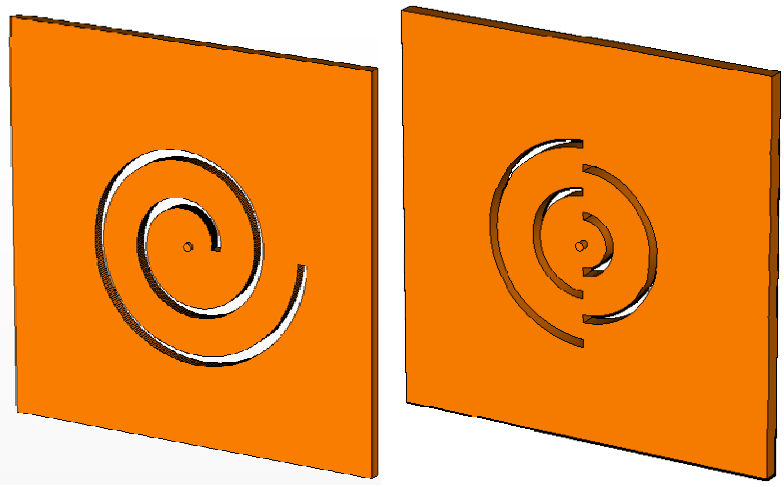

Figure 2.11: Two typical push-pin designs with different types of grating couplers.

Judging from the geometry itself, the gratings of the push-pin designs seem to form a destructive interference instead of constructive interferences as in the case of the circular gratings in the previous bull's eye and H-shaped designs. Although it seems to be contradictory to the previous approaches, this new design is better able to couple the SPP's oscillations in the presence of a metallic layer at its proximity. Most of the previous designs have the capability of focusing the SPP's energy to a nanoscale spot, but in the presence of a metallic resists/recording layer, their performance is usually impaired due to the interactions between the lens and the metallic layer. Figure 2.12 shows a comparison between cases with and without the presence of a metallic layer. As seen from the figure, when a metallic surface is placed at the proximity of the SPP's gratings, the e-field profile becomes concentrated with 25 times enhancement at the center of the structures

instead of being suppressed as before. This difference is caused by the SPP's interaction between two opposite metal surfaces which corresponds to the off-plane component of the e-field. It can be understood by considering the mirror charges inside the metallic resist/recording layer.

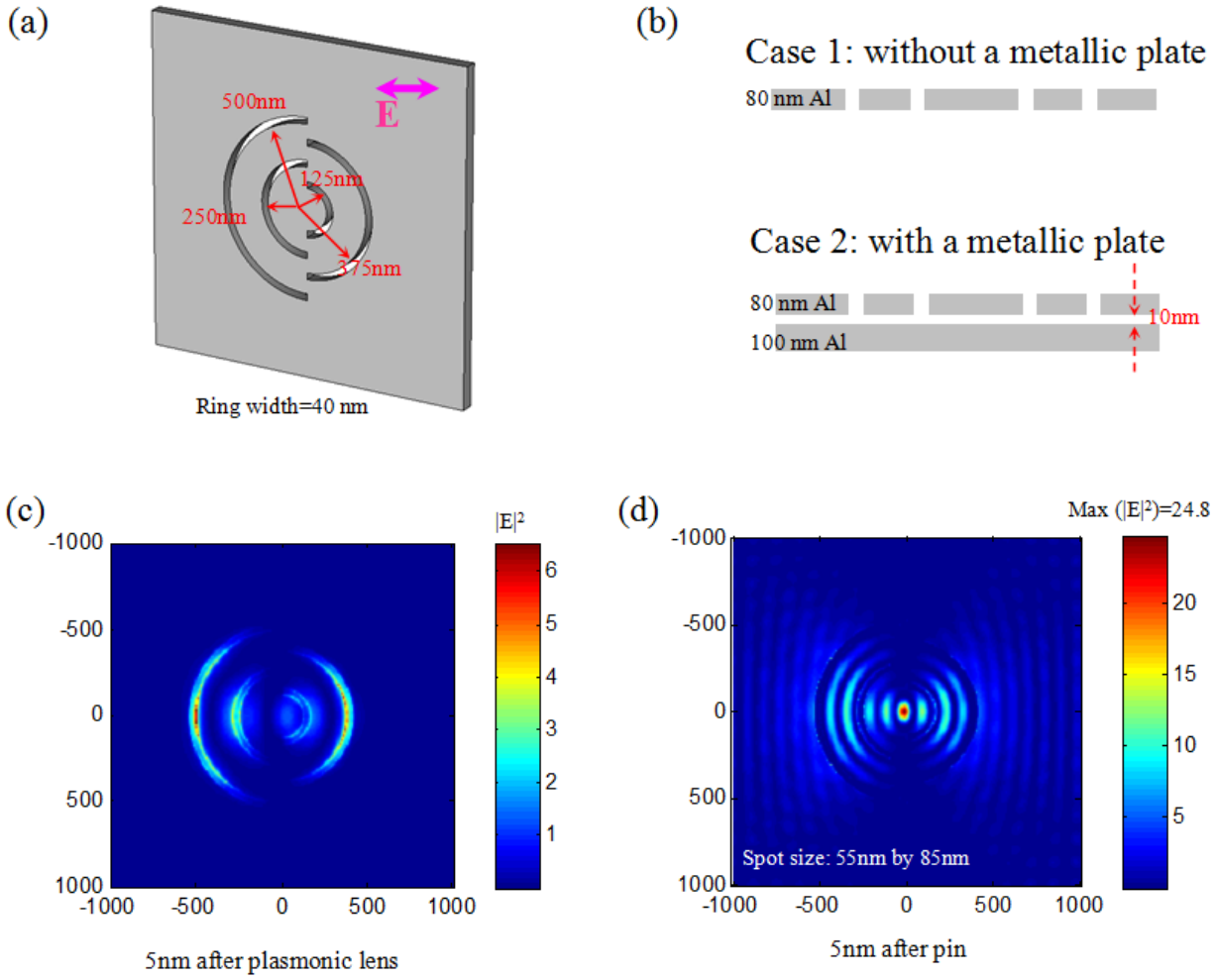

Figure 2.12: A comparison between cases with and without the presence of a metallic layer. (a) Dimensions of lens design. (b) Cross-section view. (c) Simulation result for case 1. (d) Simulation result for case 2.

In push-pin PL designs, the pin structure is placed at the center to further localize the SPPs utilizing both the lightning pole effect and antenna dipole interaction. Figure 2.13 shows an example design using gold for the wavelength of 633 nm. An enhancement of about 2000 times is achieved at the distance of 5 nm away from the pin. At a distance of 10 nm where the second gold surface is located, the enhancement factor is about 800 times. The transmission efficiency (η_L) is more than 80% which is significantly higher than for other designs at the same resolution and

working distance.

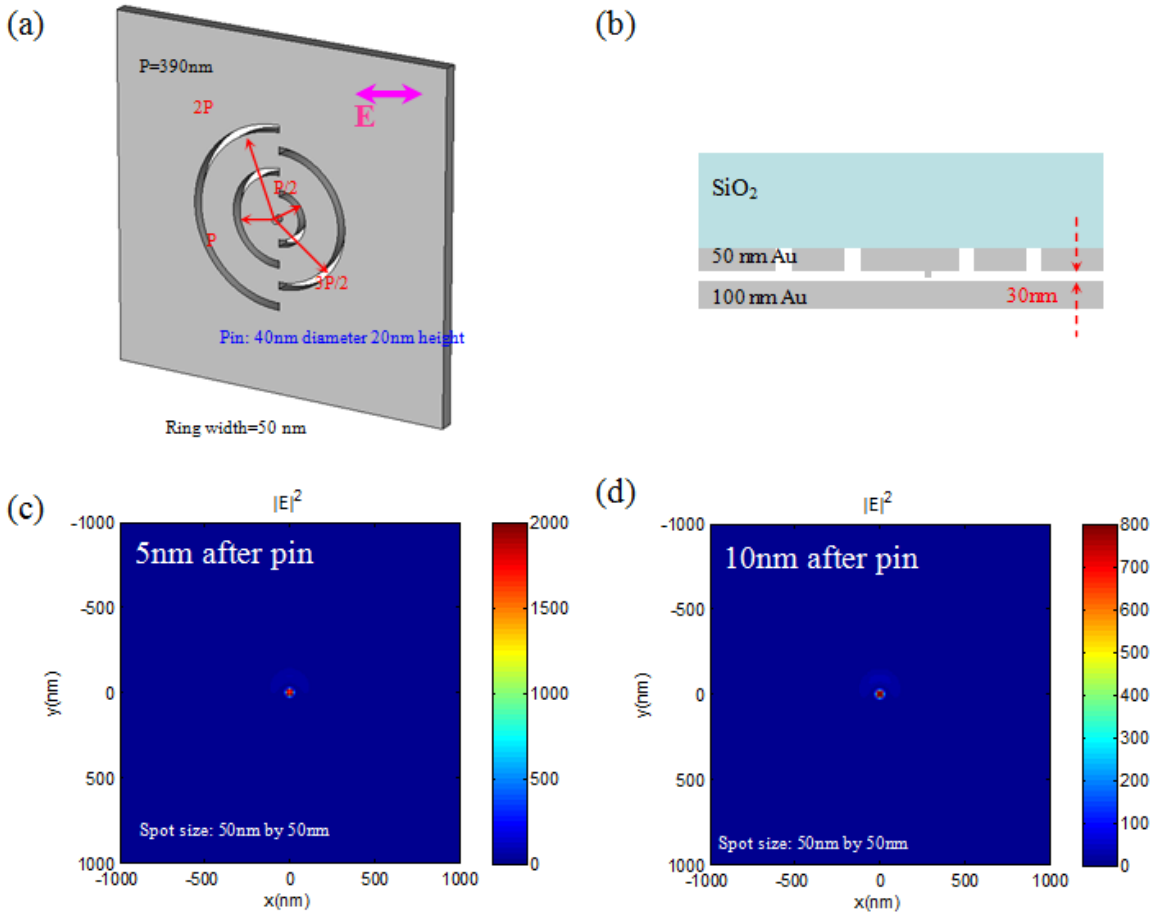

Figure 2.13: An example of push-pin design using gold for the wavelength of 633 nm. (a) The dimensions of the PL design. (b) The base surface of the PL is placed 30 nm away from the other gold surface which leaves a clearance of 10 nm at the position of the pin. (c) An enhancement of 2000 times is achieved at the distance of 5 nm away from the pin. (d) At a distance of 10 nm where the second gold surface is, the enhancement factor is about 800 times.

For the push-pin design, the size of the focus spot can be easily tuned by simply changing the dimensions of the pin structure. Figure 2.14 shows an example design for a 25 nm spot size using aluminum with a 365 nm wavelength and a 10 nm working distance.

Under proper working conditions, the push-pin design is capable of focusing light to 10 nm and below. Figure 2.15 shows an example design using aluminum with 365 nm illumination. A 10 nm light spot is obtained at a distance of 5 nm with 100 times enhancement and 20+ times contrast. In this configuration, the transmission efficiency (η_L) is about 1% due to the ultra small focus spot size, but both the spatial confinement and light enhancement can be greatly improved by using a smaller working gap.

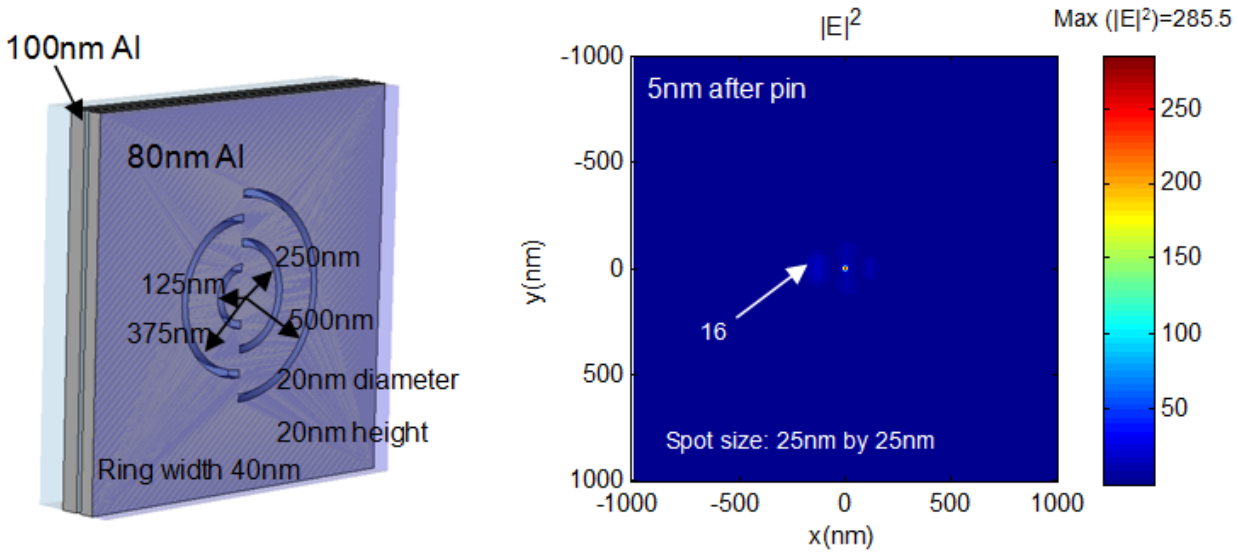

Figure 2.14: An example push-pin design for 25 nm spot size using aluminum at 365 nm wavelength and 10 nm working distance.

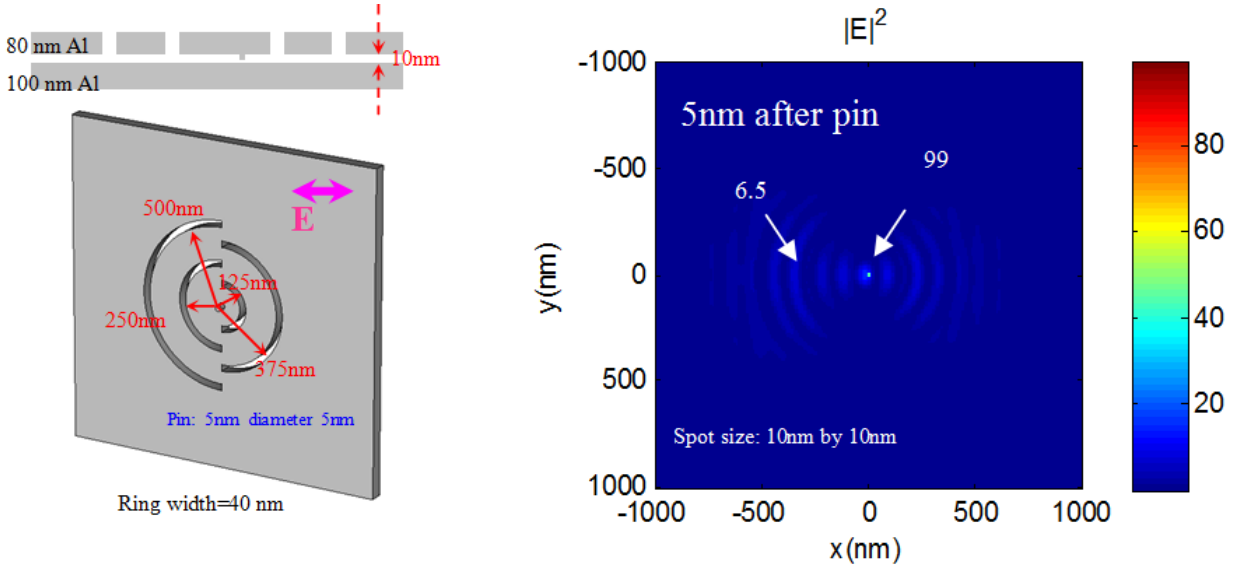

Figure 2.15: An example push-pin design using aluminum with 365 nm illumination achieving a 10 nm light spot at a distance of 5 nm with 100 times enhancement and 20+ times contrast.

Figure 2.16 shows a gold push-pin PL structure fabricated using standard micro-fabrication techniques. The center pin has a diameter of 40 nm and a height of 30 nm. In order to examine the performance of this push-pin design, the fabricated lens is studied using aperture-less NSOM. In

the experiment, the lens is illuminated from the backside at the wavelength of 633 nm with proper polarization. As shown in the figure, the evanescent component of the optical field is indeed concentrated at the pin tip. Because of the non-ideal shape of the NSOM tip, both the mapped topography and the optical field of the pin feature show a triangular shape due to the convolution effect. The mapped optical spot field has a size of 58 nm by 105 nm, but the focus spot radius should be smaller than 50 nm judging from the radius of the spot corner which is consistent with our simulation results. It should be pointed out that the aperture-less NSOM measurement represents only the nonlinear component of the evanescent field interacting with the NSOM tip above the lens top surface. The result cannot directly represent the performance of the structure. Also, a dielectric AFM tip was used in the aperture-less NSOM measurement instead of using a metallic tip which could greatly enhance the structure response. Therefore, a direct lithography test is expected to give a more convincing result.

The performance of the push-pin design was also studied using Cr as the lens material. This is appropriate for high speed scanning for reliability considerations. Because Cr doesn't support SPPs as well as some metals like Al or Au, the field enhancement is much lower compared with previously studied cases, but it still performs much better than the bull's eye and H-shaped designs. Figure 2.17 shows two Cr-based designs with 50 nm spot sizes. It shows an enhancement factor of 35 at a distance of 10 nm. An important parameter of a PL is its depth of focus (*DOF*). The push-pin design has extraordinary performance with a large DOF. As shown in the figure, when the gap is increased from 5 nm to 10 nm, both spot sizes and light intensities remain almost unchanged. This long working distance helps to produce patterns with better definition and uniformity. Similar characteristics were observed after reducing the focus spot size to 25 nm.

In the absence of the metallic resist/recording layer, the energy confinement of the push-pin PL still exists, but it has a smaller enhancement factor. The simulations shown in Figure 2.18 show that the enhancement for Al and Cr based designs drop to about 11 and 3, respectively. Due to the absence of mirror charges, the spot shape is also slightly affected by the surrounding gratings and polarization of the incident light. But in comparison to the PL designs with similar spot size, the push-pin structure has the advantages of both higher enhancement and longer working distance.

Figure 2.19 shows the SEM pictures of the fabricated structure using Cr. Effort is ongoing to implement the push-pin designs in both lithography and imaging applications.

Another potentially important application for the push-pin PL is in the field of nanoscale imaging. The protrusion of the center pin design makes it an excellent scanning probe especially for metallic structures. Figure 2.20 shows a simple example of the imaging process using an Al based push-pin PL to probe a 40-nm Al sphere. As can be seen from the figure, there are some strong dipole interactions when the pin scans over the Al sphere. This effect allows us to detect the changes of scattered far-field light which can be used to reconstruct the nearfield image.

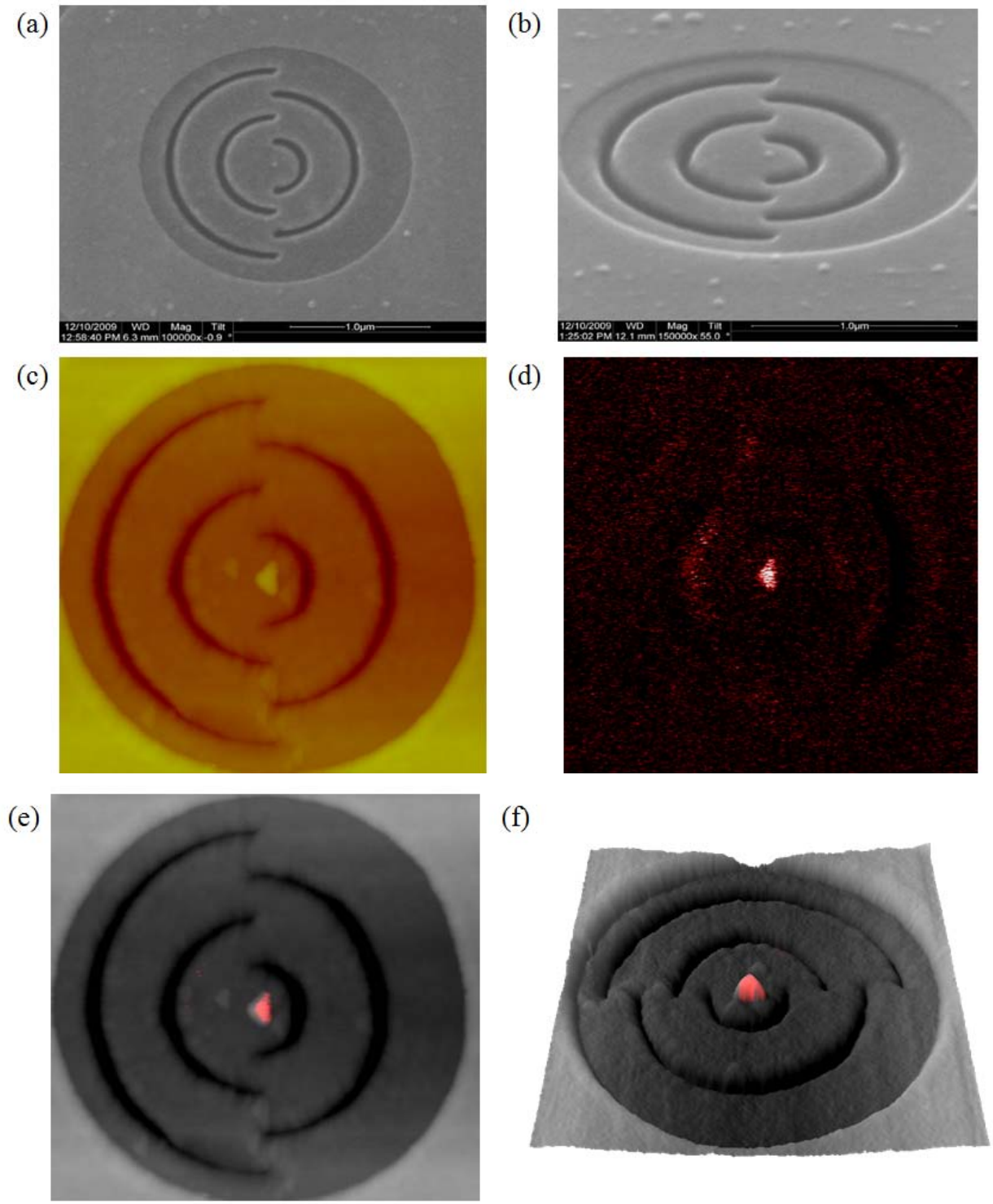

Figure 2.16: Fabricated gold push-pin PL structure fabricated and its nearfield aperture-less NSOM studied. (a) and (b) SEM pictures. (c) AFM measured lens profile. (d) Aperture-less NSOM measurement. (e) and (f) Superposed AFM measurement with aperture-less NSOM measurement.

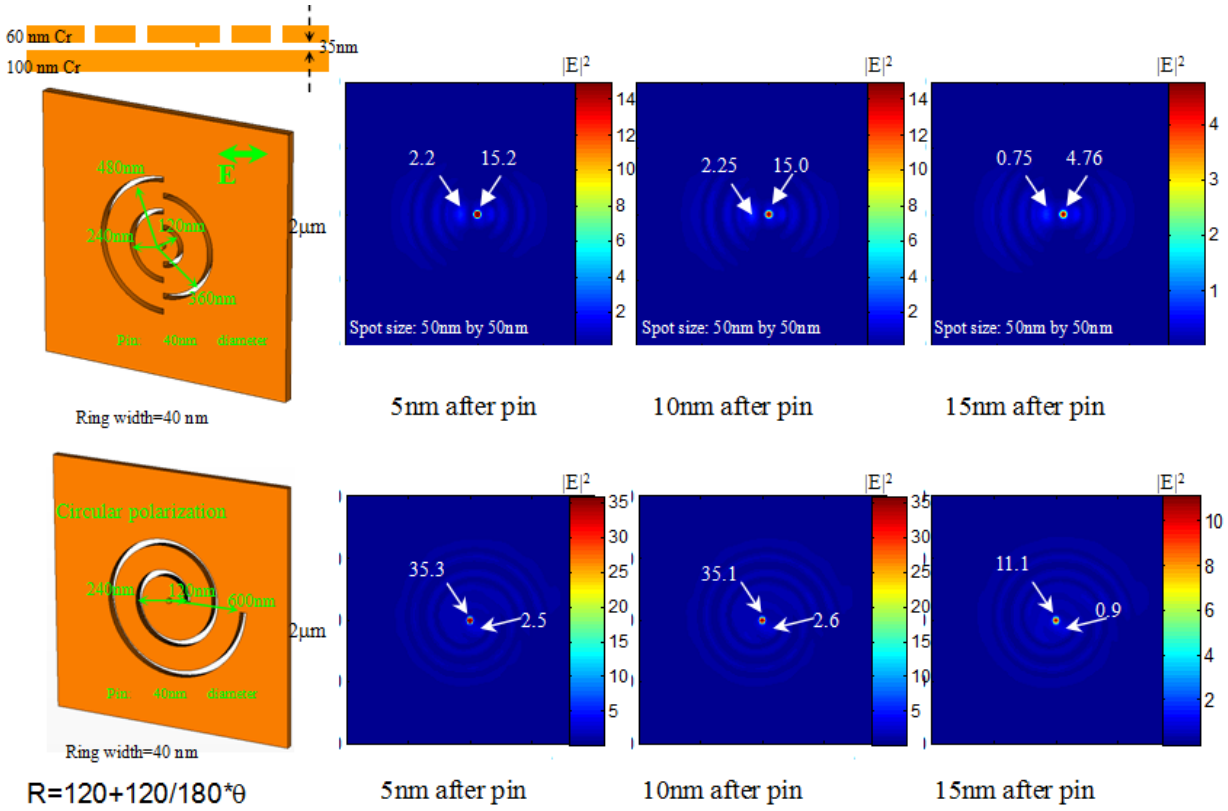

Figure 2.17: Two typical Cr-based push-pin designs with 50 nm spot size with extraordinarily large DOF. When the gap increase from 5 nm to 10 nm, both spot size and light intensity remain almost unchanged.

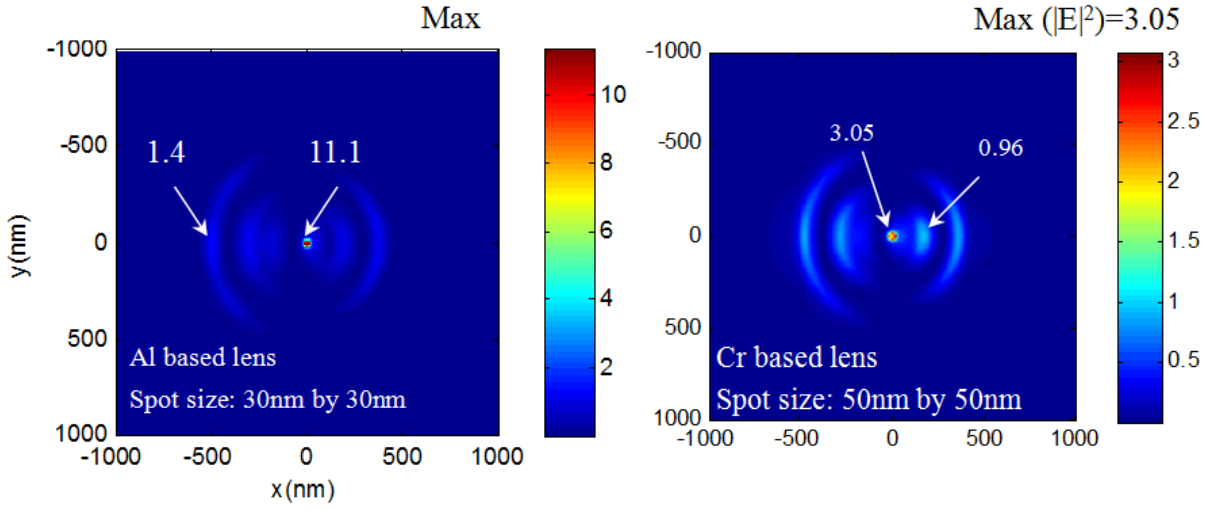

Figure 2.18: The intensity fields for Al (left) and Cr (right) based push-pin lens designs. Due to lack of mirror charges, the spot peak intensities drop to about 11 and 3 respectively and their

shapes are also slightly affected by the surrounded gratings and polarization of the incident light.

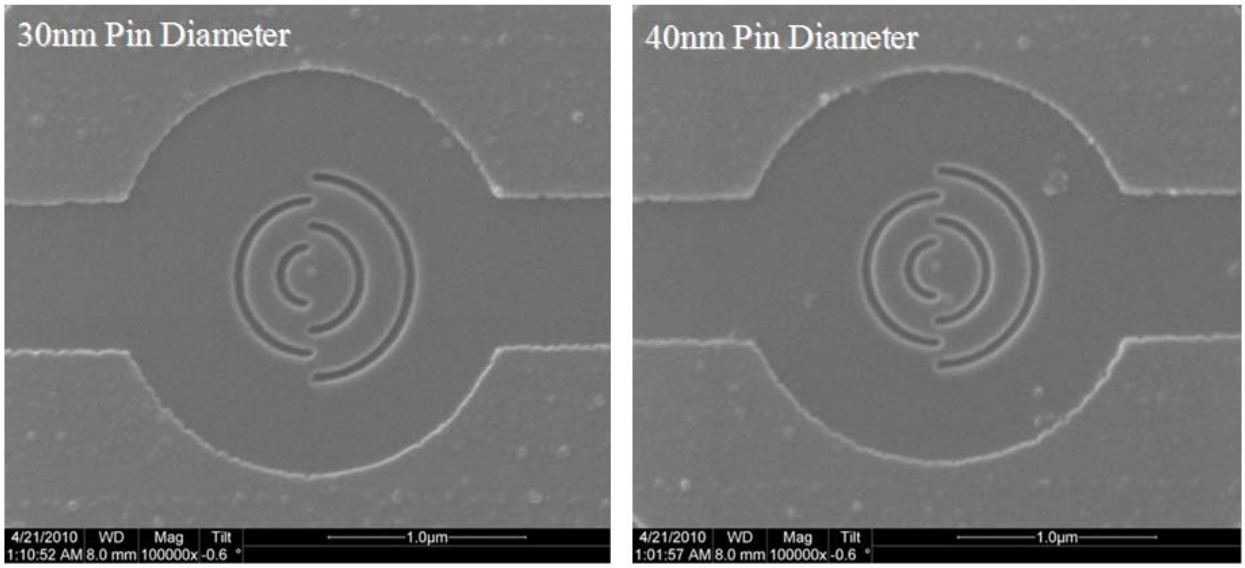

Figure 2.19: SEM pictures of fabricated Cr-based push-pin structures.

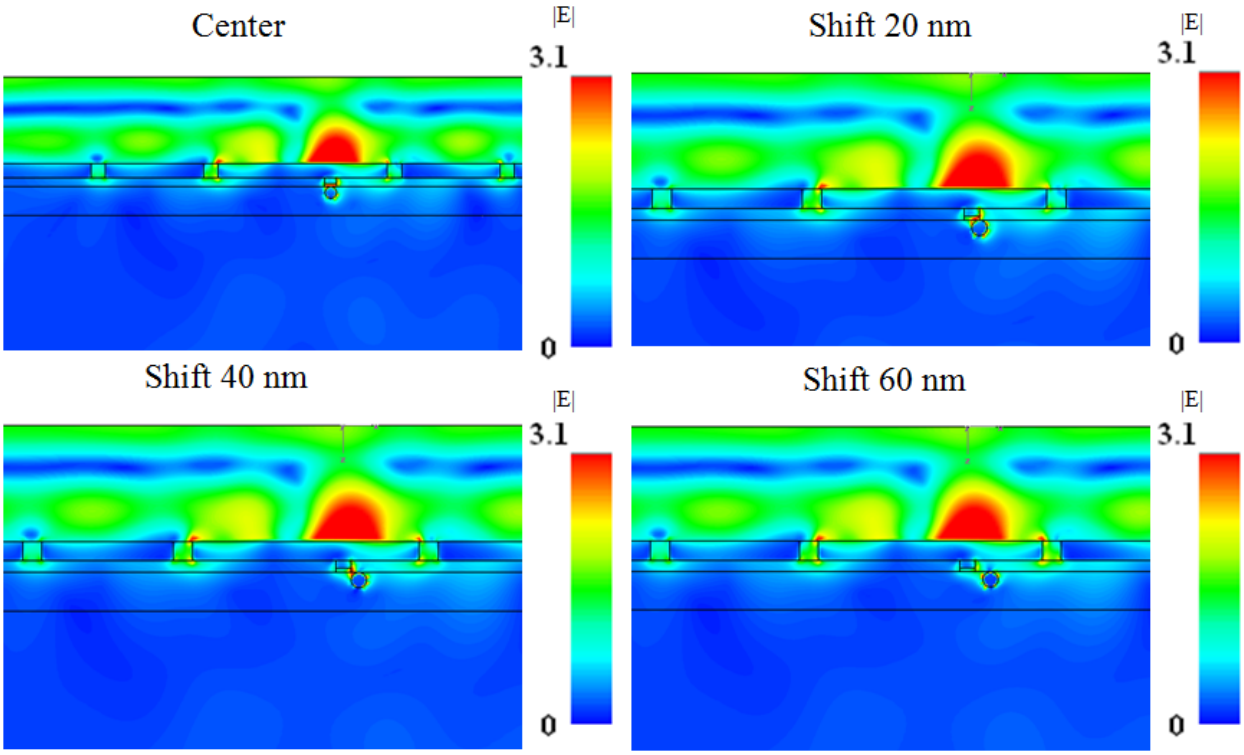

Figure 2.20: A simple example of imaging process using an Al based push-pin PL to probe a 40-nm

Al sphere. Numerical study indicated strong dipole interactions when the pin scans over the Al sphere which can be detected in the far-field to reconstruct the nearfield image.

2.4 Summary

In this chapter we first introduced the commonly used plasmonic resonant structures and their working principles. Then a series of lens parameters was proposed to characterize the performance of the PL for nanolithography purpose. Novel PL designs, including the modified bull's eye, H-shaped, H-shape with a ring reflector, recessed H-shaped and push-pin, were introduced and studied numerically and/or experimentally in order to investigate their performances.

Chapter 3 Plasmonic Flying Head

3.1 Flying Head In Hard Disk Drives

The compressible Reynolds lubrication equation is the governing equation of gas lubrication. Since only a few simple cases have analytical solutions of this equation due to the complexity of Reynolds equation, as well as the complex geometry required for the air bearing surfaces (ABS) numerical methods are needed in order to study other general configurations. Simulation tools have been developed in the Computer Mechanics Laboratory (CML) at UC Berkeley over the past 25 years [101-107] to study the gas lubrication in the head disk interface (HDI). The main solver is based on a control volume formulation of the linearized Reynolds equation.

In HDD applications, it is desirable to maintain the head-media spacing (HMS) as a constant value at different radial positions considering both the skew angle and relative disk linear velocity change according to the radial position. A successful ABS design needs to meet many requirements such as flying height (FH) uniformity, track seeking performance, fabrication tolerance, and contamination tolerance. For example , a stable and constant clearance must also be sustained in the presence of allowable altitude and temperature changes, and possible head to disk contacts must be avoided during load/unload processes and moderate strength operational shocks. To achieve the higher areal densities called for in the HDD roadmap in hard disk drives (HDD), the minimum physical spacing or FH between the read/write element and the rotating disk must be gradually reduced to sub 2 nm by both improving the ABS designs and introducing thermal flying-height controlled (TFC) to the head-disk interface (HDI). In order to achieve the close spacings and fast scanning speed, the PNL adopted the idea of using the gas lubrication approach for the scanning gap control. But because of the different emphasis in the PNL application, the requirements are somewhat different from those of HDD applications.

In this chapter we present some novel plasmonic flying head designs based on the HDD ABS technology. The proposed plasmonic flying head designs possess high bearing stiffness, damping and good fabrication and contamination tolerances. Numerical and experimental studies of the static and dynamic ABS performances, including flying attitude and load/unload performance, are carried out and discussed.

3.2 Plasmonic Lithography Head Design and Fabrication

To achieve high-speed scanning while maintaining the nanoscale gap, we designed a unique air-bearing slider to fly the PL arrays at a constant height above the disk surface at speeds of 4-12 meter/second. The rotation of the disk substrate creates an air flow along the ABS surface of the

slider of the plasmonic flying head which generates an aerodynamic lift force, which is balanced with the force supplied by the suspension arm to precisely regulate the desired nanoscale gap between the PL arrays and the rotating substrate. With the high bearing stiffness and small actuation mass, this self-adaptive method can provide up to 120 kHz effective bandwidth. The usage of such an ABS eliminates the need for a feedback control loop, and therefore it overcomes the major technical barrier for high speed scanning while precisely maintaining the nanoscale gap between the flying PL arrays and disk surface.

As shown in Figure 3.1, the high-throughput nanolithography is accomplished by using the plasmonic flying head at a relatively high speed (~10 m/s). The plasmonic flying head is made of a specially designed transparent air bearing slider with arrays of PLs fabricated on the ABS surface. Employing large arrays of PLs enables parallel writing for high throughput.

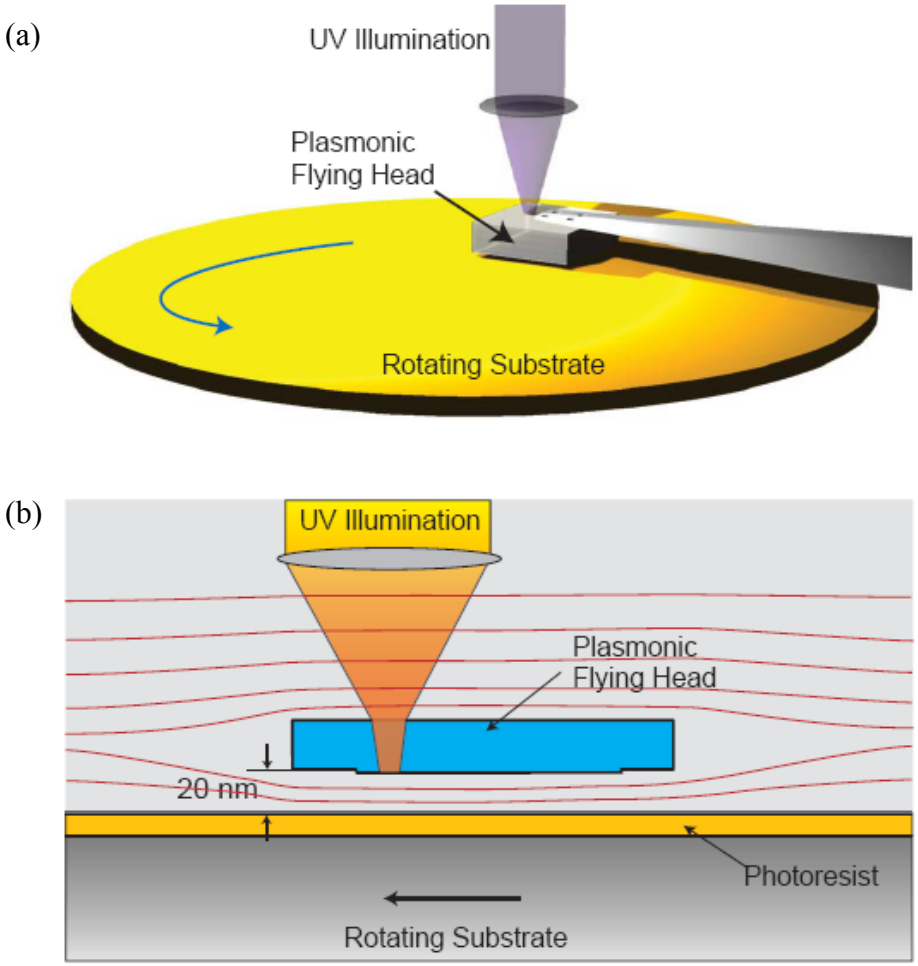

Figure 3.1: High-throughput maskless nanolithography using PL arrays. (a) Schematic showing the lens array focusing ultraviolet (365 nm) laser pulses onto the rotating substrate to concentrate surface plasmons into sub-100 nm spots. However, sub-100 nm spots are only produced in the near field of the lens, so a process control system is needed to maintain the gap between the lens and the

substrate at 20 nm. (b) Cross-section schematic of the plasmonic head flying 20 nm above the rotating substrate which is covered with photoresist.

In order to keep all the PLs within their working distance, the parallelism between the PL array and substrate needs to be carefully considered in designing the ABS. The ABS for the plasmonic flying head was designed using an in-house developed air bearing simulator, CMLair [101-107].

In order to utilize the modified bull's eye design in the lithography process, the goal of the first generation plasmonic flying head is to achieve a consistent working distance of 20 nm at scanning speeds from 4 to 12 m/s considering the fact that the disk linear velocity reduces as the head goes from the outer to inner radius. Different from the ABS design for HDD application, the skew angle in PNL process is kept at zero in order to reduce the complexities of pattern generation, light delivery and precision position control. In HDD ABS designs, a consistent FH at different disk radial positions is usually obtain by using the change of skew angle to compensate the change of linear relative disk-to-head velocity. The requirement of zero skew in PNL process leads to another practical challenge.

Figure 3.2 shows the air bearing surface design and a simulated air bearing pressure profile with streamlines. The ABS design consists of a four-pad U-shaped dual-rail slider with a long front bar. Two large rear pads generate the repelling peak pressure to float the flying head and prevent possible physical contacts. The two front pads produce the steering repelling pressure to increase the roll bearing stiffness and minimize the roll angle. Sub-2 μrad roll angle is achieved across the disk by adjusting the detailed shape and depth of the rail and pads. The pitch angle is designed to be around 80 μrad to compensate for the curvature variations of both the slider and disk. By throttling injecting air from the leading edge, the long-bar design can significantly reduce the slider's pitch angle, contamination sensitivities and also enhance the slider's damping. The U-shaped dual-rail design efficiently increases the overall sub-ambient ("negative") pressure which improves both the slider's stability and bearing stiffness. As the disk velocity decreases, both the positive pressure and negative pressure decrease, which results in a lower FH and bearing stiffness. The effective air bearing stiffness and damping ratio are about 2×10^5 N/m and 0.1 respectively. The design provides about 85 kHz bandwidth for gap control. The control band width is defined as the frequency above which the ABS cannot attenuate the 1 nm peak-to-peak error motion of the rotating disk by the factor of the exponential constant (e=2.7182).

Figure 3.3(a) shows the variation of minimum head to disk spacing when the slider is loaded onto the spinning disk. During this loading process, no direct head to disk contact takes place. Figure 3.3(b) shows the response of the minimum head to disk spacing when the head is subjected to an external shock. During the shock, the head will deviate from it initial flying altitude and then recover within 0.3 ms.

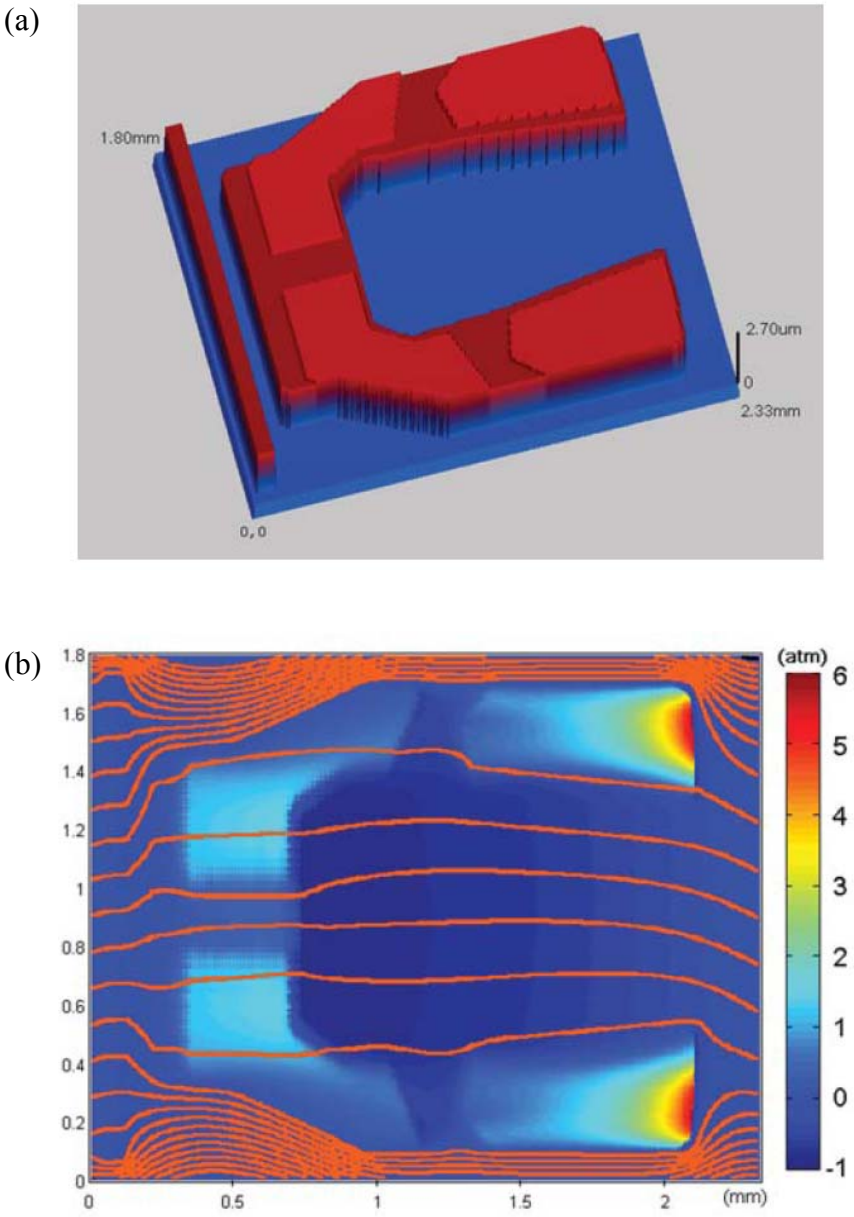

Figure 3.2: Designs and simulations of air-bearing surface (ABS). (a) Oblique view of the ABS. The topography is scaled up by a factor of 200 for better illustration. The ABS generates an aerodynamic lift force and it is balanced with the force supplied by suspension to precisely retain a nanoscale gap between the PL arrays and the rotating substrate. (b) Calculated normal air pressure (colored) and air-mass flow lines (from left to right) under the ABS with a scanning speed of 10 m/s. The pressure is normalized to ambient air pressure. The mass flow lines density is proportional to the mass flow. At the lowest point, the air pressure is maximized but the mass flow is minimized, which favors both air-bearing stiffness and contamination tolerance.

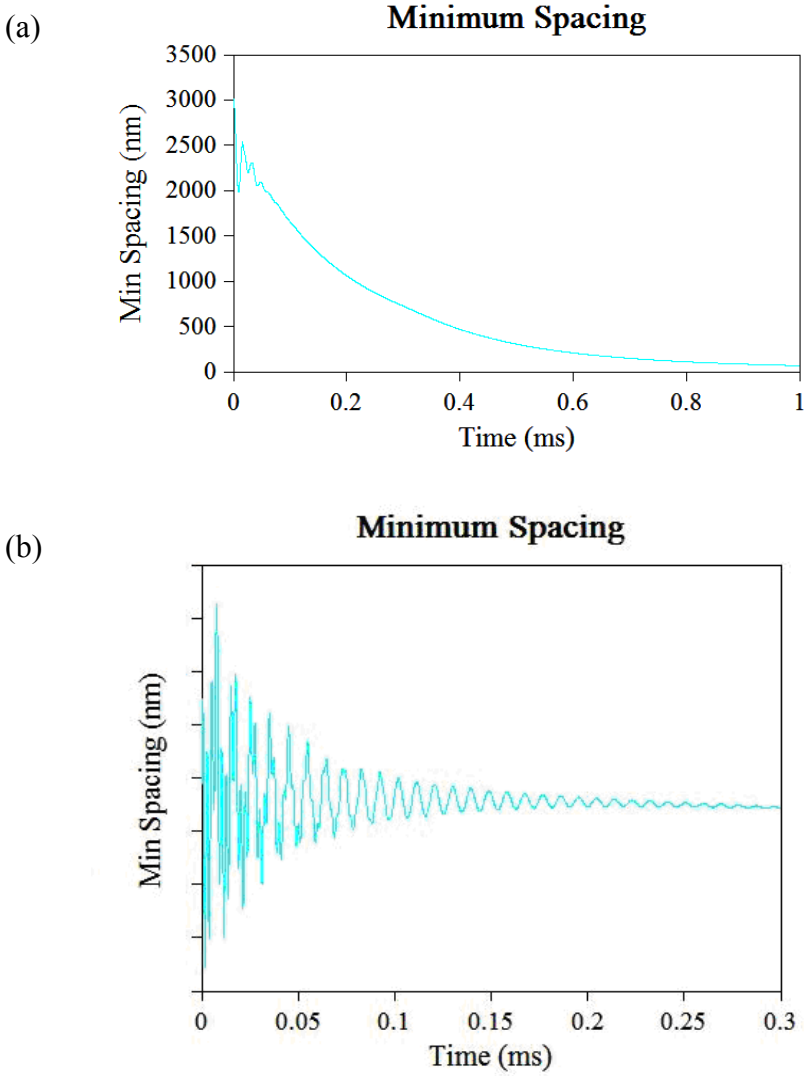

Figure 3.3: Example of dynamic performance of air-bearing surface (ABS). (a) The variation of minimum head to disk spacing when the slider is loaded onto the spinning disk. The head is released at 3 μm height with zero velocity. During this loading process, no direct head to disk contact takes place. (b) The response of the minimum head to disk spacing when the head is subjected to an external shock. During the shock, the head deviates from its initial flying altitude and then recovers within 0.3 ms.

Flying PL arrays at the optical near field is inspired by the magnetic recording head in the HDD. Unlike a conventional HDD ABS [101-107] which uses only the trailing edge mounted transducer to serially read and write the magnetic bits, we designed the plasmonic head to contain a relatively large area filled by an array of PLs that enables parallel writing and high throughput.

Due to the rapid decay of the light intensity of the PL, all PLs need to maintain a distance to the rotating substrate within 30nm which requires the bottom surface of the slider to be parallel to the substrate to within 100 μrad of pitch. This stringent parallelism requirement made the design of

the plasmonic head challenging and different from magnetic head sliders. For example, to fly 1,000 lenses within a 30 nm gap tolerance over the usable area of 800 μm × 20 μm on the rear pads with 4 μm diameter PLs, the ABS needs to be designed with less than 100 μrad pitch angle and 2 μrad roll angle. Also, the ABS needs a larger air bearing stiffness, higher damping ratio and better contamination insensitivity than a conventional HDD ABS. In addition, the plasmonic head must be transparent to light.

In this work, the plasmonic flying heads were fabricated using micro-fabrication techniques and focused ion beam milling, and they were evaluated in a dynamic FH tester (DFHT IV, Phase Metrics). Figure 3.4(a) shows an optical microscope image of the fabricated plasmonic flying head where the sapphire ABS coated with a metal film was assembled to the suspension, and a SEM image of a 2-D array of PLs (4x4) fabricated on the ABS in a square lattice Figure 3.4(b).

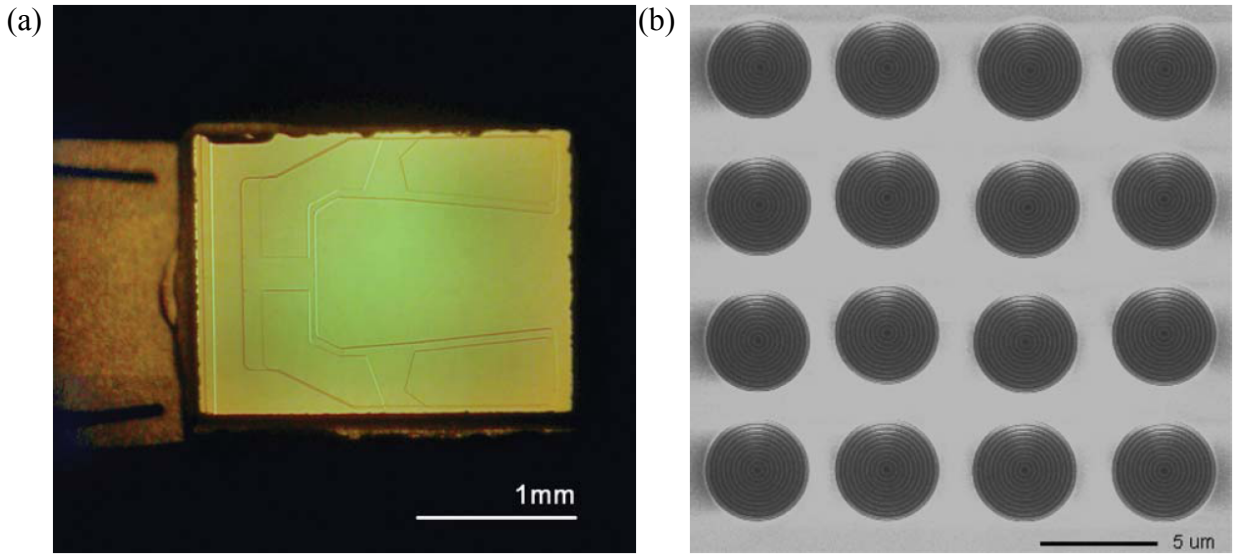

Figure 3.4: Fabricated plasmonic flying head with a modified bull's eye PL array. (a) Optical micrograph of a plasmonic flying head assembled with suspension. (b) Scanning electron microscopy (SEM) image of an array of PLs fabricated on an ABS.

Figure 3.5 shows the FH and pitch and roll angle measurements together with simulation results. We observed that the FH is kept quite uniform over the velocity range 4 to 12 m/s. The measured FH is in good agreement with the simulated ABS design performance where the slight variation from 18.0 nm to 20.4 nm, which is within the tolerance of 30 nm. The measured FH agrees well with the simulated ABS design performance. The parallelism of the ABS is determined by the roll and pitch angles of the ABS with respect to the substrate. When the linear velocity changes from 4 to 12 m/s, the experimentally measured roll and pitch angles vary from 0.15 μrad to -2.34 μrad and 61 μrad to 89 μrad, respectively, in good agreement with simulation design, which ensures the entire 1,000 lens array is within the 30nm gap tolerance.

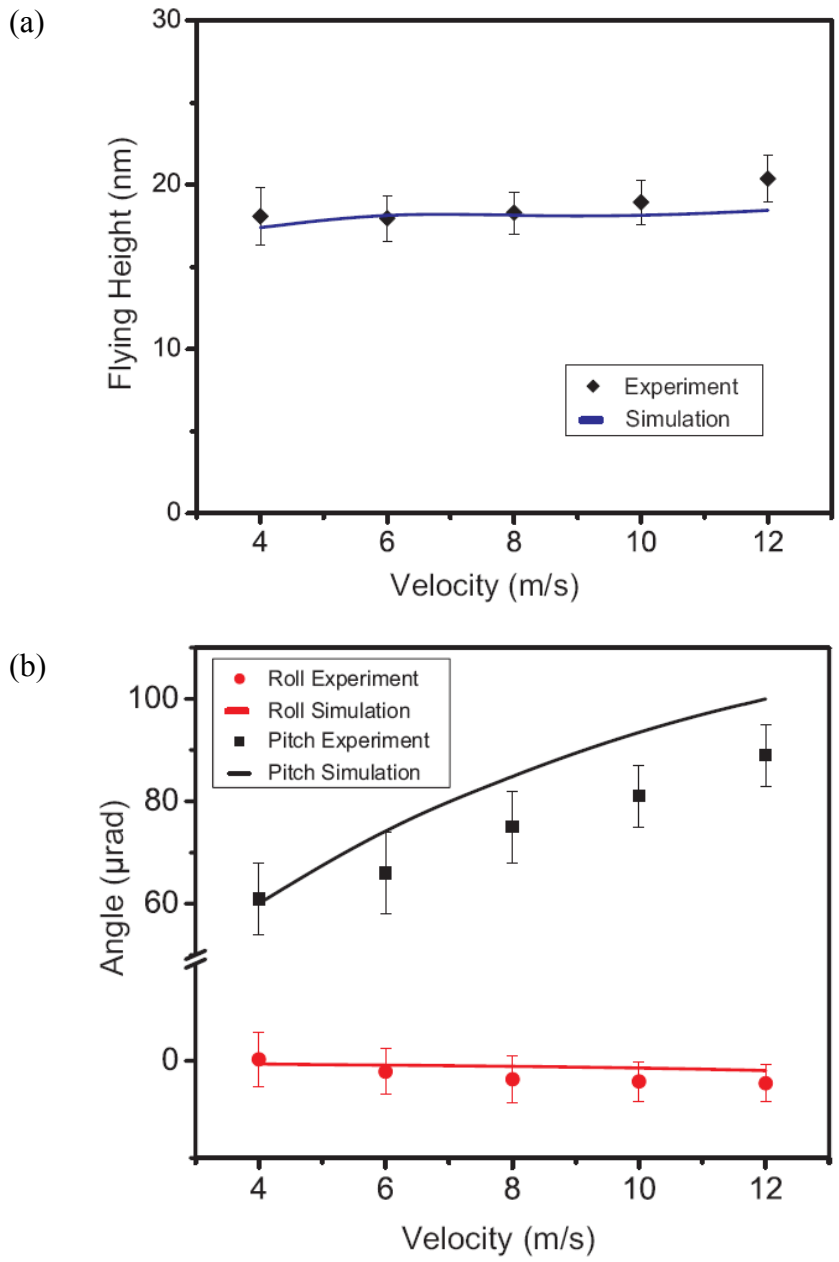

Figure 3.5: FH measurement of fabricated plasmonic flying head. (a) Measured and calculated FH shows the slider maintains the FH at 20 nm, with scanning speeds between 4 and 12 m/s. (b) Measured and simulated pitch and roll angles at scanning speeds between 4 and 12 m/s. Agreement between experiment and simulation demonstrates that the parallelism achieved is within the gap tolerance of 30 nm over the whole area of the PL array and the substrate.

3.3 Improved ABS Design For Sub-10 nm Working Gap

In order to improve the lithography resolution and throughput, the ABS design needs to be

improved to achieve a sub-10 nm working gap with smaller pitch and role variations. The ABS design goal for utilizing the H-shaped PL is to fly the PL at the height of sub-10 nm above the disk surface at speeds of 4-14 meter/second with pitch angle around 40 μrad and sub 1 μrad roll angle.

Based on our previously developed 20 nm FH ABS, the improved design is obtained by varying the etch depths and suspension preloading conditions. Figure 3.6 shows the topography and flying characteristics of the ABS. The designed speed range is from 4 to 14 m/s considering the fact that the disk linear velocity reduces as the head goes from the outer to inner radius. As shown in Figure 3.6(c) and (d), consistent 9±1 nm FHs with sub-1 μrad roll angle and 40-μrad pitch angle are achieved by optimizing the design of the air bearing surface.

Figure 3.6(b) shows the ABS and the simulation result for the normal bearing pressure profile with mass flow lines. Compared with the previous design, this improved design has even higher bearing stiffness, damping ratio and effective control bandwidth. The pitch stiffness is also greatly enhanced, therefore, a more consistent pitch angle can be achieved at different relative dead-to-disk velocities. Due to the high air bearing stiffness and small actuation mass, the flying head can follow the substrate profile and maintain a consistent FH to within sub 1-*nm*.

As shown in Figure 3.7, a plasmonic lithography head is fabricated using micro-fabrication techniques. Figure 3.7(top) inset shows the SEM image of one modified H-shaped PL fabricated by focused ion beam milling on a 60-nm thick chromium (Cr) thin film coated on the ABS. Cr was chosen as the PL material because its superb mechanical properties can prevent lens damage when the structure flies closely above the substrate at high speeds. For this design, the working gap is regulated to be uniform at 10 nm over the velocity range from 4 to 14 m/s with a sub-1 nm variation. The pitch and roll angles of the flying head are maintained at 41±2 μrad and sub-1 μrad, respectively. The effectiveness of the design was verified using a dynamic FH tester (DFHT IV, Phase Metrics). Relying on the consistent pitch angle and small roll angle, up to 16,000 modified H-shaped PLs can be placed on one single head with sub 2 nm working gap variations. Figure 3.7(bottom) shows an SEM image of an array of the modified H-shaped PL.

3.4 Summary

In this chapter, we presented the working principle, structural design, fabrication method and testing results of plasmonic flying heads. The plasmonic flying head is made of a specially designed transparent air bearing slider with arrays of PLs fabricated on its ABS. It can carry large arrays of PLs which enables parallel writing for high throughput. The plasmonic flying head is optimized for high-throughput PNL applications. This technique helps to overcome the major technical barrier for high speed scanning while precisely maintaining the nanoscale gap between the flying PL arrays and disk surface.

(a)

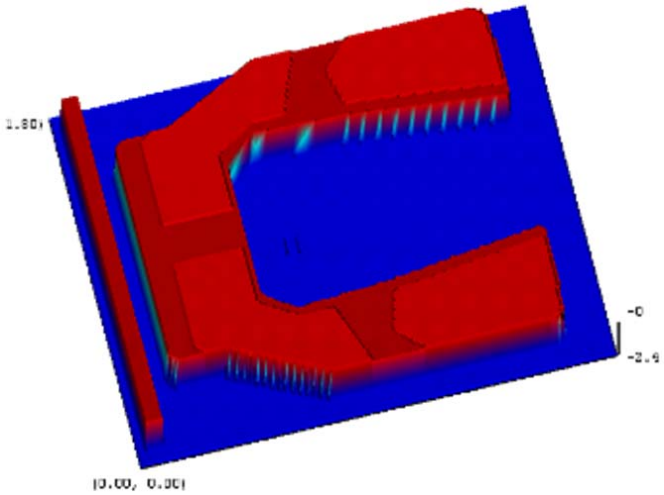

(b)

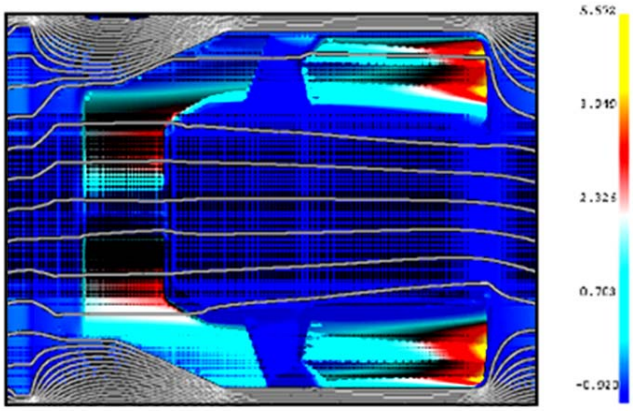

(c)

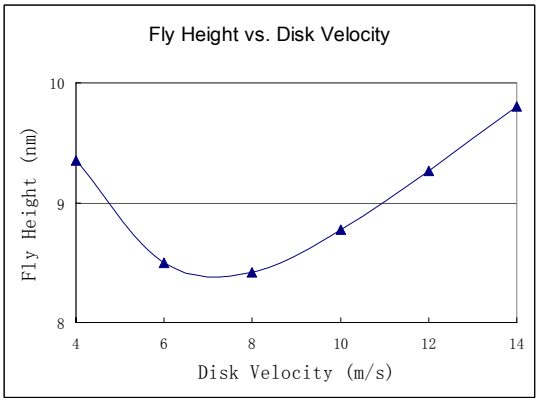

(d)

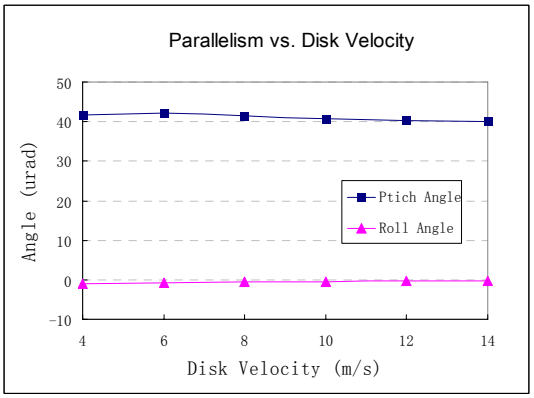

Figure 3.6: (a) New generation ABS with oblique view. The topography is scaled up by 200 times for better illustration. (b) Normal air pressure map under ABS normalized to standard atmosphere pressure. (c) FH of ABS at different disk velocities. (d) ABS parallelism at different disk velocities.

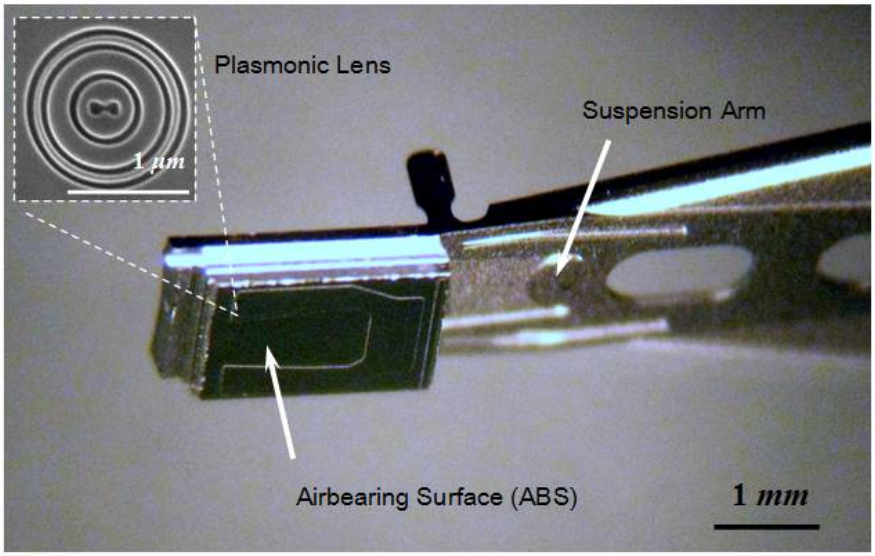

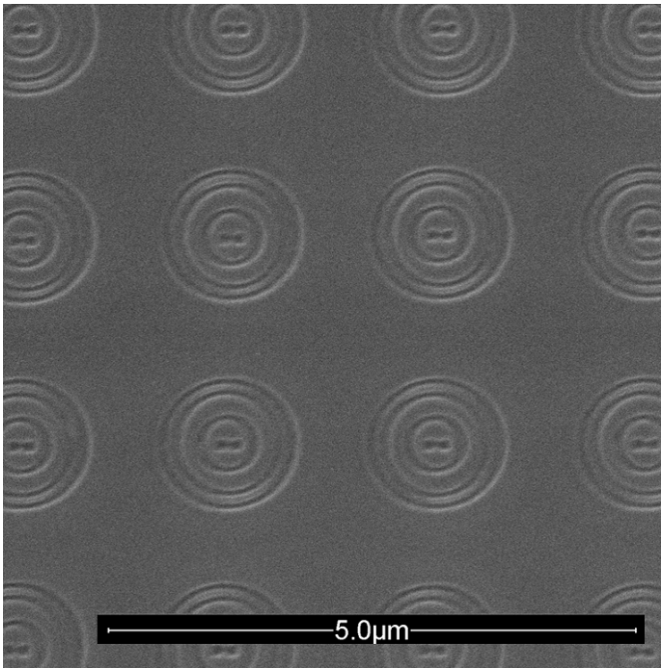

Figure 3.7: A plasmonic lithography head is fabricated using micro-fabrication techniques. (top) A photograph of a fabricated plasmonic flying head. Inset shows a PL on the ABS surface. (bottom) An SEM image of modified H-shaped PL array. Our current flying head can carry up to 16,000 lenses, The lithography throughput can be dramatically enhanced by employing PLs array for parallel writing.

Chapter 4 PNL Medium

4.1 Structure of HDD media

Today's HDD uses magnetic thin film to record information. Figure 4.1 shows a schematic of HDD medium. To support a high areal density and keep a very durable head-disk interface, the disk surface must be very smooth with minimal defects and waviness to minimize possible contacts during high speed scanning. Disks are fabricated using sputtering of multiple metallic films and a protective overcoat layer. The protective overcoat usually is diamond-like-carbon (DLC) that is covered by a thin layer of Perfluoropolyether (PFPE) as a lubricant layer to improve the durability of the head disk interface. As the areal density increases, the decreasing magnetic spacing requires a lower FH as well as a thinner protective overcoat.

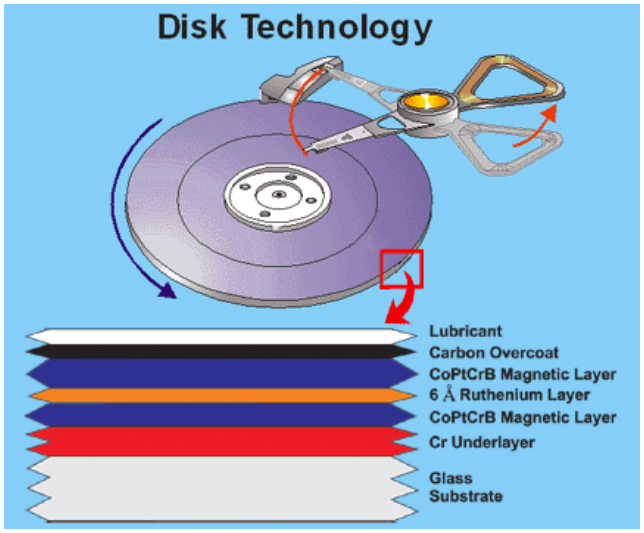

Figure 4.1: Schematic of layered HDD disk medium (from HGST)

4.2 Structure of PNL Medium

4.2.1 Choices of Resists

Many efforts have been made to fly airbearing surfaces on different types of material for varieties of purposes, such as optical recording and microscopy [108-125]. In the application of

PNL, we need to fly the airbearing surface above a resist layer. And it is desirable to have a resist layer with good mechanical properties, high resolution and good compatibility with the thin film disk fabrication process.

Conventional photoresists used in photolithography are mostly organic and photon based. Typically they have some type of photon absorbers to collect incident photons and generate chemicals to initiate a series of reactions. In order to enhance the resist sensitivity, most of them use a chemical amplification method to reduce the amount of photons required for the exposure reactions. However, this chemical amplification approach is a diffusion based process which will limit the ultimate lithography resolution. Although some current photoresists designed for 193 nm are capable of reaching a resolution of 16 nm with special treatments, they are not good choices for PNL due to their poor mechanical properties, high dosage requirement and method of film preparation.

In this work, we chose solid inorganic materials as a resist layer because of their good mechanical properties, low required dosage and sputtering compatible deposition process. Many composites and alloys can be used for resist purposes including TeO, Ge-Sb-Te-Bi, Ge-Sb-Te, Sb-Se-Te, In-Sb-Te, Ge-Te-Sb-S, Ag-In-Sb-Te, Si/Cu, AlSi, LiNbO3, α-Si and Poly-Si. Many of them are currently used for optical recording purposes and their working mechanism mostly relies on phase transitions driven by temperature changes. Some of the materials allow reversible phase change and are used in rewritable optical disks, such as Ag-In-Sb-Te and Ge-Sb-Te. Figure 4.2 shows a schematic of an optical disk with phase-change layers as recording media.

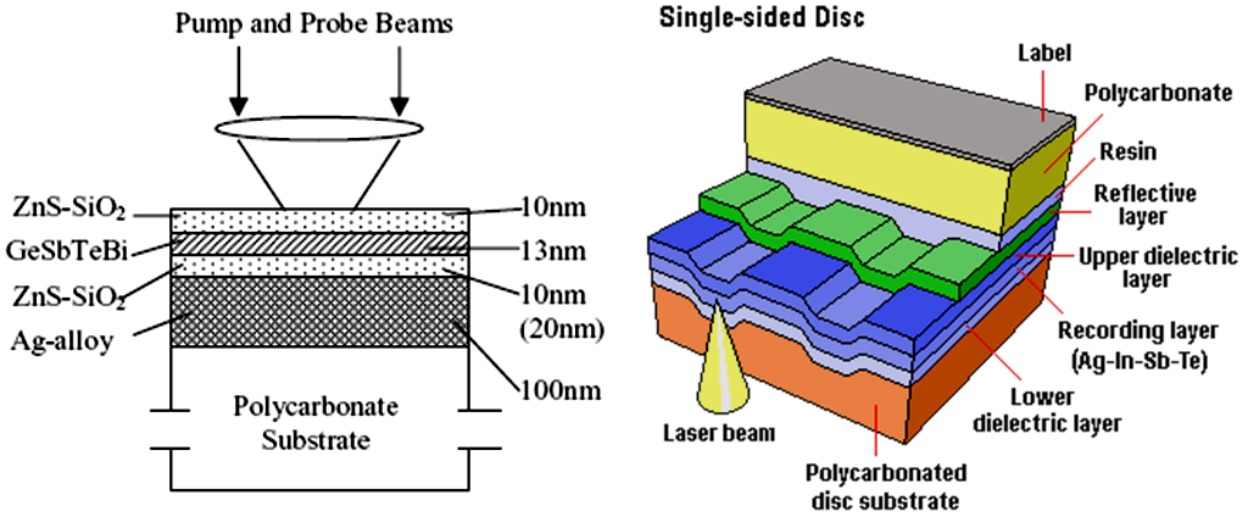

Figure 4.2: Schematic of an optical disk with phase-change layers as recording media

As an example, the media AgInSbTe from the group of chalcogenide glasses, can be switched between crystalline state and amorphous state under different laser treatments. At the amorphous state, a long duration (>10 ns) and lower-intensity laser irradiation will heat up the material to its crystallization temperature but still below its melting temperature. At the crystalline state, a short

duration (<10 ns) and high-intensity laser irradiation will heat up the material to its melting temperature and cool it down quickly to the amorphous phase. The amorphous phase has lower reflectivity than the crystalline phase, therefore, the optical data can be recorded to and read from the optical disk. These phase changes are also associated with changes of both electrical properties and chemical properties. The unique phase reversible electrical characteristic makes phase-change memory useful as a non-volatile memory. With appropriate choices of etchants and reaction conditions, the phase induced chemical properties changes make them also useful as thermal type resist materials, such as TeO [126] and Ge-Sb-Te [94, 127].

4.2.2 Phase-change PNL Resist

In our work, we developed an inorganic thermal resist $(TeO_2)_xTe_yPd_z$ [x≈80% wt., y≈10% wt., z≈10% wt.] as a positive thermal resist working with alkaline solution for the application of PNL. Pd is added to the Te-TeO_x in order to enhance the exposure uniformities and resist resolution by forming finer crystalline grains during phase transition, and its thermal stability is also greatly and beneficially improved. In comparisons with organic photoresist, the new resist has mechanical properties close to glass which is much better than those of organic polymers in terms of Young's modulus and hardness. And this inorganic resist can be deposited onto standard substrates using RF sputtering methods. This preparation method is critical because the resist layer and protective overcoats can be easily deposited sequentially in the same sputtering tool without breaking the vacuum which is important to avoid surface contaminations caused by exposure to the air. The ultimate resist resolution is mainly determined by the grain size and the spatial temperature profile. Using proper preparation method and exposure conditions, the obtained feature size can reach 10 nm or even smaller.

In our application, the $(TeO_2)_xTe_yPd_z$ layer was positioned using RF sputtering while flowing Ar and O_2 gases. This deposition condition produces fine particles of the Te-Pd based materials and amorphous TeO_2 homogeneously distributed inside the film. When the temperature rises to a level high enough to induce phase-change, Te-Pd based crystals will grow and TeO_2 becomes continuously distributed among Te-Pd based crystals. The phase change process is also associated with an optical transmission change. Because of the high etching rate of TeO_2 in alkaline solution, the phase-changed materials can be developed by alkaline solution. But phase-unchanged materials are not dissolved because the Te-Pd based fine particles are insoluble in alkaline solution and can stop the etching process.

In order to calibrate the phase transition temperature, a digital hot plate was used to heat up the different film samples uniformly to different temperatures. At the film temperatures below 200 ºC, no obvious optical transmission change could be observed. When the film temperature reached 200 ºC, the optical transmission began to drop as the film temperature increases and this dropping trend slowed down after the temperature went beyond 350 ºC.

After the hot plate tests, the heated films were put into dilute KOH solutions with different PH values for 30 seconds to study their etching rates. When PH > 11 both phase-changed and

phase-unchanged films were etched away quickly, and when PH < 9 neither phase-changed nor phase-unchanged films were obviously etched within 30 seconds. At PH ≈ 10, only the phase-changed films were etched within 30 seconds. Therefore, a KOH solution with a PH value of 10 was chosen as the developer for this TeO_x based thermal resist.

Figure 4.3 shows AFM images of laser heating test results. A CW Argon laser was used as the light source operating at 365 nm wavelength and 250 mW output power. A high NA (~0.42) UV graded aspherical lens was used to focus the light onto a 100 nm thick resist film surface at a linear scanning speed of ~1 cm/sec. At this scanning speed and laser power level, heat can quickly accumulate locally and the temperature quickly rises high enough to melt and even burn the resist layer.

As shown in Figure 4.3(a), the highly concentrated laser power generated a 2-μm wide groove at the heating location. Some of the materials were re-deposited on both sides of the groove. The heat conduction also generated a temperature profile around the heated spot to induce the phase transition. No obvious topographic changes were found in these phase-changed regions but visible changes could be observed optically under the microscope. As shown in Figure 4.3(b), after development in diluted KOH solution, the phase-changed regions were found to be etched away leaving some recessed grooves. As shown in Figure 4.3(c), with reduced laser power or/and increased scanning speed, the size of direct burning marks also reduced continuously and eventually vanished.

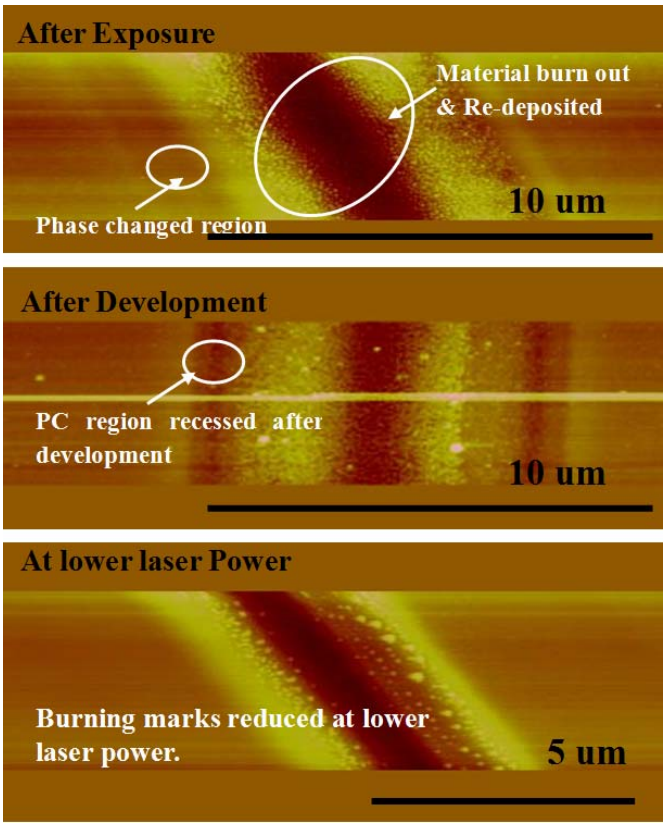

Figure 4.3: AFM images of laser heating test results. (a) The highly concentrated laser power generated a 2-μm wide groove with induce the phase transition and materials re-depositions. (b) The phase-changed regions etched away after development in diluted KOH solution. (c) With reduced the laser power or/and increased scanning speed, the size of direct burning marks also reduced.

At a linear speed of 5 m/s and 30 mW laser output power, no obvious topographic marks were found before development. After being developed for 30 seconds, the sample showed about 1 μm wide exposure marks with well defined side walls, as shown in Figure 4.4.

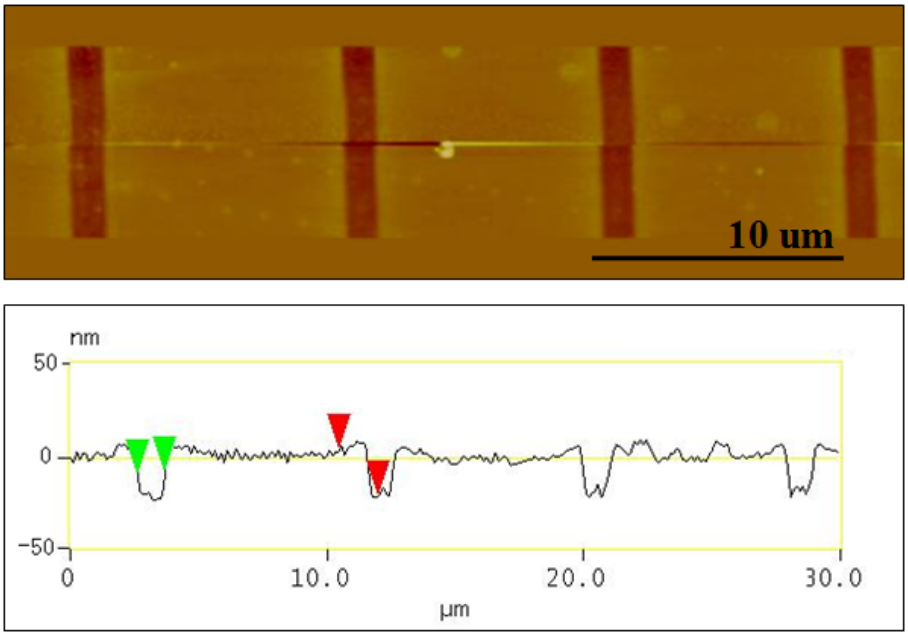

Figure 4.4: Topography (top) and cross-section (bottom) view of AFM image showing about 1 μm wide exposure marks with well defined side walls.

4.2.3 Disk Tribological Designs

Although TeO_x based inorganic resist has much better mechanical properties than organic resist, it is still relatively vulnerable in a high speed scanning process, especially when the flying head is in contact with the resist surface. The possible contacts between the plasmonic flying head and resist surface could generate particles which can likely lead to catastrophic interface failures. In order to improve the reliability of the head-disk interface, we used additional overcoats and a PFPE lubricant to protect the resist layer during the PNL process. Protective overcoats were also used on the plasmonic flying head to protect the PL metal film.

Protective overcoats, such as Diamond-like-carbon (DLC) and CN_x which are commonly used

in magnetic recording applications can be helpful for preventing contact induced resist and PL damages. On the flying head, we used DLC overcoats prepared by the sputtering process. In order to improve the adhesion of the DLC to the metal film, a thin transition layer of carbide film was employed by co-sputtering the Cr and metal simultaneously. The hardness of the DLC film was measured using a nano-indenter (Hysitron Inc.) to confirm the mechanical properties. For tribological consideration, it is desirable to use DLC films with high Young's modulus (E), high hardness (H) and moderate H to E ratio, so the films won't be too soft or too brittle. Figure 4.5 shows an example of a nano-indentation measurement result of a 70 nm thick DLC overcoat deposited on a Si substrate. An ultra-sharp nano-indenter tip (NorthStar^{TM} Cube Corner) with tip radius < 50 nm was used in the test and the engage depth was about 30 nm at the load of about 200 μN. The measured hardness and Young's modulus were 22.75 GPa and 161.5 GPa respectively, and the obtained results accord well with our expectations. It should be noted that the measured results are effective values for the DLC film and Si substrate system because the indentation depth is at the same order of DLC film thickness.

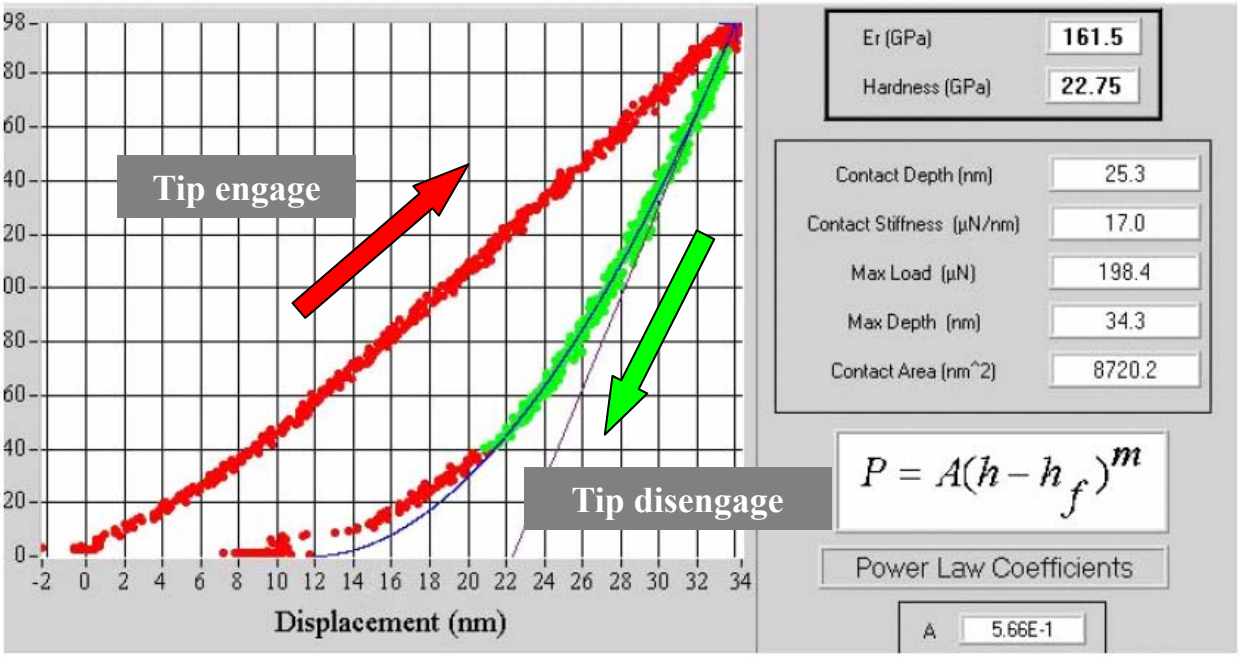

Figure 4.5: An example of DLC film nano-indentation results performed on a 70 nm thick DLC overcoat on a Si substrate.

Due to facility limitations, a Si_3N_4 film, rather than DLC, was deposited onto the resist layer by magnetron sputtering as a protective overcoat. An atomically thin layer of Cr is used as an adhesion layer between the resist layer and Si_3N_4 overcoats. Both disks and flying heads were examined using AFM. The RMS roughness value after deposition of the protective overcoats is about 0.3 nm which is almost the same as that of the substrate before film depositions.

Furthermore, a 2-nm thick lubricant Perfluoropolyether (PFPE) was also dip-coated on the top

of overcoats. The lubricant thickness is controlled by varying both the linear pull-out speed and solution concentration. A long travel computerized micro-stage with ultra smooth motion was used in order to reduce the lubricant micro-waviness generated during the dip-coating process. The lubed disks were later examined using an Optical Surface Analyzer (Candela OSA 5100) for thickness and uniformity.

This tribological configuration greatly reduces the friction and possible damage when the slider is in contact with the disk surface. The tribological performance was verified using a homemade white light interferometer with an Acoustic Emission (AE) system and a Laser Doppler Velocimeter (LDV OFV-512 Polytec). With these tribological properties, we were able to directly load our flying heads on to the disk at 10 m/s disk velocity without damaging the underneath resist layer and PL structures.

4.2.4 Thermal Designs

As shown in Figure 4.6, the PNL is a dynamic process involving the competition of high speed scanning, thermal diffusion, heat accumulation and optical absorption. The laser light is delivered onto the PL by a high NA UV objective through the transparent flying head substrate. Besides the optical energies reflected away by the metal film, a majority of energy is absorbed as heat and only a small portion was coupled by SPPs into nearfield optical irradiation at the other side of PL to pattern the resist layer. Beside the previously addressed tribological issues, there are still two other thermal challenges to be tackled in the PNL application. One is the heat management of the lithography head, and the other one is the nanoscale heat confinement in the resist layer.

In the plasmonic flying head, all of the generated heat is dissipated away mainly by two means, 1) heat conduction into the bulk head material, and 2) thermal irradiation and heat conduction through the air gap into the disk. Thermal management of the plasmonic flying head is important to ensure the flying head's durability and the pattern uniformity. Excessive optical heating could seriously damage the metal structures as shown in Figure 4.7. Figure 4.7(a) shows an AFM image of a modified bull's eye PL fabricated on a quartz substrate with 80 nm thick aluminum films. Figure 4.7(b) shows an AFM image of the same PL after burning with 30 mW CW UV light at 365 nm wavelength for about 30 seconds. It is shown that the local heat accumulation under this configuration can generate a temperature field high enough to cause interface damage between aluminum and quartz. An even high laser power could melt the PL structure. In order to use the PL at a much high laser power, which is required for the high speed scanning, sapphire substrate is used to replace the quartz because of its high thermal conductivity and excellent mechanical properties. After switching to sapphire, the damage threshold was found to improve by one order of magnitude in the same laser burning test. This sapphire based configuration allows us to use up to 300 mW of CW laser power to illuminate a single PL, but it still will not allow us to parallelize many of them in a close-packed form due to the high power requirement of each PL. In order to use PLs in a close-packed form, we need to reduce the laser power consumption of each lens by at least one order of magnitude.

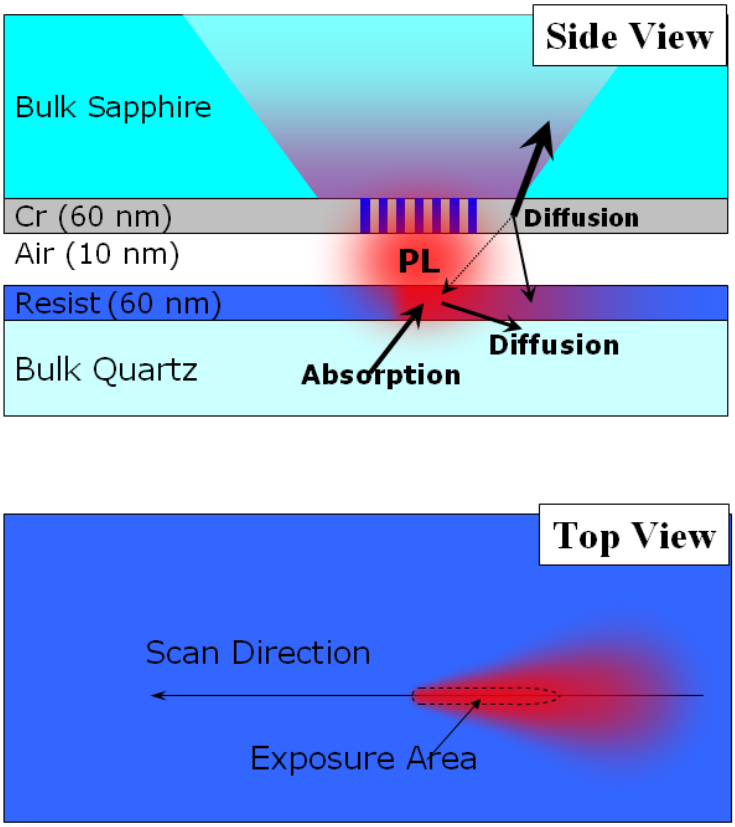

Figure 4.6: Illustration of the PNL process. It involves the competition of high speed scanning, thermal diffusion, heat accumulation and optical absorption.

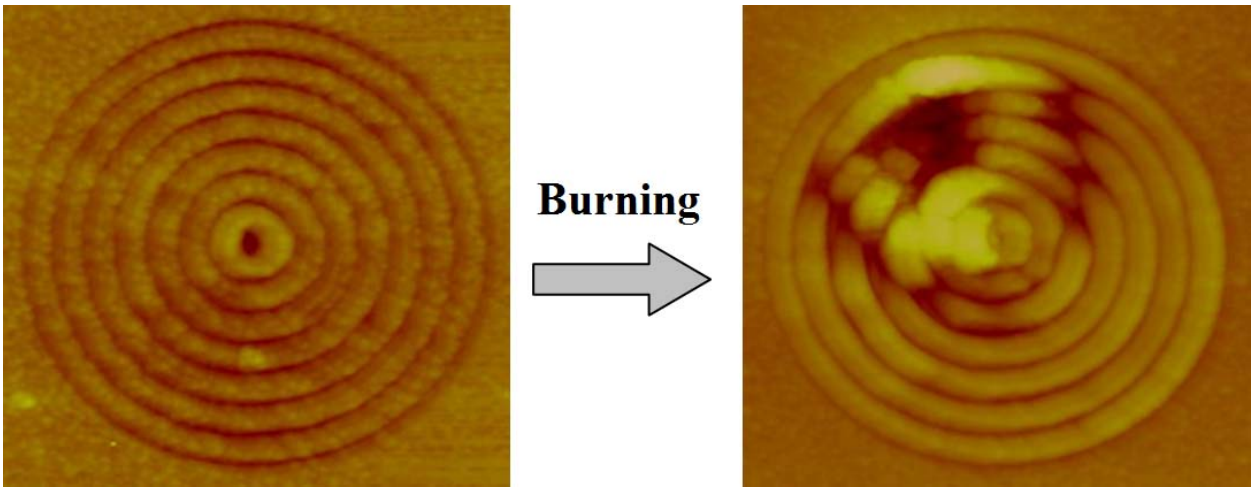

Figure 4.7: AFM image of PL topography before (left) and after (right) excessive optical heating. PL fabricated on a quartz substrate with 80 nm thick aluminum films.

At the disk side, the problem is more than avoiding thermal damage we must also ensure the high thermal confinement and good pattern uniformity. As discussed previously, the formation of the thermal pattern is a process involving the competition of high speed scanning heat diffusion, heat accumulation and optical absorption. After the heat is deposited into a small volume of the resist layer, it rapidly diffuses into its neighborhood and the disk substrate. As a result of thermal diffusion, the heat affected region in the resist layer grows and the peak temperature also reduces accordingly. If the heating spot continuously drags along the resist surface, it will leave a drop-shaped exposure mark as shown in Figure 4.8 and also illustrated in Figure 4.6. This result confirmed that the heat diffusion distance determines the required exposure dosage for recording and heat accumulation can greatly affect the uniformity of exposures. A solution to this issue will be presented in the following discussions.

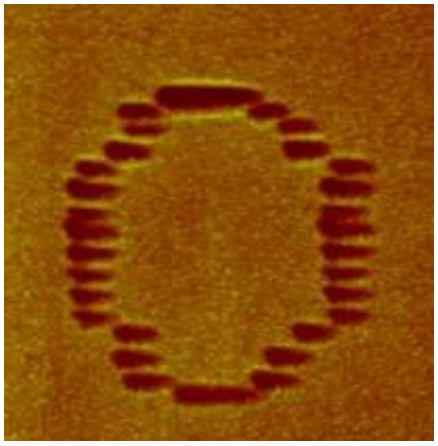

Figure 4.8: An example of drop-shaped exposure marks due to heat accumulation.

In practice, we want to both reduce the laser power requirement and minimize the heat accumulation effect to improve the pattern uniformity and resolution. A layer of heat sink underneath the resist layer significantly helps improve the sub-micron scale pattern uniformity and similar approaches have been widely used in CD/DVD recording media. But when the feature size is comparable to or smaller than the resist thickness (on the order of 50 nm in current PNL experiments), this approach itself is not adequate.

The key solution to the above issues is to lower the required operating power level by controlling the heat diffusion at the nanoscale. The thermal diffusion length is a function of time and material properties (mainly thermal diffusivity). By switching to an ultrafast laser source, we can greatly reduce the thermal diffusion length, and therefore confine the heat within a much smaller region to achieve lower laser power consumption, good pattern uniformity and high feature resolution.

Figure 4.9 shows a log-log plot of an estimation for the required laser pulse energy to generate one isolated 50-nm dot mark at different pulse durations. It assumes a PL with a perfect 50-nm

focus spot and a scanning speed on the order of 10 m/s. The solid curve corresponds to the amount of required laser pulse energy normalized to the minimum required energy E_0 which is the amount of energy needed to change the phase for a semispherical material volume of 50-nm diameter without affecting any of its neighboring materials. The trend shows that the amount of required energy grows dramatically as the pulse duration increases. This increasing trend grows more rapidly as the exposure feature size gets smaller than 50 nm.

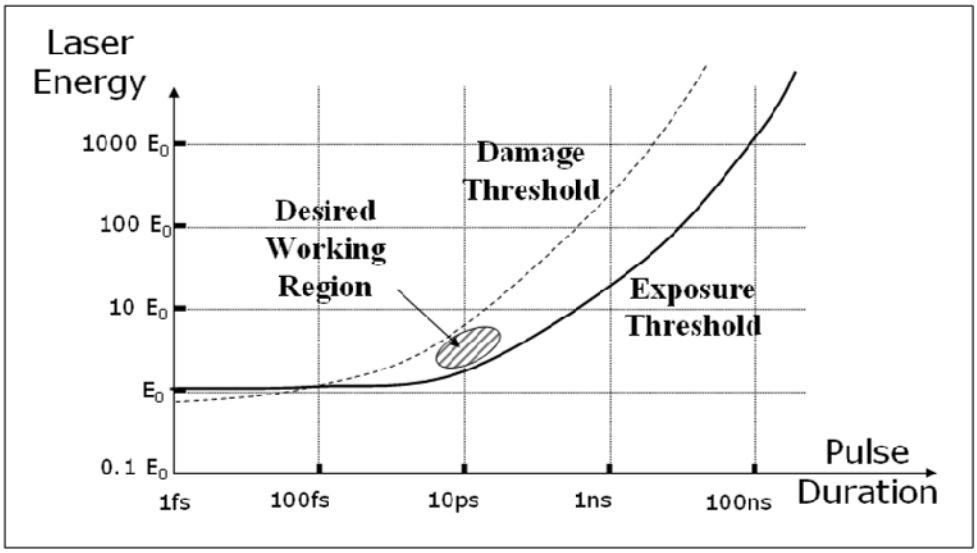

Figure 4.9: A log-log plot of estimated laser pulse energy required to generate a single 50-nm diameter exposure mark at different pulse durations where E_0 is the amount the energy needed to change the phase for a semispherical material volume with 50-nm diameter.

As an example estimation at 50 nm singe spot writing at 10 m/s, i.e., 500 MHz with 2 ns time interval, the minimum average power required to expose the resist using 2 ns pulse interval is about ~1.5 mW considering a 100 nm thermal diffusion length, which corresponds ~3 pJ heat per time interval. It requires 300 mW CW laser operating power per lens considering the case of 50% light delivery efficiency, 2% PL coupling efficiency and 50% resist absorption efficiency. In comparison with the case of 10-ps pulsed laser source, the minimum average power required to expose the resist with the same 2 ns time interval is about ~0.05 mW considering a 10nm thermal diffusion length, which corresponds ~0.1 pJ heat per pulse. It only requires 10 mW average laser operating power per lens using the same optical system and plasmonic structure.

One of the disadvantages of using ultrafast lasers in PNL is their pulse induced structure damage such as ablations. The dashed line in Figure 4.9 shows the estimation of the damage thresholds for the PL used to focus and deliver the energy to the resist layer. The damage thresholds show a similar trend as the curve for required energy. The vertical distance between the two curves defines the working margin where laser power is high enough to generate exposures but not high enough to damage the PL. This estimation shows that an optimal working region

operates at the pulse duration close to 10 ps.

Table 4.1 shows an itemized comparison between a 10-ps pulsed ultrafast laser and a 2-ns modulated CW laser. The 10-ps ultrafast laser promises patterns with much finer feature size and pattern contrast. As shown in the previous estimation, the overall power is reduced by roughly 30 times which will significantly reduce the heat accumulation effect and allow the employment of the close-packed PL array for parallel pattern purpose.

Table 4.1 Comparison between a 10-ps pulsed laser and a 2-ns modulated CW laser.

Items	**10 ps ultrafast laser**	**2 ns modulated CW laser**
Required Average Power	1×	30×
Working Margin	1×	2×
Heat Accumulation Effect	1×	30×
Exposure Contrast, i.e., Temperature gradient	10×	1×
Expected Litho Feature Size	10 nm × 10 nm	20 nm × 100 nm
Number of PLs supported	PLs arrays for parallel patterning	A few PLs

It should be mentioned that, in processing of larger scale and dense patterns where the heat accumulation still can affect the pattern uniformity, a heat sink structure consisting of a high thermal conductive metallic layer and a low thermal conductive dielectric layer underneath the resist layer will be very helpful.

4.2.5 Lubricant and Overcoats Stability

Similar to the heat-assisted magnetic recording (HAMR) system, which also requires the nanoscale local heating of the recording media to several hundreds of degrees higher temperature within a nanosecond, such a high and rapid temperatures change can lead to catastrophic head-disk interface failure due to the desorption and/or degrading of the lubricant and the overcoats [128]. In this part of the study, we used plasmonic flying heads to investigate the effects of nanoscale laser irradiation on the disk lubricant under different laser heating power levels and laser heating cycles. After each test, the disk surface was examined using a Candela OSA to study the medium surface.

Figure 4.10 shows the scheme of the lubricant durability tests. Because of the spatial

resolution limitation of the Candela OSA, we performed the lubricant laser burning test by scanning the PL over a 50-um wide strip consisting of multiple adjacent patterning tracks. Free space direct laser burning tests were also performed for comparison purposes. In the direct laser burning tests, the laser source was synchronized and modulated according to the spindle's motion in order to better distinguish the generated marks. Furthermore, in order to exaggerate the lubricant changes, the head radial scan speed was varied in the range of 20~40 nm/s which is one order slower than the typical radial scan speed in the common lithography tests. All of the following tests were performed with the lubricant PFPE Z-Tetroal at a spindle speed of 1000 rpm, corresponding to a disk velocity of about 4 m/s.

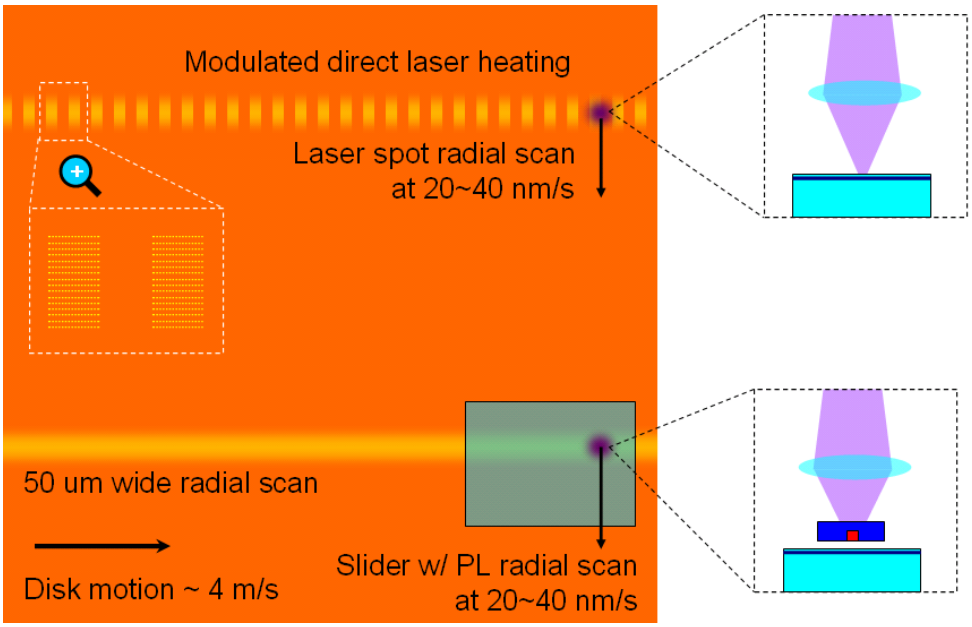

Figure 4.10: Scheme of lubricant durability tests.

Figure 4.11 shows the results of three flying tests at different radial positions of the same medium. The top two were performed as lubricant laser burning tests with laser power of 30 mW. The radial scan speeds are 25 nm/s and 40 nm/s, respectively. And the third one was performed with the laser off and scanned at 40 nm/s for comparison purpose. It can be clearly seen that the laser indeed caused visible lubricant changes in addition to those generated by the ABS, and a larger number of burning circles produced more obvious marks.

Figure 4.12 shows multiple lube laser burning tests at different radial positions by varying the laser power levels as labeled. The radial scan speed was kept at 40 nm/s for all tests. From the OSA scans we can see that higher laser power levels generated more obvious marks and no distinguishable marks were found at laser power levels below 27 mW. The disk was examined with the Candela OSA one day later to allow the lubricant to reflow in order to study the lubricant relaxation, and it is seen that the scan results showed the visible signs of lubricant relaxation.

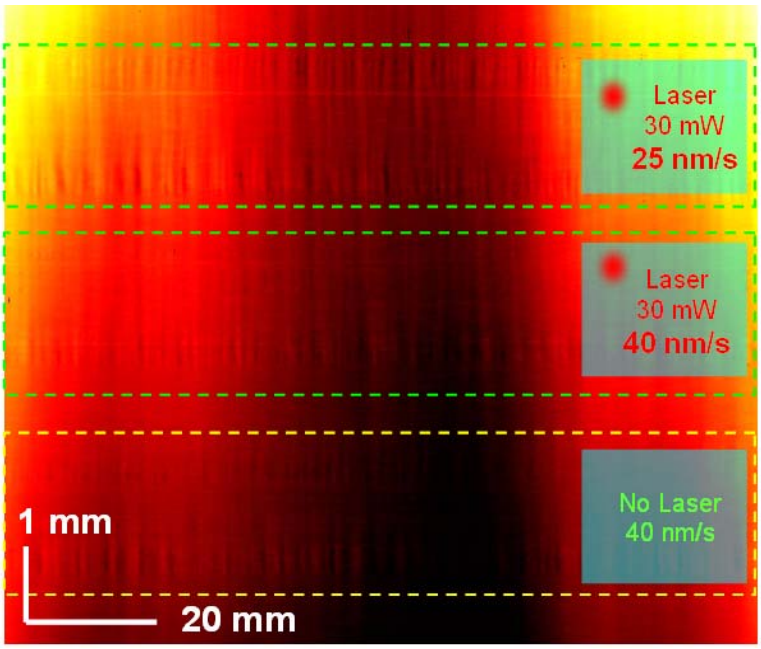

Figure 4.11: Three lubricant flying tests at different radial positions of the same disk under different laser irradiation conditions.

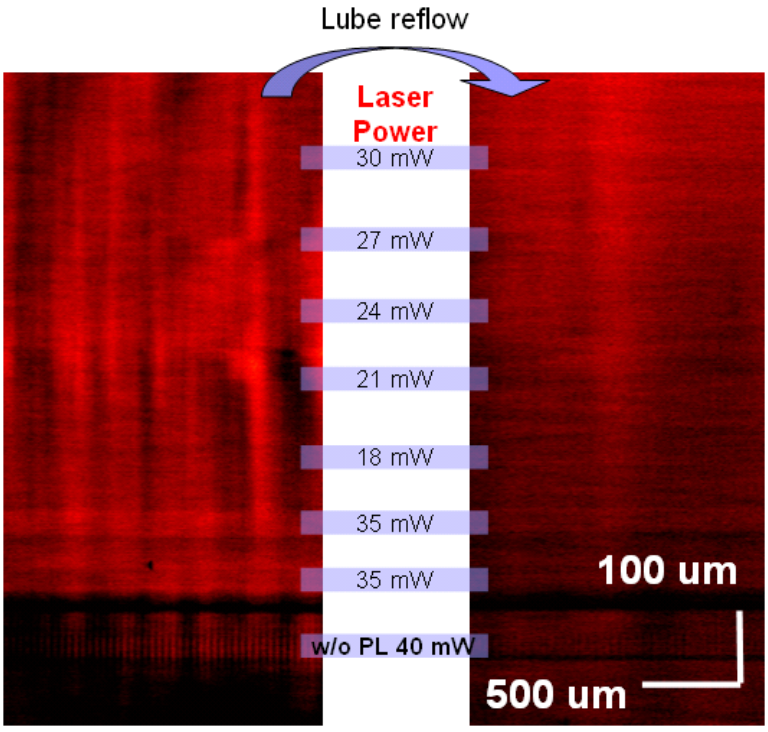

Figure 4.12: Multiple tests at different radial positions and the laser power levels.

Figure 4.13 shows a single lube laser burning tests at the laser power of 33 mW and a radial scan speed 30 nm/s. The top figure shows clear marks of a laser caused burning line, ABS caused depletion line and wash-board-like modulation marks. The middle figure shows the lubricant relaxation result after 4 days. And the bottom figure shows the OSA scan after removal of the mobile lubricant by soaking the disk in HFE7100 for 1 hour. These test results clearly indicated that the laser irradiations not only caused lubricant changes in the mobile part but also the bonded part and/or the protective overcoats were affected too.

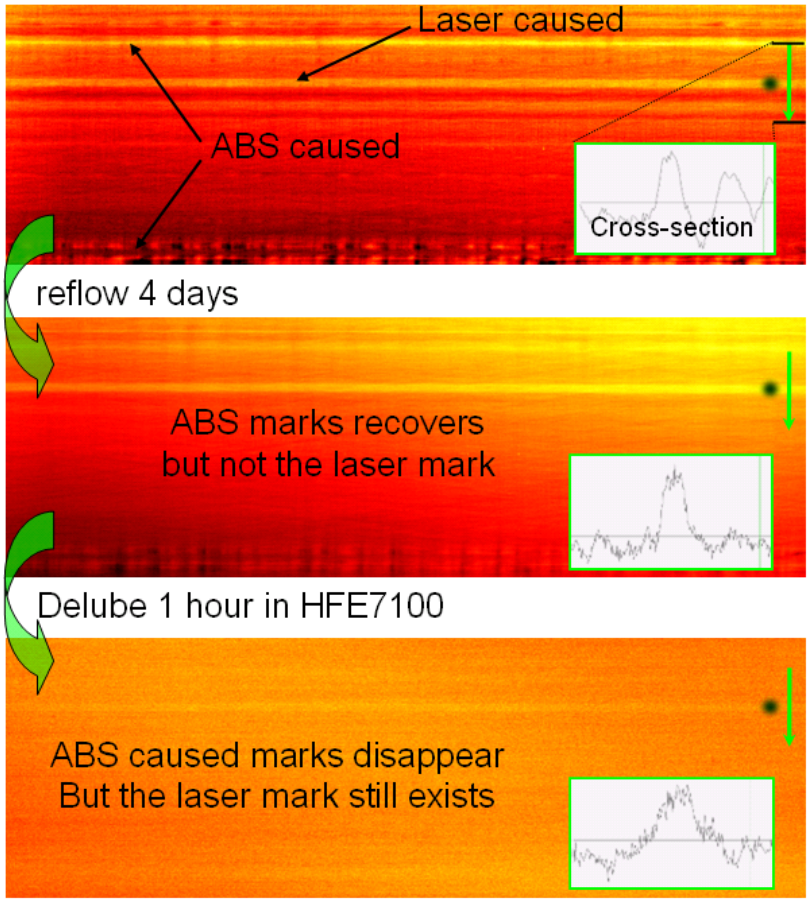

Figure 4.13: Comparison between a laser caused and ABS caused lubricant changes.

Figure 4.14 shows a comparison burning test between the free space laser and nearfield PL under the same laser power of 33 mW and a radial scan speed of 25 nm/sec. We found that the free space laser source caused similar but weaker lubricant changes although a much larger amount of photons reached the disk surface. One of the possible explanations is, although the PL only coupled a small percent of the overall laser energy, it generated an enhanced peak light intensity which is a few times stronger than that of the incident light. This higher light intensity lead to higher peak temperature which could greatly accelerate the lubricant degradation. This phenomenon agrees well with the trend of lubricant thermal degradation.

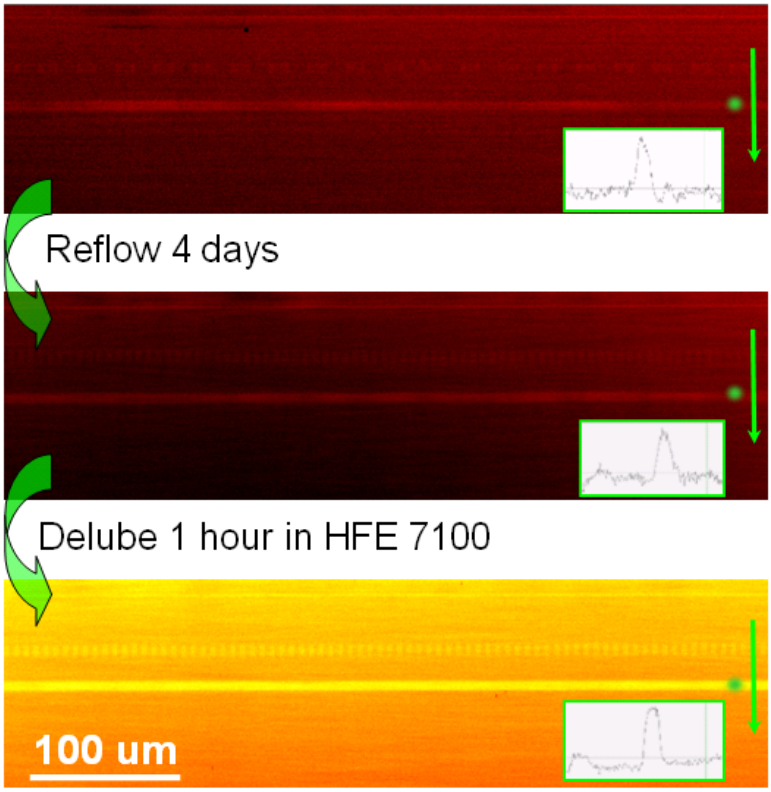

Figure 4.14: Comparison between a direct laser irradiation and PL coupled laser irradiation.

The lubricant laser irradiation test results show the lubricant is still functional in the current lithography process. But because more obvious lubricant degradation phenomena were observed when working with the PL with high local field enhancement, it might become a critical issue as both the patterning feature size reduces and PL efficiency improves.

4.3 Summary

In this chapter, we presented the medium structure specially designed for the PNL process. An inorganic thermal type phase-change resist was developed, tested and prepared. Both the resist working mechanism and nanoscale thermal management of the head-disk interface were investigated. Advantages of using an ultrafast laser in the PNL were also discussed based on the properties of the proposed resist layer. Potential lubricant failure modes were experimentally studied.

Chapter 5 Plasmonic Nano-Lithography System

5.1 Base System

In the base PNL system, the firing of a laser is synchronized with the position of the plasmonic flying head enabling lithography of arbitrary patterns as illustrated in the configuration shown in Figure 5.1. The ultra high speed firing of the laser is controlled by a high speed optical modulator controlled by the signal from a pattern generator, created according to the object to be written on the resist as predefined and loaded. As shown in previous chapters, the laser light illuminated upon the PL is focused into a nanoscale spot. And the air bearing spindle on which the disk is mounted allows the resist-coated recording disk to be spun at extremely high-speeds equivalent to a disk linear velocity of several meters per second while maintaining the close proximity gap between lens and resist by use of the advanced airbearing surface (ABS) technique that allows the exposure of sub-wasvelength details. The relative position of the head to the disk can be obtained from the angular position of the disk from the spindle encoder and the radial position of the nanostage, which holds the head. This position information is used to control the firing of the laser to achieve the desired pattern. The previously introduced inorganic TeO_2 based thermal type resist is used as the recording medium due to its superb mechanical properties, good sensitivity and high resolution.

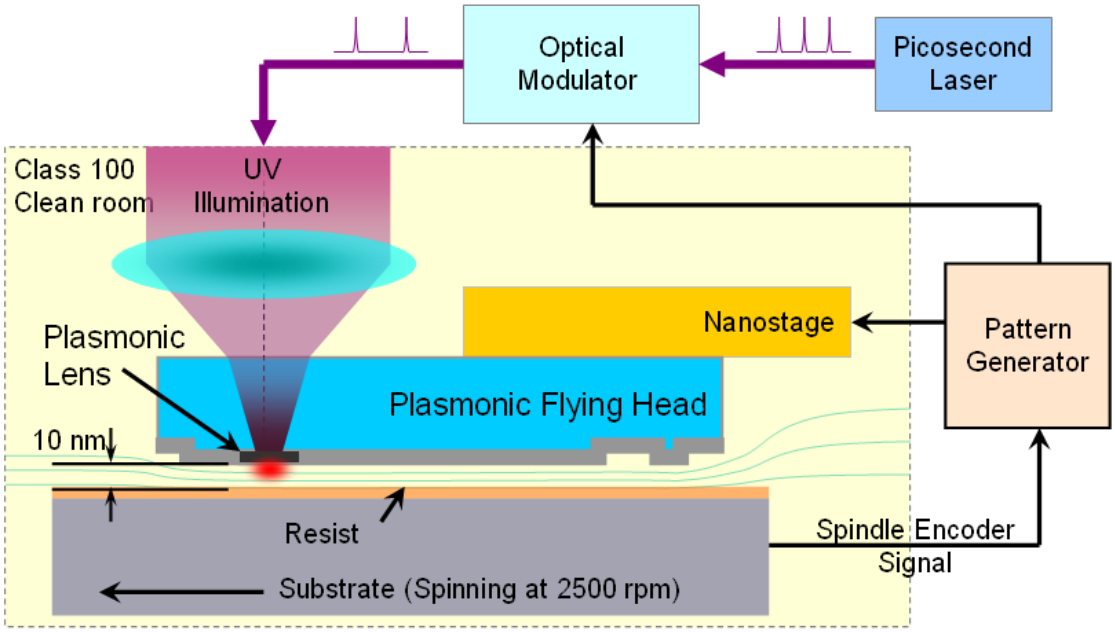

Figure 5.1: A schematic of the PNL experimental setup. The PL focuses ultraviolet laser pulses onto the rotating substrate by concentrating surface plasmons (SPPs) into nanoscale spots. An advanced airbearing surface (ABS) technology is used to maintain the gap between the lens and the substrate at 10 nm. A pattern generator is used to pick the laser pulses for exposure through an optical modulator according to the angular position of the substrate from the spindle encoder and the radial position of the flying head from a nanostage.

Similar to most other maskless lithography approaches, it is a great challenge to manage large scale arbitrary patterning especially for the PNL in order to fulfill its potentials of good reliability, high throughput and very high resolution. Many issues need to be addressed including wafer throughput, die-to-database pattern inspection, pattern stitching and controlling the variability between beams in multi-beam systems.

In particular for PNL, these issues such as data and pattern management, pattern positioning error control, need to be considered and addressed in order to achieve good system performance, including patterning accuracy, process reliability and manufacture throughput. In this work, several modularized subsystems were built in addition to the previously illustrated base setup as shown schematically in Figure 5.2, and a system snap-shot is shown in Figure 5.3.

The shown PNL testbed was designed and optimized for an ultrafast pulsed laser, and it includes the laser pulse modulation system, pre-focusing monitoring and CW laser assisted system, mechanical and electronic adjustment system and the FH and light transmission monitoring system.

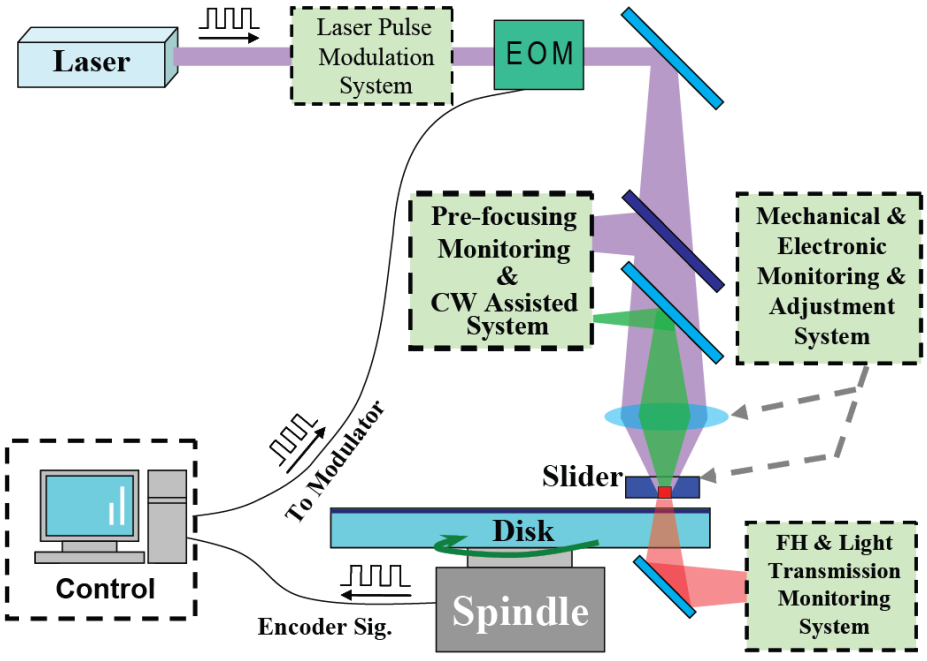

Figure 5.2: Illustration of modularized subsystems in addition to the base PNL system shown

previously.

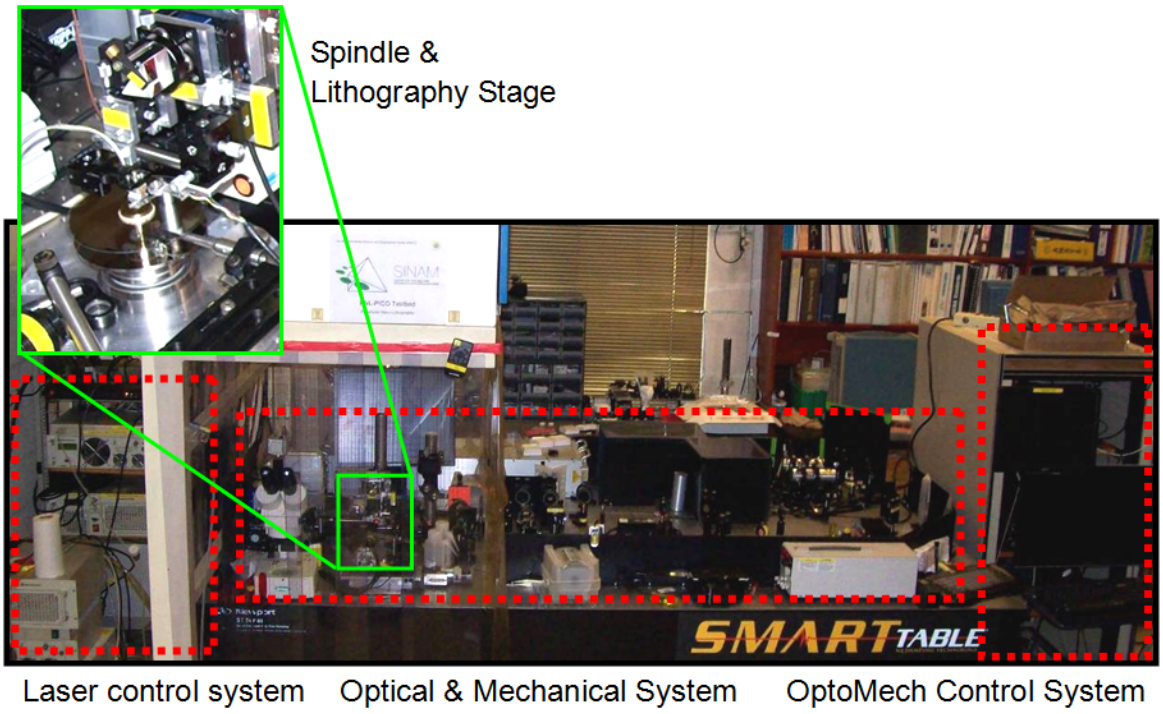

Figure 5.3: Snap-shot of PNL base system

Our first generation of the prototype system aimed for 50nm patterning resolution within a 4-inch wafer. According to the International Technology Roadmap for Semiconductors (ITRS) lithography roadmap (2009 edition), the maskless requirements are the same as the wafer requirements except that the data volume is half that of an optical mask and the grid size is one-quarter of the optical requirements. This leads to small critical dimension (CD) changes, high overlay accuracy between layers and sub-10 nm lithography tool positioning accuracy in both the radial and circumferential directions.

5.2 Process Monitoring Systems

In order to ensure the process reliability, some monitoring modules are built into the base PNL platform including a FH and PL transmission monitoring module and acoustic emission sensing module.

The FH and PL transmission monitoring module is set to monitor the FH of the plasmonic flying head during the lithography process. This is done by using white-light (or multi-wavelength) interferometry at the head-disk interface together with a visible/UV imaging system. This monitoring system is schematically illustrated in Figure 5.4.

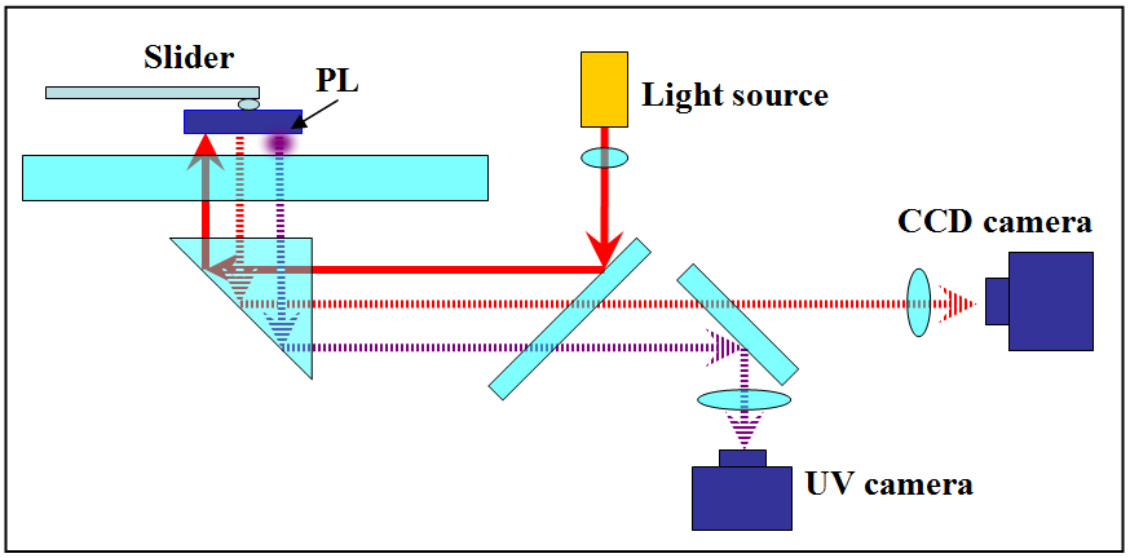

Figure 5.4: Illustration of the FH & PL transmission monitoring module.

In the head-disk interface, this white-light interferometry can achieve a gap sensing resolution reaching 0.1 nm. Without careful calibration and high accuracy sensing modules, this method can still qualitatively provide the spacing information of the head-disk interface. It is worth pointing out that the PL transmission monitoring system only senses the far field propagating components of the transmitted light and the scattered portion of the nearfield components, therefore it cannot provide direct nano-focusing performance of the PL.

5.3 Patterning Data Rate and Lithography Throughput

5.3.1 Pulse Rate Multiplication

The required laser pulse rate of each PL is determined by the relative linear scanning speed and pattern pixel size. For example, a process with 50 nm pixel size and 10 m/s scan speed corresponds a 200 MHz minimum pulse rate, and a four-time higher rate (i.e. 800 MHz) will be more desirable to achieve patterns with good uniformity and accuracy.

Currently, most commercially available ultrafast lasers operate at the repetition rate on the order of 100 MHz. One way to obtain high repetition rate is to internally modify the laser cavity and pulse triggering circuits. An alternative way is to split the laser pulse train into multiple beams, introduce different time delays to each beam and then combine them back, as shown in Figure 5.5. One of the advantages of this alternative approach is that it allows the use of optical modulators with much lower bandwidth. An example optical layout is shown in Figure 5.6, where the laser pulse rate is doubled twice from 80 MHz to 320 MHz using polarizing optics.

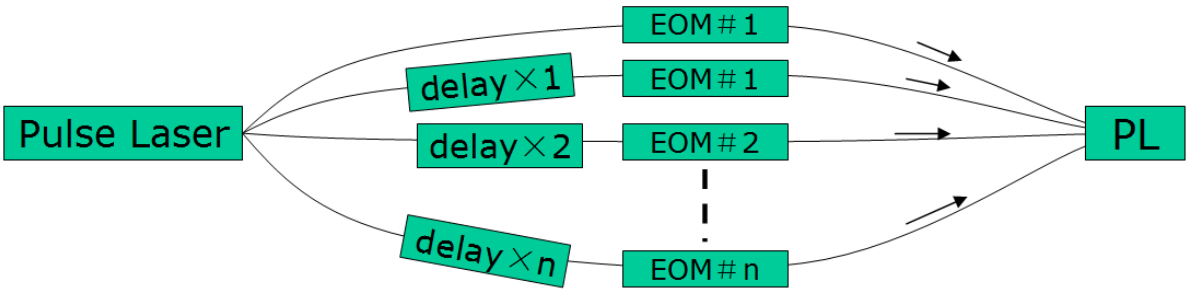

Figure 5.5: Illustration of external laser pulse rate multiplication by introducing different time delays to split beams and then combine them back together.

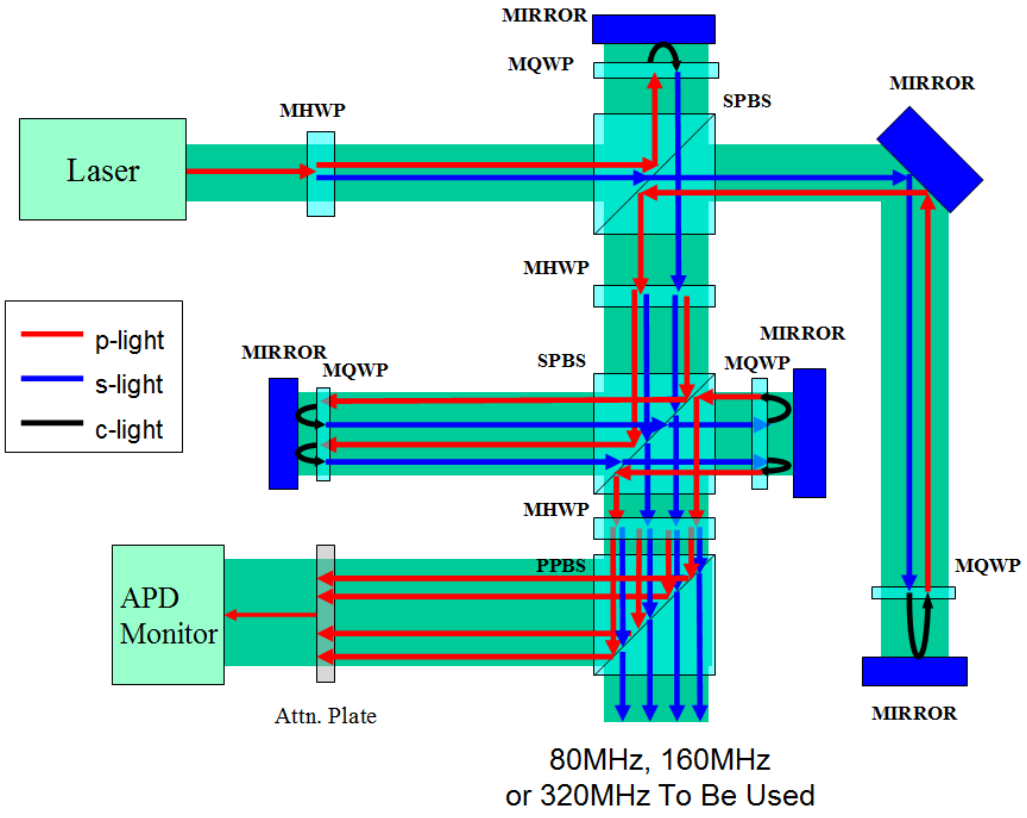

Figure 5.6: A method for doubling the laser pulse rate twice from 80 MHz to 320 MHz using polarizing optics.

In practice, we can also relax this pulse rate requirement by using a combination of different types of PLs (for example, the H-shaped PL and recessed H-shaped PL) during the parallel patterning but it may be at the expense of increasing the complexities of pattern processing and requirements of stitching accuracy.

5.3.2 Parallel Patterning

Although one single PL scanning at a speed of 10 m/s already has much higher throughput than many other maskless lithography approaches, parallelizing multiple PLs will further enhance the lithography throughput. As an example of a previously discussed plasmonic flying head design with modified H-shaped PLs, up to 16,000 lenses can be placed on the bottom of the ABS considering the changes of mean FH and pitch and roll angles at different linear velocities, which allows the patterning of a 12-inch wafer in less than 1 minute. But in practice, it is a great challenge in maskless lithography to independently manage 16,000 lenses and the huge amount of data required for the patterning process. And development of PNL still needs advances in developing high speed and compact modulator arrays or picosecond laser diode arrays.

For many high volume manufacturing applications, another alternative can address the above issue by using synchronized spindle arrays (or multiple lithography heads) associated with modulator arrays (or laser diode arrays) to achieve the desired high throughput, i.e., an array of spindles or lithography heads is synchronized and fed by the same array of modulators or ultrafast laser diodes as illustrated in Figure 5.7.

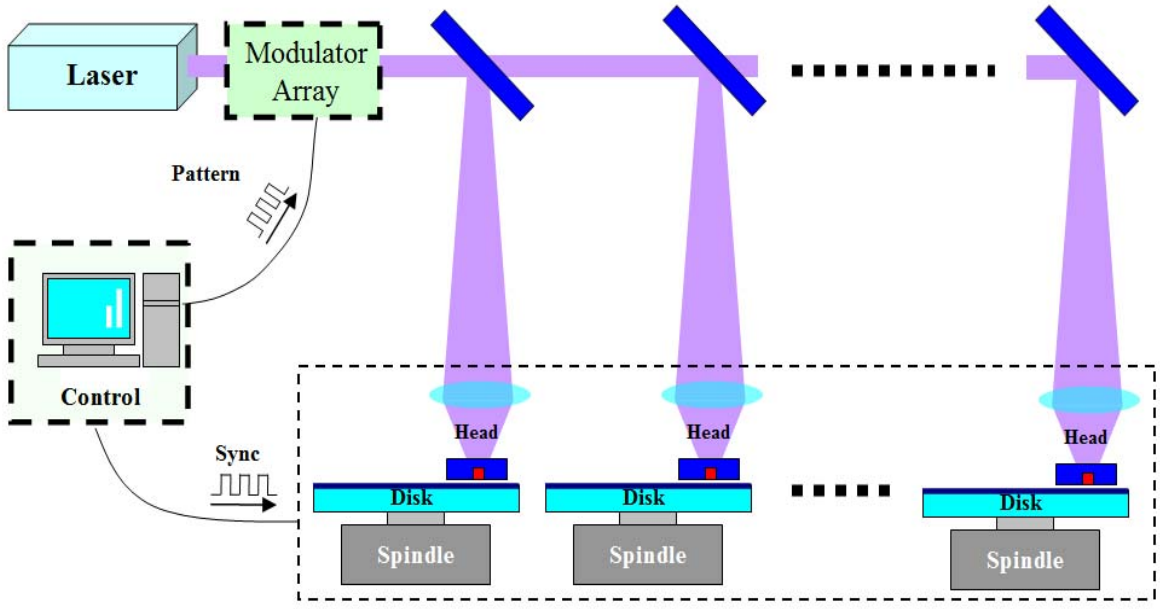

Figure 5.7: Schematic of a parallel array of spindles fed by the same array of modulators to reduce the required number of modulators for high volume mass production.

For example, we consider the case of writing 12-inch wafers at 10 nm resolution close-packed features using 400 lenses per plasmonic flying head (i.e., a 20 by 20 PLs/modulator/laser diode arrays) and 16 synchronized spindles (i.e., a 4 by 4 spindle array) with one head per spindle. The required data feeding rate is about 400 Gb/s which is manageable using current chip and telecom

based technologies. The hourly throughput can be as high as 100 wafers which is more than enough for most of high volume manufacturing.

In this work, we parallelized two PLs for demonstration purposes by placing them 5 μm apart along the circumferential direction as shown in Figure 5.8. Two laser beams are delivered onto two lenses using the same prefocusing lens by using slightly different incident angles. The prefocusing lens focuses both laser beams down to about 2 μm spots, which avoids possible crosstalk between the PLs.

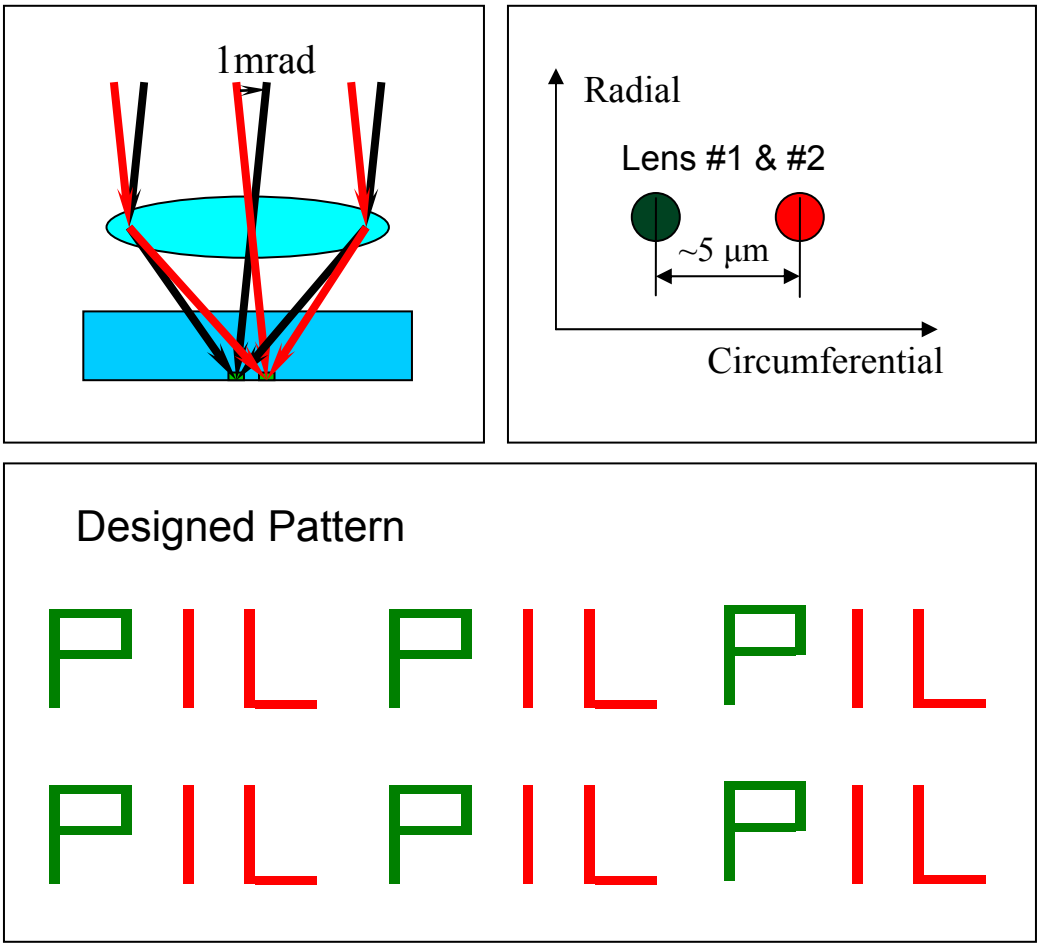

Figure 5.8: An example of parallelizing two PLs for demonstration purposes by placing two PLs with 5 μm separation along the circumferential direction.

As an example as shown in Figure 5.8, two lenses write patterns independently where lens #1 writes the letter “P” and lens #2 writes letters “IL” at 5um away along the circumferential direction. Combination of the two patterns gives the patterns of “PIL” periodically.

In this configuration, two laser beams are controlled independently by two different modulators as shown in Figure 5.9. The current experimental system configuration can support up to 4 PLs for parallel arbitrary patterning due to the limited number of modulators built into the

testbed but it can be expanded by adding more modulators.

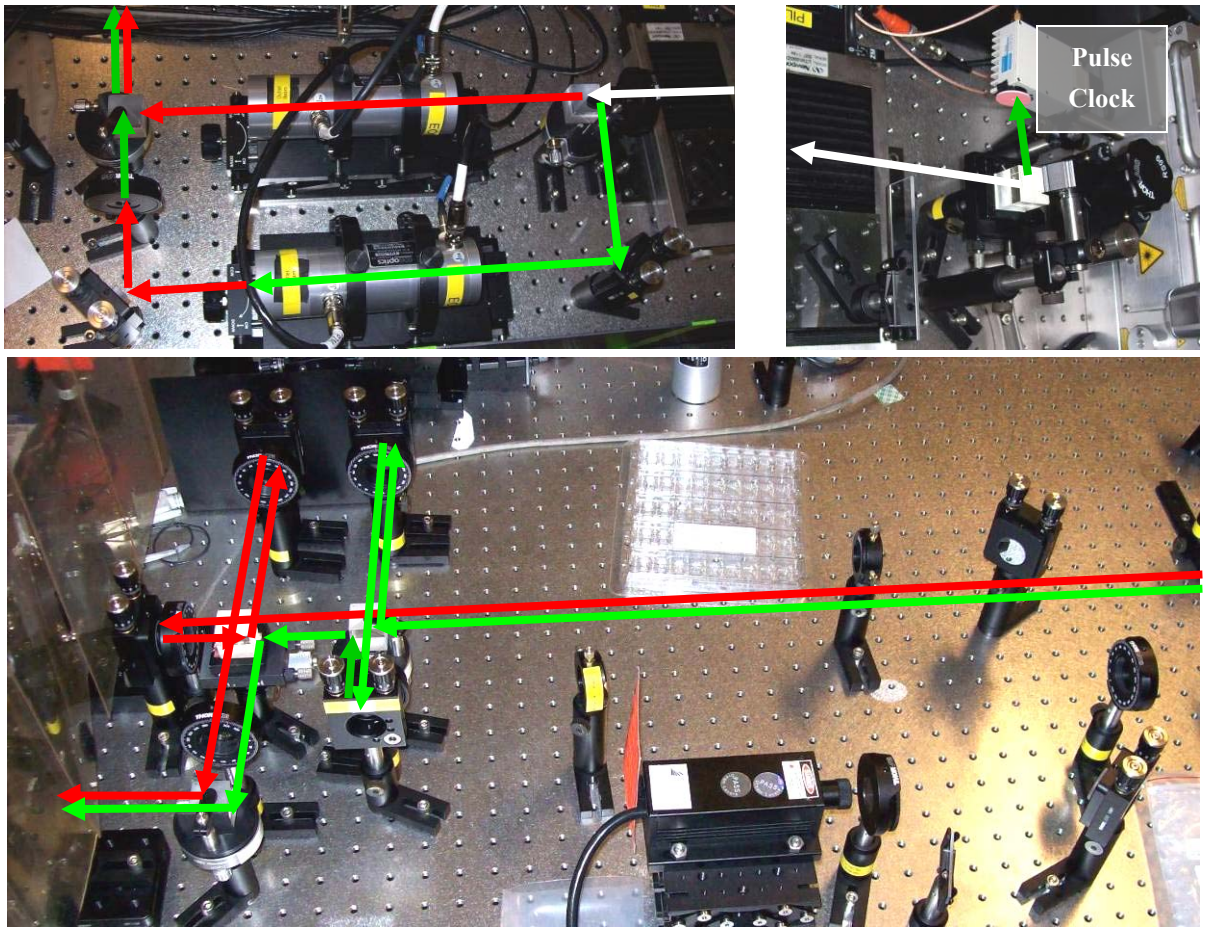

Figure 5.9: Scheme of using two laser beams which are controlled independently by two different modulators.

5.4 Plasmonic Lithography Positioning System

5.4.1 Sources of Error Motions

Sensing and compensating the system's motion errors are important for achieving good pattern definition especially during the high speed lithography process. The major motion errors are from the relative motions between the PL and the prefocusing lens and the relative motions between the PL and the disk. And they are mainly caused by the nonflatness of the disk substrate, windage acting on the head/suspension assembly and the disk, and motion errors of the spindle including both synchronized (or repeatable) motion error and asynchronized (or non-repeatable) motion error. Figure 5.10 shows an illustration of the motion error resources decomposed into

XRZ (off-track, down-track and off-plane) coordinates and some of the motion errors are coupled.

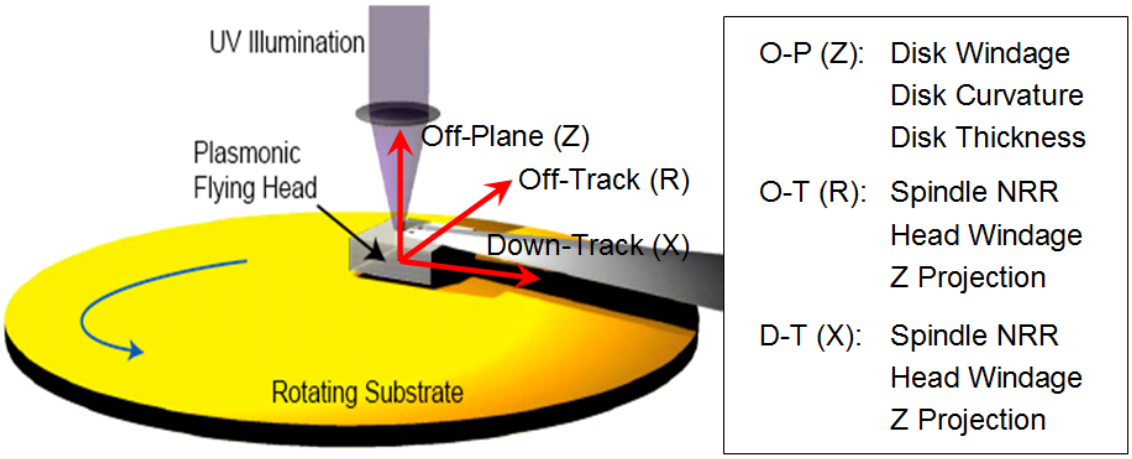

Figure 5.10: Schematic illustration of Precision Rotary-Multi Axis Positioning System (R-MAPS) (left) and definition of movement direction (right).

Figure 5.11 shows an example of typical sources of vibrations and their spectra measured in the head-disk system. For the purpose of PNL, the overall magnitude of motion errors needs to be suppressed well below 10 nm for most of applications.

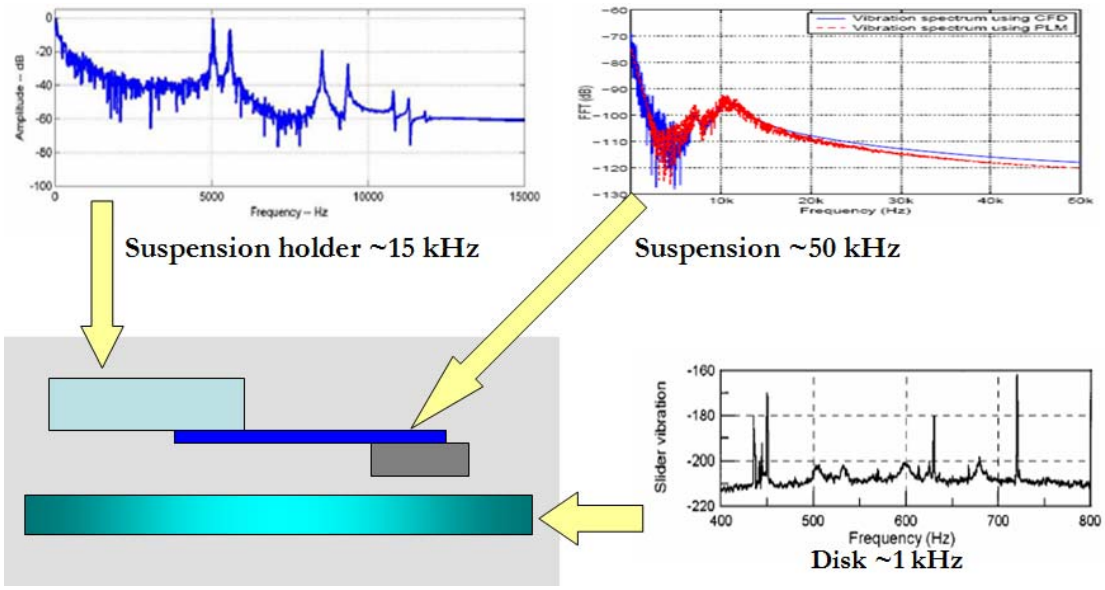

Figure 5.11: Typical sources of vibrations and their spectra in the head-disk system.

5.4.2 Prefocusing Control For Light Delivery

The off-plane motion error is mainly caused by nonflatness of the disk substrate and windage induced disk vibrations, and both of them affect the alignment between the prefocusing lens and the PL in both the Z and XR directions because of its projection components by the suspension arm. The vibrations of the disk can be effectively suppressed to a desirable range by switching to a thicker disk substrate, but the disk nonflatness (both thickness and curvature) are usually uneconomical to manage for a variety of practical reasons. Therefore, a pre-focusing control system is built into the PNL platform to sense and compensate the relative motion between the PL and prefocusing lens.

As illustrated in Figure 5.12, the prefocusing control system uses another CW laser as the light source to sense the position of the PL. A high speed quad photo detector is configured as a position sensitive detector (PSD) to detect the image of the PL. And another high speed quad photo detector works with a set of cylindrical and convex lenses to detect the distance between the PL and the prefocusing lens. Also, a CCD camera is used for acquiring lens images for initial alignment and process monitoring purposes. The prefocusing lens is hosted by a PZT lens actuator and controlled by a Labview real-time system based on the sensing information.

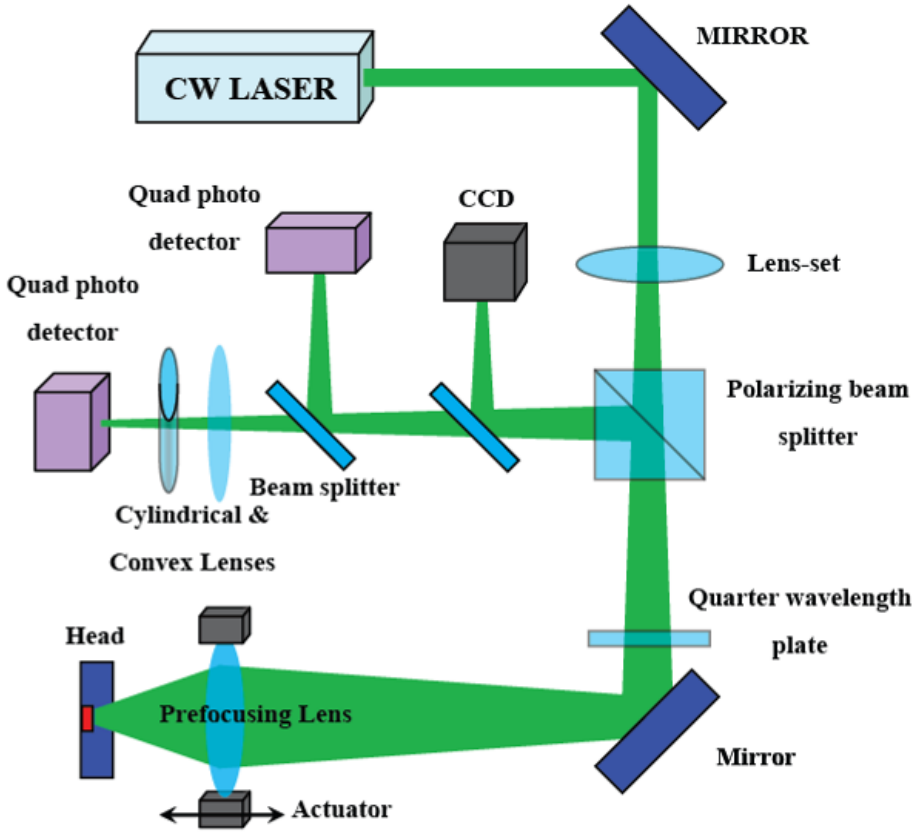

Figure 5.12: Illustration of the prefocusing control system which uses another CW laser as a light

source to sense the in-plane position and distance of the PL, and a PZT lens actuator is used to compensate the motion errors based on the sensing information.

The actuator's dynamic response is measured in the prefocusing system by using a sweep sine as input and capturing the output from quad photo sensors. As shown in Figure 5.13, after loading with the prefocusing lens, the PZT lens actuator behaves as a 2nd order dynamic system with 400 Hz bandwidth, which is large enough to compensate the out-of-plane disk motion errors.

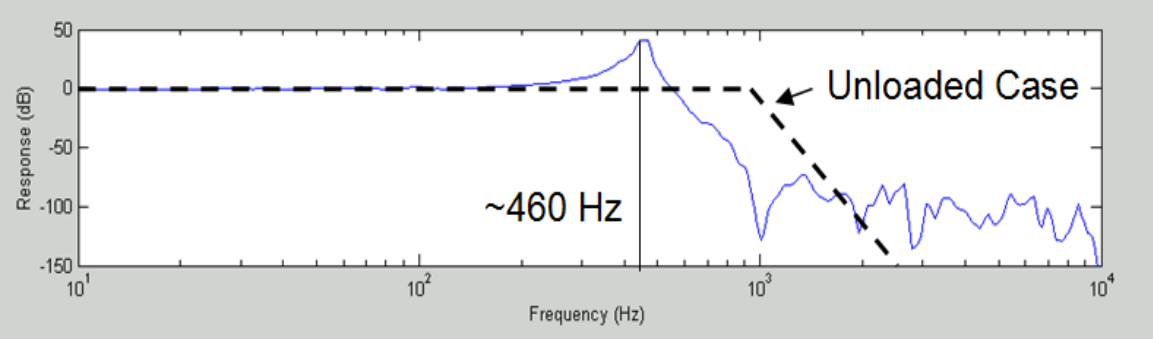

Figure 5.13: Response of prefocusing lens actuator before and after loaded with prefocusing lens.

Figure 5.14(top) shows a typical measurement of a sensor signal power spectrum. In this test, the disk rotated at 2000 rpm corresponding to a base signal frequency at 33.3 Hz. Figure 5.14(bottom) shows the sensor's noise floor where the major noise peaks are mainly from the 60 Hz disturbances and can be further suppressed by improving electrical shielding as needed. As shown in the measurement, the signals are more than three orders stronger than the noise level in terms of magnitude which is accurate enough for our applications.

Real-time controllers were designed and implemented based on a Labview real-time module and C language embedded subroutines. Figure 5.15(left) shows the direct measurement of the disk's motion errors with a peak-to-peak magnitude of 10 μm. Figure 5.15(middle) shows the sub-2 μm peak-to-peak motion error after compensation using a modified PID controller. Figure 5.15(right) shows the sub-1 μm peak-to-peak motion error after compensation using a self-adaptive controller with a noise filter. The achieved control accuracy well meets the process requirements but it can be further improved by using another control algorithm such as feed-forward.

The major in-plane (XR) components of motion errors between the prefocusing lens and PL are caused by the slow drifting of alignment when the head travels over a larger range along the radial (R) direction. They can be easily compensated by low bandwidth in-plane actuators. Figure 5.16 shows a schematic of a prefocusing system as it was integrated with the nanolithography testbed.

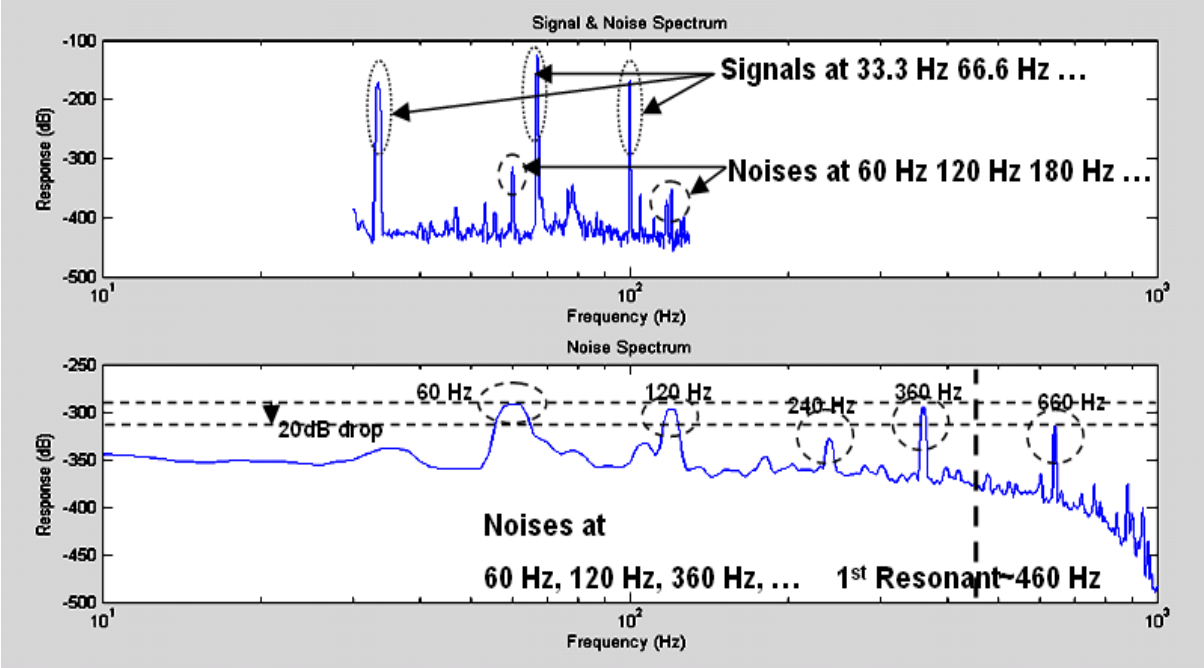

Figure 5.14: A typical measurement of a sensor signal power spectrum (top) and sensor noise floor (bottom) where the major noise peaks are mainly from the 60 Hz disturbances before electrical shielded. The disk rotation speed was 2000 rpm corresponding to a base signal frequency at 33.3 Hz.

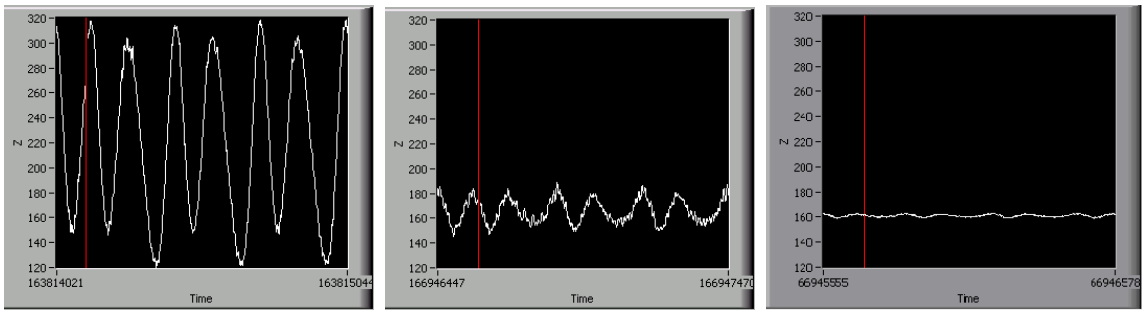

Figure 5.15: Direct measurement of the disk's error motions. (left) Before implementation of the controller the magnitude is about 10 μm peak to peak. (middle) After compensation using a modified PID controller it is reduced to sub-2 μm. (right) Sub-1 μm peak to peak motion error was achieved using a self-adaptive controller with a noise filter.

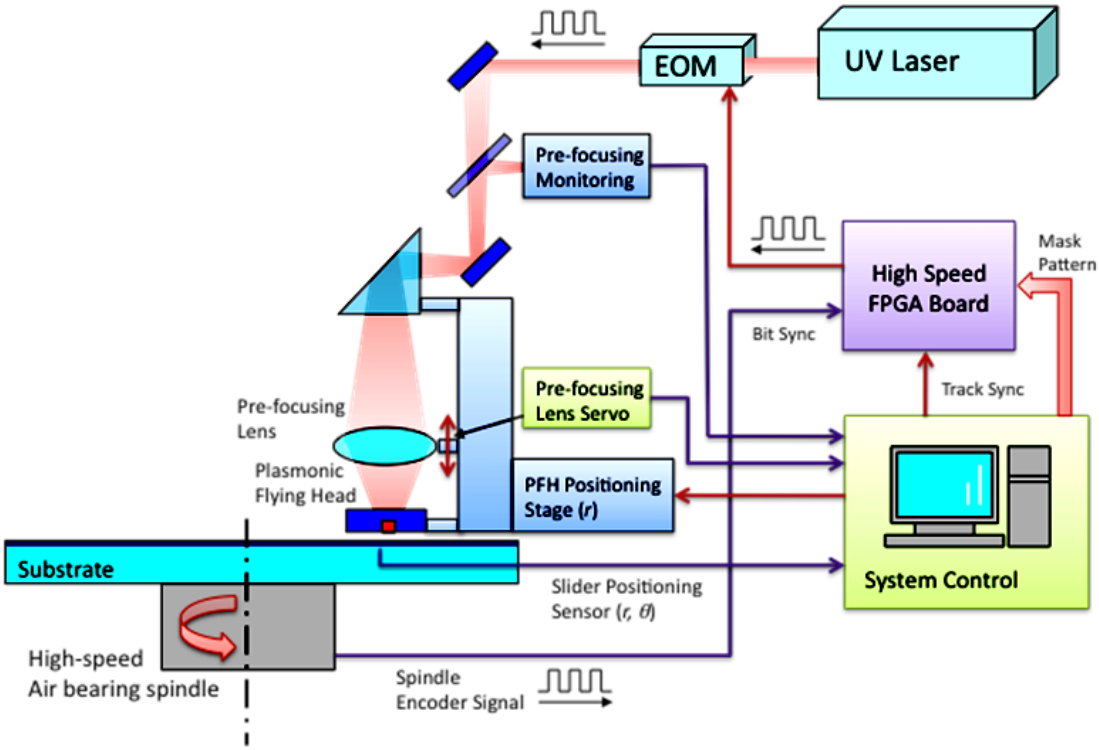

Figure 5.16: Schematic of prefocusing control system

5.4.3 Plasmonic Flying Head Positioning Control

One of the great challenges in PNL is the detection and compensation of relative motion errors between the PL and the disk. Unlike HDDs where the position information is pre-coded into the servo sectors on each side of the disks, currently the PNL approach requires external positioning sensors to detect the relative motion error because of its stringent requirements on pattern stitching accuracy. In order to reach sub-10 nm positioning accuracy in both the radial and circumferential directions, it is desirable to detect the motion errors at sub-1 nm accuracy and sub-100 kHz bandwidth. Figure 5.17 shows one possible sensing scheme (top) and control scheme (bottom) where multiple sensors are employed to detect the motion errors and a head actuator is used to drive the slider/suspension assembly.

Tool implementation for PNL is an ongoing effort within the NSF Center for Scalable and Integrated NanoManufacturing (SINAM) in collaboration with the Center for Precision Metrology at the University of North Carolina Charlotte (UNCC) and the University of California at Los Angeles (UCLA), as shown in Figure 5.18.

Figure 5.19 shows the CAD design of the nano-positioning base stage working next to a high precision spindle with ultra-low none-repeatable runout (NRR).

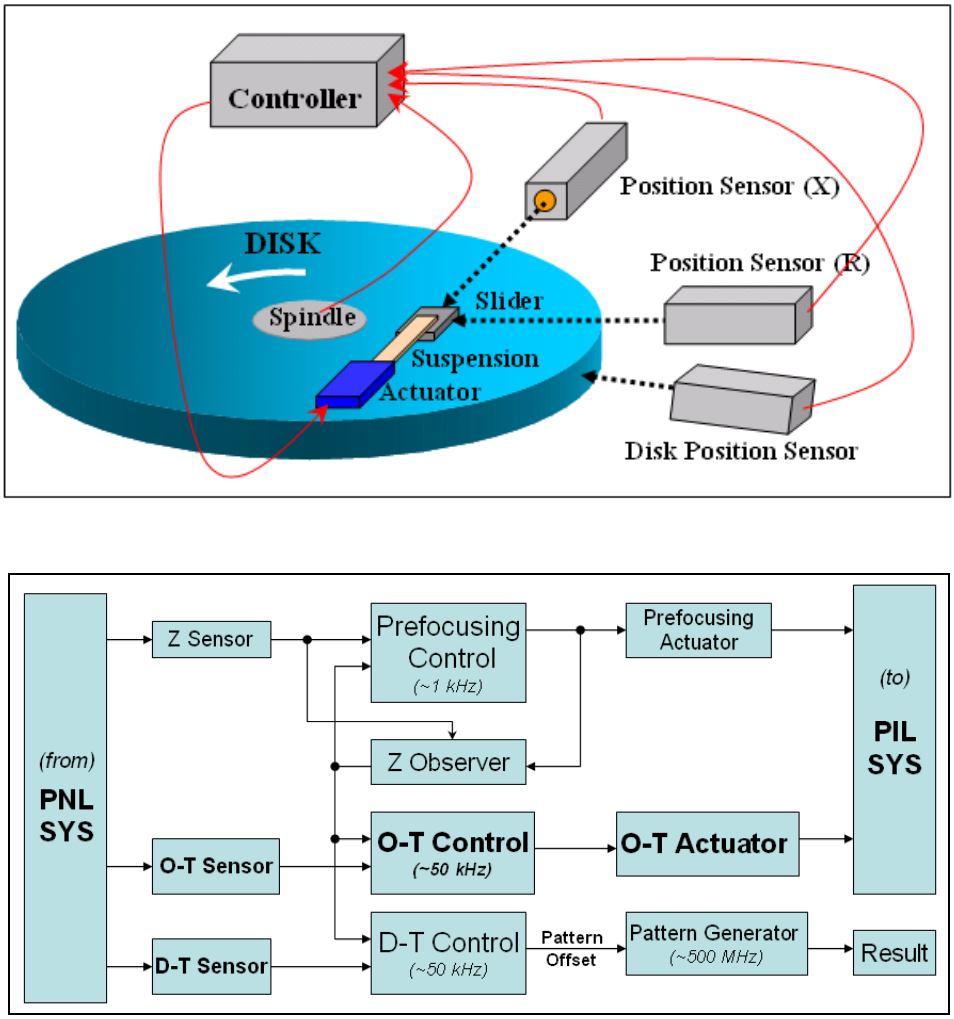

Figure 5.17: One possible sensing scheme (top) and control scheme (bottom), where multiple sensors are employed to detect the motion errors and a head actuator is used to drive the slider/suspension assembly.

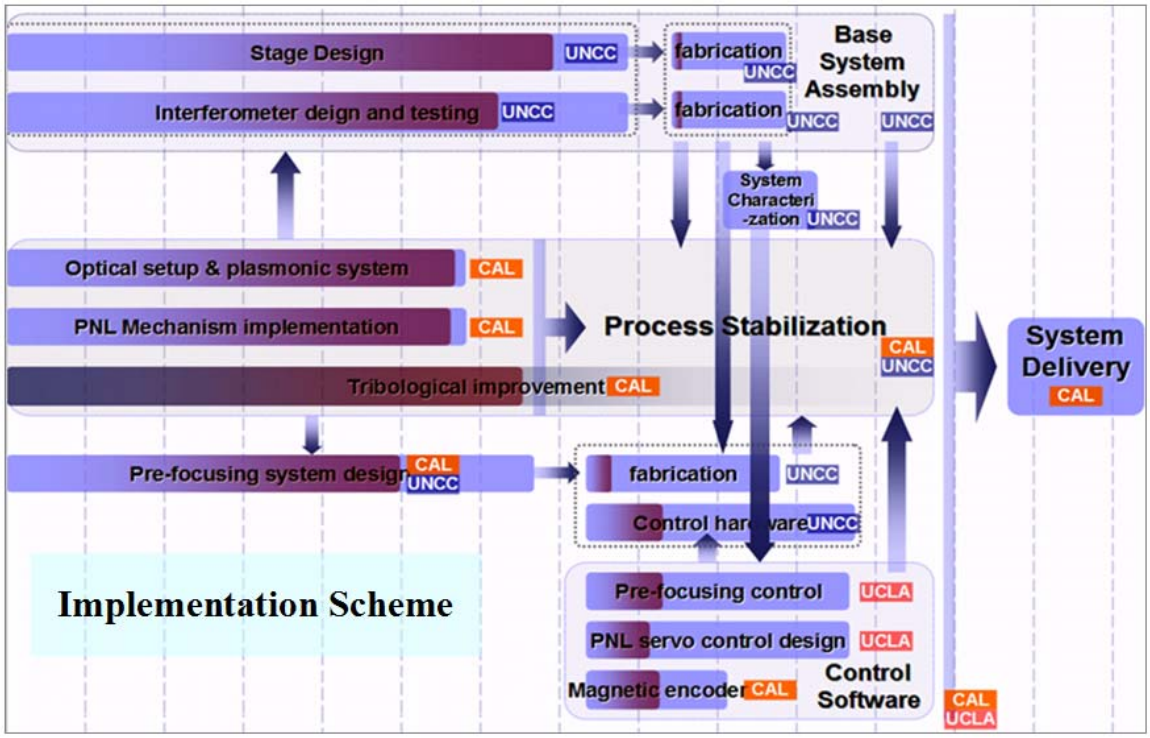

Figure 5.18: Tool implementation for PNL is an ongoing effort in collaborations with other researchers.

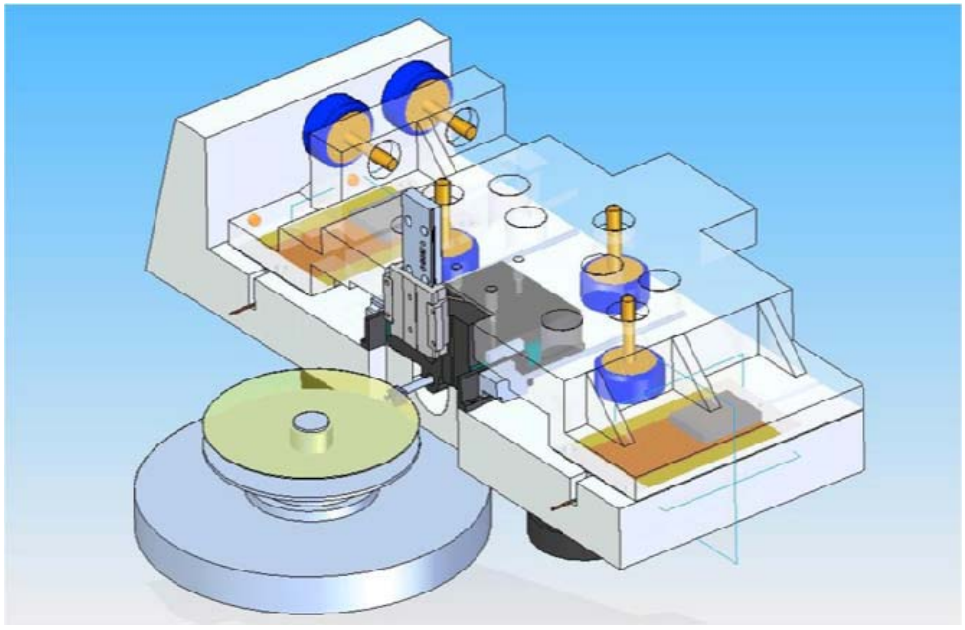

Figure 5.19: CAD design of the nano-positioning base stage working next to a high precision spindle with ultra-low none-repeatable runout (NRR).

The nano-positioning base stage provides a precise radial linear motion (R) in a wafer range and also serves as a carrier for most of positioning sensors and actuators. As an example, Figure 5.20 shows the assembly of the base stage and the prefocusing control module.

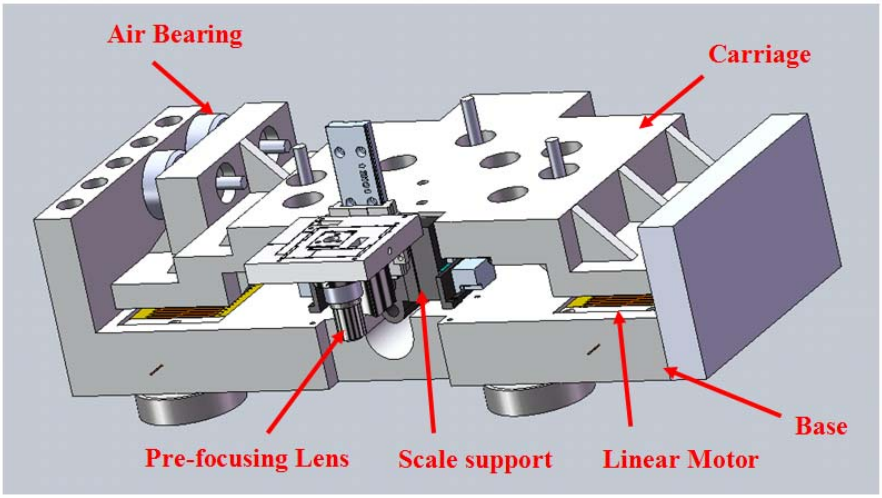

Figure 5.20: Model of the current nano-positioning base stage design

After being integrated with motion error sensors and high speed actuators for the head/suspension assembly, the nano-positioning base stage will provide a controllable motion in all of the out-of-plane (Z), down-track (X), and off-track (R) directions achieving sub-10 nm stitching accuracy.

5.5 CW Laser Assisted FH Control and Resist Pre-heating Module

Inspired by the thermal flying-height control (TFC) method used in current HDDs, we developed the CW laser assisted FH control and resist pre-heating module using the same laser and optics as used in the prefocusing control module. By adjusting the incident CW laser power and size of the laser heating region, we can dynamically regulate the PLs working distance and the size of the protrusion area at the locations of the PLs. In addition, it also locally pre-heats the resist layer through HDI heat conduction to a higher temperature for the purpose of further reducing the exposure dosage of the ultrafast laser and improving process reliability.

Figure 5.21 shows two examples of ANSYS thermal/mechanical simulation results. In these simulations, we used a local laser heating at the power of 300 mW (equivalent to a net heat power of 100 mW) which is calculated from the experimental conditions (a CW laser with output power up to 500 mW at 532 nm, 33% absorption efficiency of 60 nm thick Chromium film, and 70% overall optical efficiency). The left figure shows a peak protrusion of 10 nm with a maximum

temperature rise of 50 K and with a heating spot size around 40 μm. The right figure shows a peak protrusion of 7 nm with a maximum temperature rise of 10 K with a heating spot size around 40 μm. In the extreme case when the focus spot size is reduced to 2 μm, the laser heating will provide a peak temperature rise of 1000 K and a 14-nm peak protrusion where the temperature is too high for our current application. The optimal performance is achieved using ~20 μm heating spot which will provide a peak temperature rise of about 300 K and a protrusion of about 10 nm.

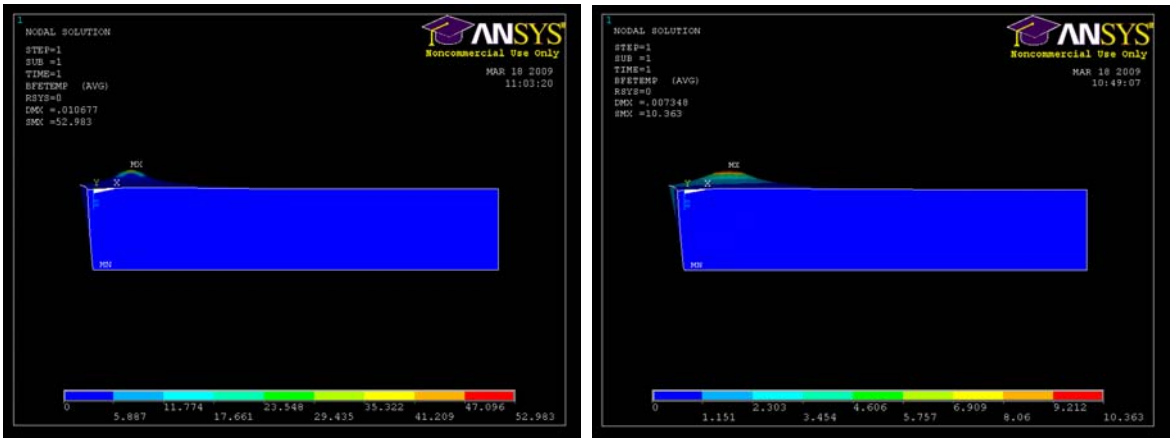

Figure 5.21: Two examples of ANSYS thermal/mechanical simulation results with a local laser heating at the power of 300 mW. The left figure shows a peak protrusion of 10 nm with maximum temperature rise of 50 K with heating spot size around 40 um. And the right figure shows a peak protrusion of 7 nm with a maximum temperature rise of 10 K with a heating spot size around 40 um.

There are two things worth noting regarding the above simulations and this FH regulation scheme. First, the thermal protrusion also affects the flying attitude of the plasmonic flying head due to the push-back force acting on the trailing pad[102], therefore the FH reduction is somewhat smaller than the simulated protrusion. But because the plasmonic flying head features two extraordinarily large trailing pads without highly localized airbearing pressure, the push-back force will only have minor effects on the flying attitude. In experiments, head-to-disk contacts can be observed by the FH monitoring system at a CW laser power around 300 mW, which agrees well with the simulation results. Second, although this thermal protrusion is a local effect compared to the size of the flying head, this scheme is still valid for the parallel patterning process. For example, working with a 20 μm heating laser spot, the protruded area is about 40 μm in diameter within 1 nm variation. When aligned properly with the ABS pitch angle, the heated region can provide enough area for several hundred PLs for parallel patterning which is enough for most high volume manufacturing as discussed previously.

5.6 Summary

In this chapter, we presented the PNL system architecture for high-throughput, high resolution, and good reliability. Many issues including data and pattern management, writing positioning errors and process monitoring were discussed, and solutions were proposed and implemented or are in the process of being implemented in order to improve the system's performance, accuracy, reliability and throughput.

Chapter 6 Results and Discussion

6.1 Continuous Wave (CW) Laser Based PNL Tests

A CW laser based lithography test was performed for the purpose of quick demonstration of the PNL concept. In this test, a 200-mW broadband UV CW laser (Argon laser, Spectra-Physics, operating at ~365 nm UV broadband) beam was focused down to a several micrometer spot onto one of the modified bull's eye PLs in a 4 by 4 lens array, which further focused the beam to a sub-100 nm spot onto the spinning disk for writing of arbitrary patterns (Figure 5.1). The laser pulses are controlled by an electro-optic modulator with timing by signals from a pattern generator. The writing location is determined by the angular position of the disk from the spindle encoder and the position of a high accuracy linear stage along the radial direction. We used the previously introduced TeO_x based thermal resist deposited on a quartz wafer by magnetic sputtering. A high precision airbearing spindle (Stealth 2, Seagull Precision) was used to rotate the wafer at 2,000 rpm which is equivalent to the disk speed of 10 m/s at the outer radius. After pattern writing and development in diluted KOH solution, the exposed patterns were examined using an atomic force microscope. The result demonstrated that we can achieve high-speed patterning with 80 nm linewidth at 10 m/s (Figure 6.1(a)) which is below the size of the far-field diffraction limit. Figure 6.1(b) and (c) show patterning of arrays of the acronym "SINAM" with the feature size of 145 nm.

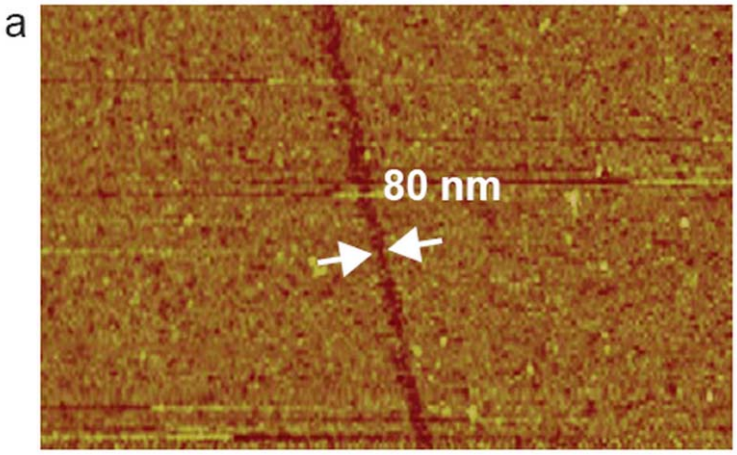

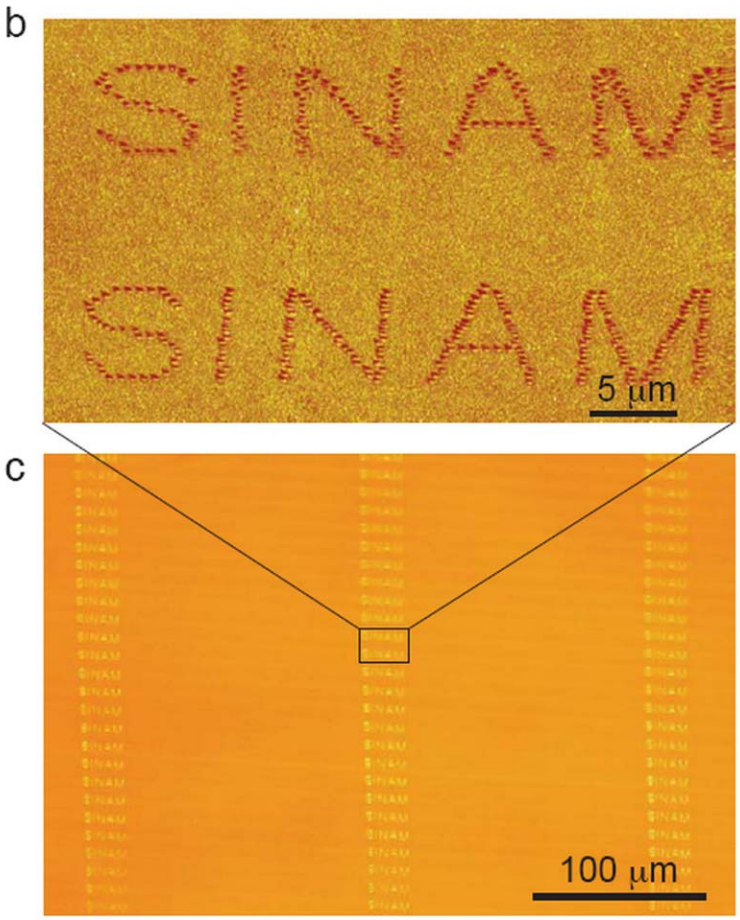

Figure 6.1: Maskless Lithography by flying PLs at near field. (a) AFM image of pattern with 80 nm line width on the TeOx based thermal photoresist. (b) AFM image of arbitrary writing of "SINAM" with 145 nm line width. (c) Optical micrograph of patterning of the large arrays of "SINAM".

In order to achieve even smaller writing linewidths, as shown in the right hand part of Figure 6.2, a dual-spot PL (top-left) was designed for sub-30 nm lines writing. Under a plane wave illumination, this PL produces two hot spots (top-middle), and under off-center illuminations (bottom-left) it produces only one very narrow single elliptical hot spot (bottom-middle) which can be used to writing narrow lines. The right figure shows an AFM image of the achieved lithography result of semi-dashed lines modulated between 20 nm and 30 nm in width and 1 μm in period.

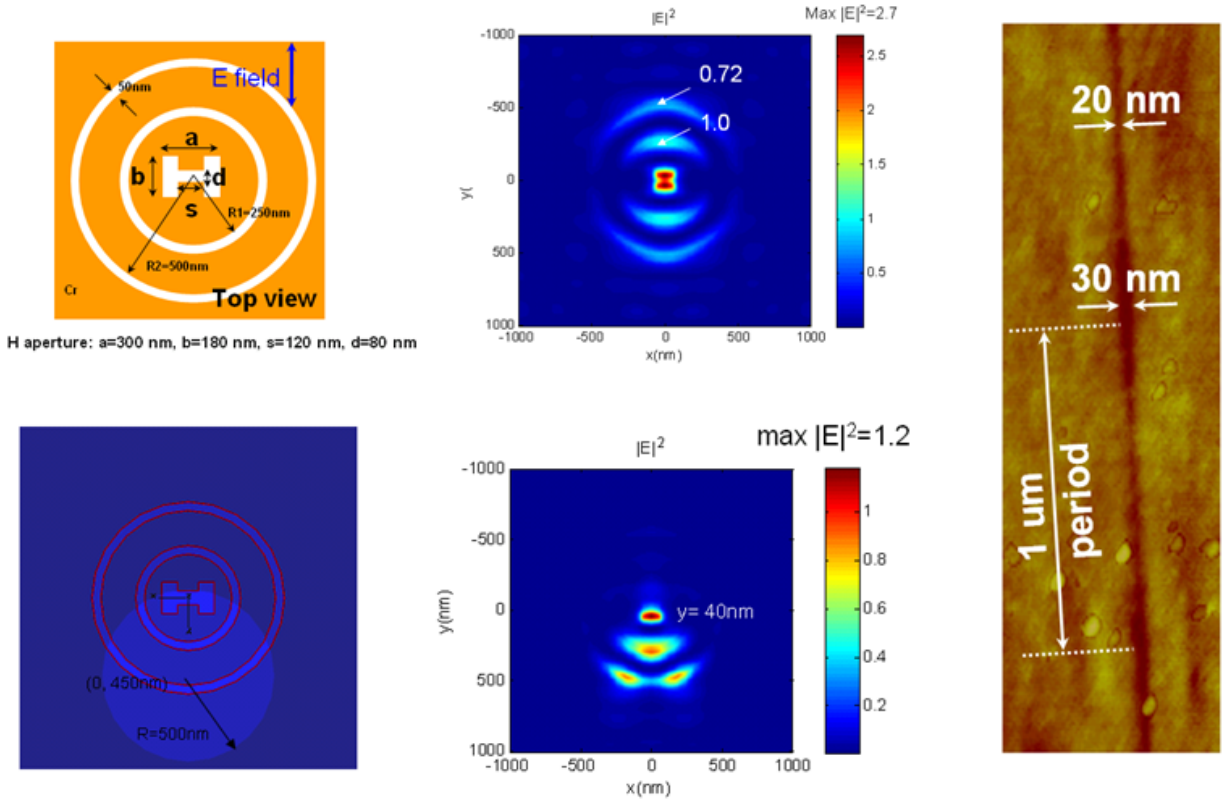

Figure 6.2: A dual-spot PL for sub-30 nm lines writing. Top-left figure shows the lens geometry. Under plane wave illumination, this design produces two hot spots (top-middle) and with off-center illuminations (bottom-left) it produces one very narrow single elliptical hot spot (bottom-middle). The right figure shows the AFM image of the lithography result of semi-dashed lines modulated between 20 nm and 30 nm in width and 1 μm in period.

6.2 Ultrafast Laser Based PNL Tests

In order to fulfill the real-world application needs, as presented in the earlier chapter, a new high-throughput maskless nanolithography system was developed with 22 nm half pitch resolution patterning capability. A 10-mW picosecond pulsed UV laser beam(Vanguard, Spectra-Physics, 355 nm wavelength, 12 ps pulse duration, 80 MHz repetition rate) was used as the exposure light source, to manage the critical laser dose and thermal diffusion in order to achieve good pattern contrast, uniformity and small feature size. During the lithographic process, a spindle was used to rotate the substrate with the resist at 2,500 rpm, corresponding to disk speeds of 4~14 m/s at different radii. The laser pulse train was also probed by an ultrafast photodetector to provide the external clock for the FPGA-based pattern generator for the purpose of improving the pattern stitching accuracy. After the PNL experiment, the exposed patterns were developed in diluted KOH solution and examined using an AFM.

Using the H-shaped PL, we achieved 50 nm wide line writing. Figure 6.3(a) shows the AFM image of a group of 50 nm wide lines with 20 nm depth. And Figure 6.3(b) shows an example of parallel lithography results based on the example scheme illustrated in previous section 5.3.2.

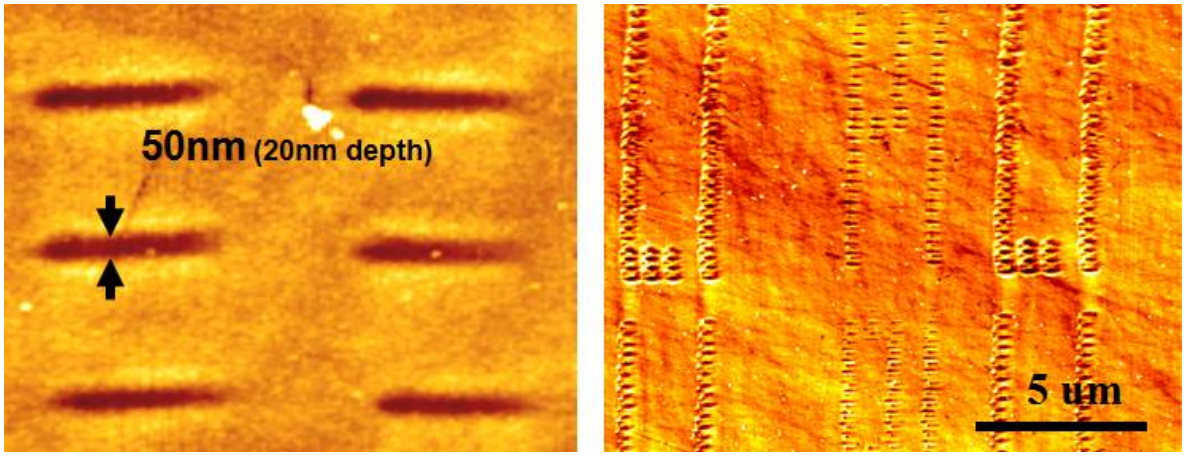

Figure 6.3: AFM images of (left) a group of 50 nm wide lines with 20 nm depth and (right) an example of parallel patterning result.

The performance of the H-shaped PL can be further improved by adding the ring reflector as discussed previously. Figure 6.4(a) shows the AFM image of a typical PNL result of a train of closely patterned dots obtained using the improved PL design with which the resists work at a positive tone. Due to the relatively large radius of the AFM tips, the real pattern edge sharpness and pattern depth cannot be resolved. However, one can determine the pattern's periodicity, which is measured to be 44 nm. The pitch size is in excellent accord with the experimental conditions (at a relative substrate velocity of 3.5 m/s and a laser pulse repetition rate of 80 MHz), thus each dot is generated by a single laser pulse (~100 pJ/pulse). Although there are some dot size variations caused by the finite shutter rising time of the optical modulator and pulse-to-pulse heat accumulation effects, from this result we can conclude that we have indeed successfully achieved ~22 nm half pitch resolution for closely packed dot arrays.

Figure 6.4(b) shows the AFM image of closely patterned dots at 27 nm half pitch using resists working at negative tone. We have also demonstrated line patterning at 30 nm full width at half maximum (FWHM) as shown by the AFM image in Figure 6.4(c). It was written at both higher laser power and higher pattern spatial frequency to allow the dots to merge into continuous lines. It should be noted that pattern edge sharpness can be greatly improved by the optimization of resist exposure threshold and developing conditions.

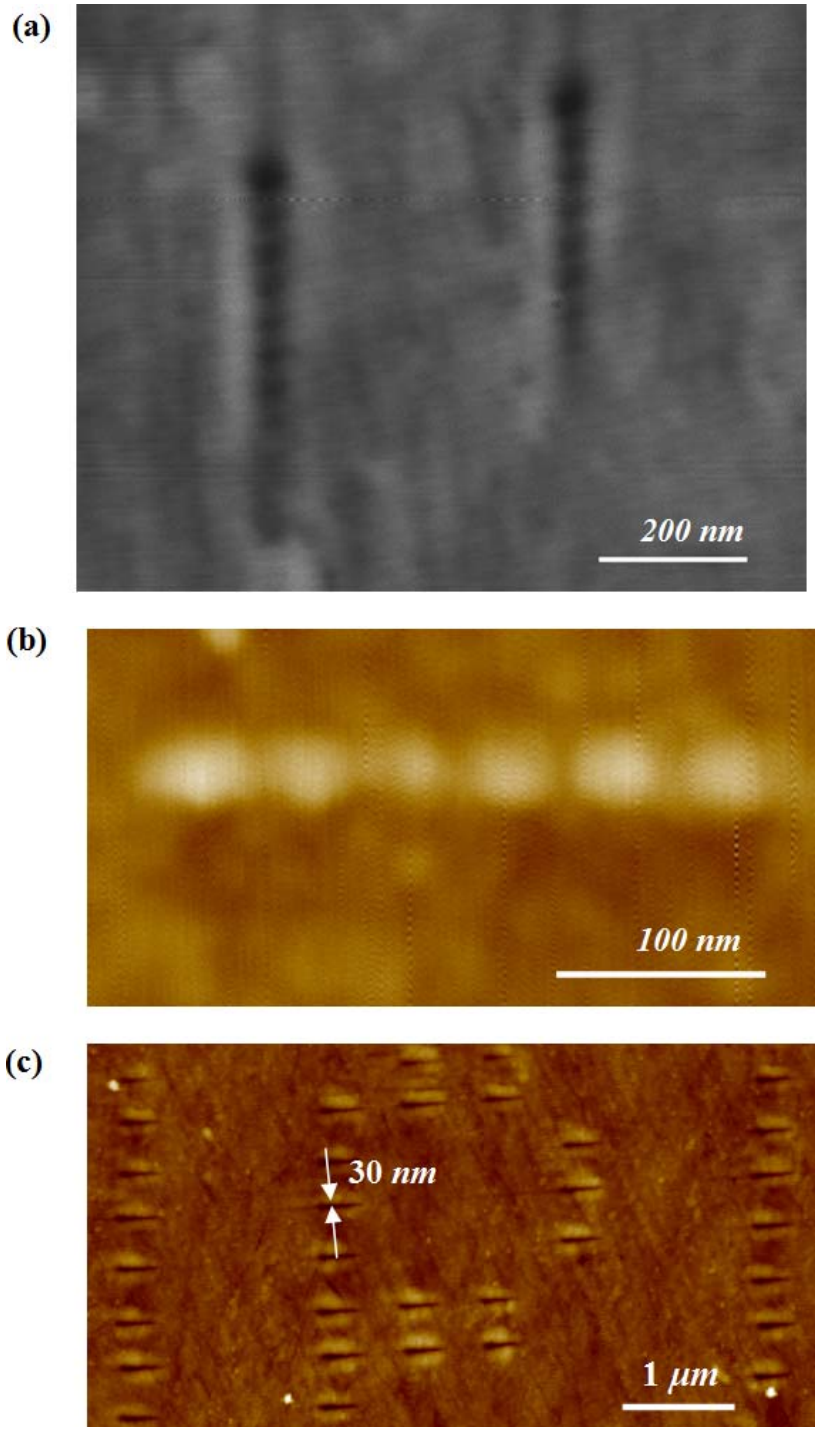

Figure 6.4: PNL results. (a) The AFM image of closely packed dots with a 22 nm half pitch. (b) The AFM image of closely packed dots with 27 nm half pitch size. (c) The AFM image of arbitrary pattern writing at 30 nm linewidth.

6.3 Summary

In summary, we have demonstrated a PNL system which is capable of high-speed patterning with 22 nm half-pitch resolution and 30-nm linewidth patterns. The resolution can be further improved by utilizing shorter SPPs wavelength and guiding mechanisms [59]. Also, the lithography throughput can be dramatically enhanced by increasing the scanning speed and employing a greater number of PLs and flying heads for parallel patterning. Due to the extremely fast scanning, the single PL at speed of 10 m/s already has a much higher throughput than most other maskless lithography approaches. Consider a 16,000 lenses array occupying an area of 800 μm × 20 μm at the bottom of the ABS with each PL of 1 μm in diameter. Taking into account the changes of mean FH, as well as the pitch and roll angles at different linear velocities, our simulation shows that the corresponding FH variation for all the PLs is with the range from 8 to 12 nm, which is well within the acceptable range of the PL working distance. Thus, at the scanning speed at 10 m/s, a plasmonic flying head carrying 16,000 lenses can write a 12" wafer in less than 1 minute. Furthermore, a slider of a few millimeters in size may take up to 10^5 lenses.

Flying PL arrays at optical near field enables a low cost, high-throughput maskless nanoscale fabrication with a few orders of magnitude higher throughput than conventional maskless approaches. It opens a new route towards the next generation lithography (NGL) not only for the electronics industry, but also for the emerging nanotechnology industry. Besides its application in nanolithography, this technique can also be used for nanoscale metrology and imaging. Furthermore, it has strong potential to facilitate the next generation magnetic data storage, known as heat assisted magnetic recording (HAMR) and Bit-Patterned Media (BPM), to achieve two orders higher capacities in the future [128]. In future industrial implementation of this technology, some engineering challenges must be addressed such as pattern data management, lithography linewidth control, pattern overlay and resist defect reduction, which are common for all maskless lithography approaches. Integrated approaches for precision engineering, metrology, as well as new resist development will be needed.

Chapter 7 Summary

This thesis focuses on developing the PNL technique and PNL tool implementation for the next-generation lithography (NGL).

After a brief overview of current nanolithography techniques, the fundamentals of surface plasmons (SPPs) and the status of HDD technology, we presented the use of surface plasmons and advanced airbearing techniques to develop a novel PNL technique. Chapters 2 - 4 presented the key PNL components including PLs, plasmonic flying heads and patterning media. Both numerical and experimental studies were performed to explain their working principles and optimize the designs. Chapter 5 emphasized the development of the maskless PNL system with integration of a flying head with PLs, recording medium and an optical/mechanical/electrical testbed. Chapter 6 presented the PNL results and discussed the potential of this approach. Direct demonstrations of 22 nm half-pitched dot-pattern writing and 30 nm line-pattern writing were presented in this thesis.

Our ultimate goal of this work is to develop a high-throughput PNL system which can generate arbitrary high resolution patterns for high volume manufacturing purposes. Further studies are needed in system optimization and implementation which include higher performance PLs, improving the head-disk interface tribological configuration, exploring the possibility of new resists, and integration of high accuracy motion error sensing and positioning subsystems.

PNL enables agile maskless nanoscale fabrication with the potential to realize a few orders of magnitude greater throughput than conventional maskless lithography techniques. It is a low-cost, high-throughput maskless nanolithography approach for the NGL and also for the emerging nanotechnology applications, nanoscale metrology and imaging. Its strong potential can also facilitate the next generation magnetic data storage, known as heat assisted magnetic recording (HAMR) and Bit-Patterned Media (BPM), to achieve a few orders higher capacities in HDDs in the future. Such a low-cost, high-throughput scheme promises a new route towards the next generation nano-manufacturing.

Bibliography

1. Okazaki, S., *RESOLUTION LIMITS OF OPTICAL LITHOGRAPHY.* Journal of Vacuum Science & Technology B, 1991. **9**(6): p. 2829-2833.
2. Jeong, H.J., et al., *THE FUTURE OF OPTICAL LITHOGRAPHY.* Solid State Technology, 1994. **37**(4): p. 39-&.
3. Gwyn, C.W., et al., *Extreme ultraviolet lithography.* Journal of Vacuum Science & Technology B, 1998. **16**(6): p. 3142-3149.
4. Service, R.F., *EUV lithography - Optical lithography goes to extremes - And beyond.* Science, 2001. **293**(5531): p. 785-786.
5. Fay, B., *Advanced optical lithography development, from UV to EUV.* Microelectronic Engineering, 2002. **61-2**: p. 11-24.
6. Solak, H.H., et al., *Sub-50 nm period patterns with EUV interference lithography.* Microelectronic Engineering, 2003. **67-8**: p. 56-62.
7. Chang, S.W., et al., *Sub-50 nm feature sizes using positive tone molecular glass resists for EUV lithography.* Journal of Materials Chemistry, 2006. **16**(15): p. 1470-1474.
8. Kemp, K. and S. Wurm, *EUV lithography.* Comptes Rendus Physique, 2006. **7**(8): p. 875-886.
9. Ekinci, Y., et al., *20 nm Line/space patterns in HSQ fabricated by EUV interference lithography.* Microelectronic Engineering, 2007. **84**(5-8): p. 700-704.
10. Goethals, A.M., et al., *Status of EUV lithography at IMEC.* Journal of Photopolymer Science and Technology, 2007. **20**(3): p. 383-392.
11. Thackeray, J.W., et al., *Pathway to sub-30nm resolution in EUV lithography.* Journal of Photopolymer Science and Technology, 2007. **20**(3): p. 411-418.
12. Vladimirsky, Y., *Next generation lithography (NGL) concept application in X-ray lithography.* Proceedings of the SPIE - The International Society for Optical Engineering, 2000. **3997**: p. 478-482.
13. Early, K., M.L. Schattenburg, and H.I. Smith, *Absence of resolution degradation in X-ray lithography for lambda from 4.5 nm to 0.83 nm.* Microelectronic Engineering, 1990. **11**(1-4): p. 317-321.
14. Liddle, J.A., et al., *The SCattering with angular limitation in projection electron-beam lithography (SCALPEL) system.* Japanese Journal of Applied Physics Part 1-Regular Papers Short Notes & Review Papers, 1995. **34**(12B): p. 6663-6671.
15. Liddle, J.A., et al., *MASK FABRICATION FOR PROJECTION ELECTRON-BEAM LITHOGRAPHY INCORPORATING THE SCALPEL TECHNIQUE.* Journal of Vacuum Science & Technology B, 1991. **9**(6): p. 3000-3004.
16. Mkrtchyan, M.M., *Electron scattering and related phenomena in scattering with angular limitation projection electron lithography (SCALPEL*).* Japanese Journal of Applied Physics Part 1-Regular Papers Short Notes & Review Papers, 2000. **39**(12B): p.

6881-6896.
17. Mkrtchyan, M.M., et al., *Electron scattering and transmission through SCALPEL masks.* Journal of Vacuum Science & Technology B, 1998. **16**(6): p. 3385-3391.
18. Semke, W.H., et al., *Dynamic analysis of a SCALPEL mask during electron-beam exposure.* Journal of Vacuum Science & Technology B, 1998. **16**(6): p. 3587-3591.
19. Cramer, G., I.L. Hsin, and A. Zakhor, *Lossless Compression Algorithm for REBL Direct-Write E-Beam Lithography System.* Proceedings of the SPIE - The International Society for Optical Engineering, 2010. **7637**: p. 76371L (15 pp.)-76371L (15 pp.).
20. Petric, P., et al., *REBL nanowriter: reflective electron beam lithography.* Proceedings of the SPIE - The International Society for Optical Engineering, 2009. **7271**: p. 727107 (15 pp.)-727107 (15 pp.).
21. Petric, P., et al., *REBL: A novel approach to high speed maskless electron beam direct write lithography.* Journal of Vacuum Science & Technology B, 2009. **27**(1): p. 161-166.
22. Bartelt, J.L., et al., *MASKED ION-BEAM LITHOGRAPHY - A FEASIBILITY DEMONSTRATION FOR SUBMICROMETER DEVICE FABRICATION.* Journal of Vacuum Science & Technology, 1981. **19**(4): p. 1166-1171.
23. Platzgummer, E., *Maskless Lithography and Nanopatterning with Electron and Ion Multi-Beam Projection.* Proceedings of the SPIE - The International Society for Optical Engineering, 2010. **7637**: p. 763703 (12 pp.)-763703 (12 pp.).
24. Chou, S.Y., C. Keimel, and J. Gu, *Ultrafast and direct imprint of nanostructures in silicon.* Nature, 2002. **417**(6891): p. 835-837.
25. Chou, S.Y., P.R. Krauss, and P.J. Renstrom, *Imprint lithography with 25-nanometer resolution.* Science, 1996. **272**(5258): p. 85-87.
26. Chou, S.Y., P.R. Krauss, and P.J. Renstrom, *Nanoimprint lithography.* Journal of Vacuum Science & Technology B, 1996. **14**(6): p. 4129-4133.
27. Chou, S.Y., et al., *Sub-10 nm imprint lithography and applications.* Journal of Vacuum Science & Technology B, 1997. **15**(6): p. 2897-2904.
28. Gates, B.D., et al., *New approaches to nanofabrication: Molding, printing, and other techniques.* Chemical Reviews, 2005. **105**(4): p. 1171-1196.
29. Michel, B., et al., *Printing meets lithography: Soft approaches to high-resolution printing.* Ibm Journal of Research and Development, 2001. **45**(5): p. 697-719.
30. Xia, Y.N. and G.M. Whitesides, *Soft lithography.* Annual Review of Materials Science, 1998. **28**: p. 153-184.
31. Pease, R.F., *Maskless lithography.* Microelectronic Engineering, 2005. **78-79**: p. 381-392.
32. McCord, M.A., *Electron beam lithography for 0.13 mu m manufacturing.* Journal of Vacuum Science & Technology B, 1997. **15**(6): p. 2125-2129.
33. Melngailis, J., *FOCUSED ION-BEAM TECHNOLOGY AND APPLICATIONS.* Journal of Vacuum Science & Technology B, 1987. **5**(2): p. 469-495.
34. Piner, R.D., et al., *"Dip-pen" nanolithography.* Science, 1999. **283**(5402): p. 661-663.
35. Salaita, K., et al., *Massively parallel dip-pen nanolithography with 55000-pen two-dimensional arrays.* Angewandte Chemie-International Edition, 2006. **45**(43): p.

7220-7223.
36. Vettiger, P., et al., *The "Millipede" - More than one thousand tips for future AFM data storage.* Ibm Journal of Research and Development, 2000. **44**(3): p. 323-340.
37. Cooper, E.B., et al., *Terabit-per-square-inch data storage with the atomic force microscope.* Applied Physics Letters, 1999. **75**(22): p. 3566-3568.
38. Muraki, M. and S. Gotoh, *New concept for high-throughput multielectron beam direct write system.* Journal of Vacuum Science & Technology B, 2000. **18**(6): p. 3061-3066.
39. Pease, R.F., et al., *Prospects for charged particle lithography as a manufacturing technology.* Microelectronic Engineering, 2000. **53**(1-4): p. 55-60.
40. Groves, T.R. and R.A. Kendall, *Distributed, multiple variable shaped electron beam column for high throughput maskless lithography.* Journal of Vacuum Science & Technology B, 1998. **16**(6): p. 3168-3173.
41. Kampherbeek, B.J., et al., *An experimental setup to test the MAPPER electron lithography concept.* Microelectronic Engineering, 2000. **53**(1-4): p. 279-282.
42. Carter, D.J.D., et al., *Zone-plate array lithography (ZPAL): a new maskless approach.* Proceedings of the SPIE - The International Society for Optical Engineering, 1999. **3676**: p. 324-332.
43. Carter, D.J.D., et al., *Maskless, parallel patterning with zone-plate array lithography.* Journal of Vacuum Science & Technology B, 1999. **17**(6): p. 3449-3452.
44. Carter, D.J.D., et al. *Maskless nanolithography with diffractive optics: zone-plate-array lithography (ZPAL)*. in *Trends in Optics and Photonics. Diffractive Optics and Micro-Optics. Vol.41. Technical Digest. Postconference Edition*. 2000. Quebec City, Que., Canada: Opt. Soc. America.
45. Chao, D., et al., *Immersion zone-plate-array lithography.* Journal of Vacuum Science & Technology B, 2005. **23**(6): p. 2657-2661.
46. Djomehri, I.J., T.A. Savas, and H.I. Smith, *Zone-plate-array lithography in the deep ultraviolet.* Journal of Vacuum Science & Technology B, 1998. **16**(6): p. 3426-3429.
47. Menon, R., et al., *Zone-plate-array lithography (ZPAL): simulations for system design.* AIP Conference Proceedings, 2000(507): p. 647-652.
48. Smith, H.I., et al., *Zone-plate-array lithography: A low-cost complement or competitor to scanning-electron-beam lithography.* Microelectronic Engineering, 2006. **83**(4-9): p. 956-961.
49. Ouk Kim, S., et al., *Epitaxial self-assembly of block copolymers on lithographically defined nanopatterned substrates.* Nature, 2003. **424**(6947): p. 411-414.
50. Ruiz, R., et al., *Density multiplication and improved lithography by directed block copolymer assembly.* Science, 2008. **321**(5891): p. 936-939.
51. Stoykovich, M.P., et al., *Directed assembly of block copolymer blends into nonregular device-oriented structures.* Science, 2005. **308**(5727): p. 1442-1446.
52. Park, S., et al., *Macroscopic 10-Terabit-per-Square- Inch Arrays from Block Copolymers with Lateral Order.* Science, 2009. **323**(5917): p. 1030-1033.
53. Genet, C. and T.W. Ebbesen, *Light in tiny holes.* Nature, 2007. **445**(7123): p. 39-46.

54. Ozbay, E., *Plasmonics: Merging photonics and electronics at nanoscale dimensions.* Science, 2006. **311**(5758): p. 189-193.
55. Ritchie, R.H., *PLASMA LOSSES BY FAST ELECTRONS IN THIN FILMS.* Physical Review, 1957. **106**(5): p. 874-881.
56. Fang, N., et al., *Sub-diffraction-limited optical imaging with a silver superlens.* Science, 2005. **308**(5721): p. 534-537.
57. Liu, Z.W., et al., *Focusing surface plasmons with a plasmonic lens.* Nano Letters, 2005. **5**(9): p. 1726-1729.
58. Srituravanich, W., et al., *Plasmonic nanolithography.* Nano Letters, 2004. **4**(6): p. 1085-1088.
59. Stockman, M.I., *Nanofocusing of optical energy in tapered plasmonic waveguides.* Physical Review Letters, 2004. **93**(13).
60. Hecht, B., et al., *Facts and artifacts in near-field optical microscopy.* Journal of Applied Physics, 1997. **81**(6): p. 2492-2498.
61. Hoffmann, P., B. Dutoit, and R.P. Salathe, *Comparison of mechanically drawn and protection layer chemically etched optical fiber tips.* Ultramicroscopy, 1995. **61**(1-4): p. 165-170.
62. Lazarev, A., et al., *Formation of fine near-field scanning optical microscopy tips. Part I. By static and dynamic chemical etching.* Review of Scientific Instruments, 2003. **74**(8): p. 3679-3683.
63. Shalom, S., et al., *A MICROPIPETTE FORCE PROBE SUITABLE FOR NEAR-FIELD SCANNING OPTICAL MICROSCOPY.* Review of Scientific Instruments, 1992. **63**(9): p. 4061-4065.
64. Barnes, W.L., A. Dereux, and T.W. Ebbesen, *Surface plasmon subwavelength optics.* Nature, 2003. **424**(6950): p. 824-830.
65. Dogariu, A., et al., *Optical pulse propagation through metallic nano-apertures.* Applied Physics B-Lasers and Optics, 2002. **74**: p. S69-S73.
66. Ebbesen, T.W., et al., *Extraordinary optical transmission through sub-wavelength hole arrays.* Nature, 1998. **391**(6668): p. 667-669.
67. Salomon, L., et al., *Near-field distribution of optical transmission of periodic subwavelength holes in a metal film.* Physical Review Letters, 2001. **86**(6): p. 1110-1113.
68. Thio, T., et al., *Surface-plasmon-enhanced transmission through hole arrays in Cr films.* Journal of the Optical Society of America B-Optical Physics, 1999. **16**(10): p. 1743-1748.
69. Raether, H., *surface plasmons on smooth and rough surfaces and on gratings*. 1988: Springer. 136.
70. Wang, Y., et al., *Plasmonic nearfield scanning probe with high transmission.* Nano Letters, 2008. **8**(9): p. 3041-3045.
71. Challener, W.A., et al., *Heat-assisted magnetic recording by a near-field transducer with efficient optical energy transfer.* Nature Photonics, 2009. **3**(4): p. 220-224.
72. Kryder, M.H., et al., *Heat Assisted Magnetic Recording.* Proceedings of the Ieee, 2008. **96**(11): p. 1810-1835.

73. Rottmayer, R.E., et al., *Heat-assisted magnetic recording.* Ieee Transactions on Magnetics, 2006. **42**(10): p. 2417-2421.
74. Kikitsu, A., *Prospects for bit patterned media for high-density magnetic recording.* Journal of Magnetism and Magnetic Materials, 2009. **321**(6): p. 526-530.
75. Litvinov, D., et al., *Recording physics, design considerations, and fabrication of nanoscale bit-patterned media.* Ieee Transactions on Nanotechnology, 2008. **7**(4): p. 463-476.
76. Richter, H.J., et al., *Recording on bit-patterned media at densities of 1 Tb/in(2) and beyond.* Ieee Transactions on Magnetics, 2006. **42**(10): p. 2255-2260.
77. Richter, H.J., et al., *Recording potential of bit-patterned media.* Applied Physics Letters, 2006. **88**(22).
78. Yang, X., et al., *Challenges in 1 Teradot/in.(2) dot patterning using electron beam lithography for bit-patterned media.* Journal of Vacuum Science & Technology B, 2007. **25**(6): p. 2202-2209.
79. Valaskovic, G.A., M. Holton, and G.H. Morrison, *PARAMETER CONTROL, CHARACTERIZATION, AND OPTIMIZATION IN THE FABRICATION OF OPTICAL-FIBER NEAR-FIELD PROBES.* Applied Optics, 1995. **34**(7): p. 1215-1228.
80. Ash, E.A. and G. Nicholls, *SUPER-RESOLUTION APERTURE SCANNING MICROSCOPE.* Nature, 1972. **237**(5357): p. 510-&.
81. Durig, U., D.W. Pohl, and F. Rohner, *NEAR-FIELD OPTICAL-SCANNING MICROSCOPY.* Journal of Applied Physics, 1986. **59**(10): p. 3318-3327.
82. Leviatan, Y., *STUDY OF NEAR-ZONE FIELDS OF A SMALL APERTURE.* Journal of Applied Physics, 1986. **60**(5): p. 1577-1583.
83. Pohl, D.W., W. Denk, and M. Lanz, *OPTICAL STETHOSCOPY - IMAGE RECORDING WITH RESOLUTION LAMBDA/20.* Applied Physics Letters, 1984. **44**(7): p. 651-653.
84. Synge, E.H., *A suggested method for extending microscopic resolution into the ultra-microscopic region.* Philosophical Magazine, 1928. **6**(35): p. 356-362.
85. Lezec, H.J., et al., *Beaming light from a subwavelength aperture.* Science, 2002. **297**(5582): p. 820-822.
86. Thio, T., et al., *Enhanced light transmission through a single subwavelength aperture.* Optics Letters, 2001. **26**(24): p. 1972-1974.
87. Betzig, E., et al., *BREAKING THE DIFFRACTION BARRIER - OPTICAL MICROSCOPY ON A NANOMETRIC SCALE.* Science, 1991. **251**(5000): p. 1468-1470.
88. Betzig, E., et al., *NEAR-FIELD MAGNETOOPTICS AND HIGH-DENSITY DATA-STORAGE.* Applied Physics Letters, 1992. **61**(2): p. 142-144.
89. Jin, E.X. and X.F. Xu, *Enhanced optical near field from a bowtie aperture.* Applied Physics Letters, 2006. **88**(15).
90. Sendur, K. and W. Challener, *Near-field radiation of bow-tie antennas and apertures at optical frequencies.* Journal of Microscopy-Oxford, 2003. **210**: p. 279-283.
91. Sundaramurthy, A., et al., *Field enhancement and gap-dependent resonance in a system of two opposing tip-to-tip Au nanotriangles.* Physical Review B, 2005. **72**(16).

92. Sundaramurthy, A., et al., *Toward nanometer-scale optical photolithography: Utilizing the near-field of bowtie optical nanoantennas.* Nano Letters, 2006. **6**(3): p. 355-360.
93. Xu, J.Y., et al., *Design tips of nanoapertures with strong field enhancement and proposal of novel L-shaped aperture.* Optical Engineering, 2005. **44**(1).
94. Matsumoto, T., et al., *Writing 40 nm marks by using a beaked metallic plate near-field optical probe.* Optics Letters, 2006. **31**(2): p. 259-261.
95. Matsumoto, T., et al., *Highly efficient probe with a wedge-shaped metallic plate for high density near-field optical recording.* Journal of Applied Physics, 2004. **95**(8): p. 3901-3906.
96. Srituravanich, W., et al., *Flying plasmonic lens in the near field for high-speed nanolithography.* Nature Nanotechnology, 2008. **3**(12): p. 733-737.
97. Yin, L.L., et al., *Subwavelength focusing and guiding of surface plasmons.* Nano Letters, 2005. **5**(7): p. 1399-1402.
98. Itagi, A.V., et al., *Ridge waveguide as a near-field optical source.* Applied Physics Letters, 2003. **83**(22): p. 4474-4476.
99. Sendur, K., C. Peng, and W. Challener, *Near-field radiation from a ridge waveguide transducer in the vicinity of a solid immersion lens.* Physical Review Letters, 2005. **94**(4).
100. Shi, X.L. and L. Hesselink, *Mechanisms for enhancing power throughput from planar nano-apertures for near-field optical data storage.* Japanese Journal of Applied Physics Part 1-Regular Papers Short Notes & Review Papers, 2002. **41**(3B): p. 1632-1635.
101. Bogy, D.B., et al., *Some advanced air-bearing design issues for proximity recording.* Journal of Tribology-Transactions of the Asme, 1998. **120**(3): p. 566-570.
102. Juang, J.Y. and D.B. Bogy, *Nanotechnology advances and applications in information storage.* Microsystem Technologies-Micro-and Nanosystems-Information Storage and Processing Systems, 2005. **11**(8-10): p. 950-957.
103. Juang, J.Y. and D.B. Bogy, *Air-bearing effects on actuated thermal pole-tip protrusion for hard disk drives.* Journal of Tribology-Transactions of the Asme, 2007. **129**(3): p. 570-578.
104. Juang, J.Y., D.B. Bogy, and C.S. Bhatia, *Design and dynamics of flying height control slider with piezoelectric nanoactuator in hard disk drives.* Journal of Tribology-Transactions of the Asme, 2007. **129**(1): p. 161-170.
105. Juang, J.Y., D. Chen, and D.B. Bogy, *Alternate air bearing slider designs for areal density of 1 Tb/in(2).* Ieee Transactions on Magnetics, 2006. **42**(2): p. 241-246.
106. Lu, S., et al., *Air bearing design, optimization, stability analysis and verification for sub-25nm flying.* Ieee Transactions on Magnetics, 1996. **32**(1): p. 103-109.
107. Lu, S., et al., *DESIGN, SIMULATION, FABRICATION AND MEASUREMENT OF A 25-NM, 50-PERCENT SLIDER.* Ieee Transactions on Magnetics, 1995. **31**(6): p. 2952-2954.
108. Hirata, M., et al., *Near-field optical flying head with protruding aperture and its fabrication.* Japanese Journal of Applied Physics Part 1-Regular Papers Short Notes & Review Papers, 2005. **44**(5B): p. 3519-3523.

109. Hirota, T., et al., *Air-bearing design and flying characteristics of flexible optical head slider combined with visible laser light guide.* Microsystem Technologies, 2002. **8**(2-3): p. 155-160.
110. Hsiao, C.C., T.S. Liu, and S.H. Chien, *Adaptive inverse control for the pickup head flying height of near-field optical disk drives.* Smart Materials & Structures, 2006. **15**(6): p. 1632-1640.
111. Kawasaki, G., et al., *Development of an optical flying head for a next-generation magneto-optical recording system.* Microsystem Technologies-Micro-and Nanosystems-Information Storage and Processing Systems, 2005. **11**(8-10): p. 1081-1084.
112. Kim, D.E., et al., *Development of flying type head/slider for optical recording technology.* Tribology International, 2005. **38**(6-7): p. 578-587.
113. Kim, J.H., *Head-disk interface problems in first-surface near-field optical recording with flying optical head.* Current Applied Physics, 2008. **8**(5): p. 577-582.
114. Kim, S., et al., *Effective design and performance of an optical flying head for near-field recording.* Japanese Journal of Applied Physics Part 1-Regular Papers Short Notes & Review Papers, 2002. **41**(3B): p. 1884-1888.
115. Kim, S., et al., *An optical flying head assembly for a small-form-factor plastic disk in PCMCIA-like drive.* Japanese Journal of Applied Physics Part 1-Regular Papers Short Notes & Review Papers, 2004. **43**(7B): p. 4752-4758.
116. Kim, S., et al., *A study on the flying stability of optical flying head on the plastic disks.* Ieee Transactions on Magnetics, 2005. **41**(2): p. 986-988.
117. Kim, S.H., et al., *Integrated MEMS optical flying head with lens positioning actuator for small form factor optical data storage.* Sensors and Actuators a-Physical, 2004. **114**(2-3): p. 429-437.
118. Lee, J., J. Kim, and N.C. Park, *Air-bearing surface design of an optical flying head considering dynamic characteristics.* Proceedings of the Institution of Mechanical Engineers Part J-Journal of Engineering Tribology, 2008. **222**(J4): p. 581-591.
119. Lee, J.H., et al., *Optical flying head mounted on four-wire type actuator.* Sensors and Actuators a-Physical, 2004. **113**(1): p. 100-105.
120. Mizuno, T., et al., *An optical configuration based on flying head structure for near-field recording.* Japanese Journal of Applied Physics Part 1-Regular Papers Short Notes & Review Papers, 2004. **43**(4A): p. 1403-1409.
121. Ohkubo, T., et al., *Tracking and readout characteristics of a minute aperture mounted optical head slider flying above a chromium patterned medium.* Microsystem Technologies-Micro-and Nanosystems-Information Storage and Processing Systems, 2006. **12**(6): p. 571-578.
122. Ohkubo, T., et al., *Readout characteristics of a non-circular aperture mounted on an optical head slider flying above a medium having sub-100-nm-long patterns.* Microsystem Technologies-Micro-and Nanosystems-Information Storage and Processing Systems, 2007. **13**(8-10): p. 1077-1084.

123. Ukita, H., Y. Katagiri, and S. Fujimori, *SUPERSMALL FLYING OPTICAL HEAD FOR PHASE-CHANGE RECORDING MEDIA*. Applied Optics, 1989. **28**(20): p. 4360-4365.
124. Ukita, H., et al., *READ WRITE PERFORMANCE AND RELIABILITY OF A FLYING OPTICAL HEAD USING A MONOLITHICALLY INTEGRATED LD-PD.* Applied Optics, 1991. **30**(26): p. 3770-3776.
125. Yoon, S.J., et al., *Design of optical flying head for magnetooptical recording.* Ieee Transactions on Magnetics, 2005. **41**(10): p. 2851-2853.
126. Ito, E., et al., *TeOx-based film for heat-mode inorganic photoresist mastering.* Japanese Journal of Applied Physics Part 1-Regular Papers Short Notes & Review Papers, 2005. **44**(5B): p. 3574-3577.
127. Lin, Y., et al., *Ultrafast-laser-induced parallel phase-change nanolithography.* Applied Physics Letters, 2006. **89**(4).
128. Zhang, J., et al., *Lubrication for heat-assisted magnetic recording media.* Ieee Transactions on Magnetics, 2006. **42**(10): p. 2546-2548.
129. Pan, L. and D.B. Bogy, *Heat-assisted magnetic recording.* Nature Photonics, 2009. **3**(4): p. 186-187.